DISSERTATION

A STUDY OF THE INFLUENCE OF PROCESS PARAMETER VARIATIONS ON THE MATERIAL PROPERTIES AND LASER DAMAGE PERFORMANCE OF ION BEAM SPUTTERED Sc_2O_3 and HfO_2 THIN FILMS

Submitted by

Peter F. Langston

Department of Electrical and Computer Engineering

In partial fulfillment of the requirements

For the Degree of Doctor of Philosophy

Colorado State University

Fort Collins, Colorado

Fall 2016

Doctoral Committee:

Advisor: Carmen Menoni

Jorge Rocca
Mario Marconi
Azer Yalin

Copyright by Peter F. Langston 2016

All Rights Reserved

ABSTRACT

A STUDY OF THE INFLUENCE OF PROCESS PARAMETER VARIATIONS ON THE MATERIAL PROPERTIES AND LASER DAMAGE PERFORMANCE OF ION BEAM SPUTTERED Sc_2O_3 and HfO_2 THIN FILMS

This work is a study of the influence of process parameter variations on the material properties and laser damage performance of ion beam sputtered Sc_2O_3 and HfO_2 thin films using a Vecco Spector ion deposition system. These parameters were explored for the purpose of identifying optically sensitive defects in these high index materials after the deposition process. Using a host of optical metrology and materials analysis techniques we report on the relationship between oxygen partial pressure in the deposition chamber during film growth and optical absorption in the grown material at 1 μm. These materials were found to be prone to excess oxygen incorporation. Positive identification of this excess oxygen is made and exactly how this oxygen is bound in the different materials is discussed. The influence of this defect type on the optical and mechanical properties of the material is also given and discussed. Laser damage results for these single layers are presented. The influence of higher and lower deposition energy was also studied to determine the potential for defect creation both at the surface and in the bulk of the material grown. Optimized thin films of HfO_2, Sc_2O_3 and Ta_2O_5 were grown and tested for laser damage with a 1030 nm laser having a pulse width of ~375 ps and a nominal spot size of ~100 μm FWHM. The laser damage threshold ranking of these materials followed fairly well with the band gap of the material when tested in air. When these same materials were tested in vacuum Sc_2O_3 was found to be very susceptible to vacuum mediated laser induced surface defect

creation resulting in a greatly reduced LIDT performance. Ta_2O_5 showed much the same trend in that its in vacuum performance was significantly reduced from its in air performance but there was not as great of a difference between the in air and in vacuum performance as there was for Sc_2O_3. HfO_2 also showed a large reduction in its in vacuum LIDT results compared with its in air LIDT values however, this material showed the smallest decrease of the three high index materials tested. A second contribution of this work is in the investigation of the impact of capping layers on the in air and in vacuum LIDT performance of single layer films. Ultra thin capping layers composed of different metal oxides were applied to 100 nm thick single layers of the same high index materials already tested, HfO_2, Sc_2O_3 and Ta_2O_5. These capped samples were then LIDT tested in air and in vacuum. These ultra thin capping layers were shown to greatly influence the in air and in vacuum damage performance of the uncapped single layers. Damage probability curves were analyzed to retrieve surface and bulk defect densities as a function of local fluence. Methods for maximizing the LIDT performance of metal oxides based on our studied materials for use in air and in vacuum are discussed.

TABLE OF CONTENTS

ABSTRACT ii
LIST OF TABLES v
LIST OF FIGURES vi
CHAPTER I. INTRODUCTION 1
CHAPTER II. PREVIOUS WORK ON HfO_2 AND Sc_2O_3 19
CHAPTER III. INTERFERENCE COATINGS 42
CHAPTER IV. ION BEAM SPUTTERING OF METAL OXIDES 57
CHAPTER V. THIN FILM CHARACTERIZATION 68
CHAPTER VI. DATA AND RESULTS 100
CHAPTER VII. CONCLUSIONS AND FUTURE WORK 146
BIBLIOGRAPHY 150
APPENDIX 158

LIST OF TABLES

Table 1: Band gap energies of metal oxides 2
Table 2: Absorption at 1 μm 114
Table 3: Absorption loss at 1.064 μm for the basecoats and capped samples. The absorption loss of a 100 nm thick SiO2, 1-2 ppm, is barely distinguished from that of the substrate. 162

LIST OF FIGURES

Figure 1: Taken from Jupe et al.[11]. Demonstration of multi photon absorption in laser damage processes 9
Figure 2: Taken from Stuart et al. [15] 11
Figure 3: Hypothetical damage onset curves using two different laser spot sizes. Red points represent testing with a larger hypothetical spot size than the black squares. 12
Figure 4: Generic crystal lattice 30
Figure 5: Silicon-oxygen bond arrangement [65] 31
Figure 6: Quartz crystal lattice structure [66] 32
Figure 7: Amorphous SiO_2 grown on single crystal silicon [67] 33
Figure 8: Light at an interface [100] 44
Figure 9: Single layer in air 45
Figure 10: Phase shift at an interface [101] 46
Figure 11: Multiple surface reflections 47
Figure 12: Specular vs diffuse reflections [103] 49
Figure 13: Idealized vs practical band gap [104] 50
Figure 14: Transitions in a defect laden high band gap material [105] 51
Figure 15: Induced defect states [105] 53
Figure 16: Conduction band electron density due to multiphoton ionization only and with the addition of avalanche ionization [15]. 54
Figure 17: Vecco Spector dual ion beam sputtering system diagram 59
Figure 18: Sputtering ion source in the Vecco Spector [108] 61
Figure 19: Collision cascade [109] 62
Figure 20: Thompson's energy distribution of sputtered material 62
Figure 21 (a) and (b): 600 eV and 1.2 KeV Ar+ impacting and penetrating into an oxidized (10 angstrom) scandium target at 45 degrees from the surface normal. 63
Figure 22: Energy lost to phonon creation in the target from the incoming ions (red curve) and recoiling target atoms (blue curve). 600 eV Ar+ incident on the target at 45 degrees from the surface normal. 64
Figure 23: Oxygen and scandium dislocated in the target for 600 eV Ar+ impacting at 45 degrees from the surface 65
Figure 24: Sputtered atoms of oxygen and scandium for 600 eV Ar+ impacting at 45 degrees from the surface normal. 65
Figure 25: Oxide coverage of a metal target plotted against oxygen partial pressure [110]. 67
Figure 26: Typical spectrophotometer trace. 69
Figure 27: Example Tauc's plot of Sc_2O_3 single layers one as grown and one annealed. 69
Figure 28: Diagram of Woollam ellipsometer operation. [111] 70
Figure 29: Twyman Green interferometer 72

Figure 30: Typical PCI surface absorption signal.. 74
Figure 31: PCI schematic.. 75
Figure 32: Picture of PCI at Colorado State University 75
Figure 33: Total integrated scattering sphere, sample and diode [115]. 77
Figure 34: XPS diagram.. 78
Figure 35: HfO_2 XPS 4f peak 79
Figure 36: HfO_2 and hafnium XPS 4f peak 80
Figure 37: FTIR spectra [116] 82
Figure 38: Example FTIR spectra of an Sc_2O_3 films grown on Fused Silica 82
Figure 39: AFM explanatory diagram [117].. 83
Figure 40: Representative AFM scan of a 100 nm thick HfO_2 film 84
Figure 41: SEM image of a damage site on a Sc_2O_3 single layer film 85
Figure 42: SEM image of a damage site on a HfO_2 single layer film 85
Figure 43: XRD Bragg diffraction [118] 86
Figure 44: XRD system 87
Figure 45: Example XRD scan of an Sc_2O_3 film.. 87
Figure 46: Mechanisms to strain broaden an XRD peak [119] 88
Figure 47: Zeeman split of one energy level [121]... 89
Figure 48: Diagram of an EPR cavity, magnet and support equipment [122]............................... 91
Figure 49: Example EPR spectra of two Sc_2O_3 films grown using different oxygen partial pressures... 92
Figure 50: Diagram of in air LIDT test setup 94
Figure 51: Picture of in air LIDT test setup.. 95
Figure 52: UHV damage test apparatus.. 96
Figure 53: Schematic of UHV damage apparatus.. 96
Figure 54: XEI plasma cleaner used to remove hydrocarbon contamination from test optic surfaces before introduction into the testing vacuum chamber [123]. 97
Figure 55: Partial pressure measurement made on the UHV chamber with a sample inside after 8 hours of pumping. 98
Figure 56: (a) X-ray diffraction spectra of amorphous Sc_2O_3 for films deposited as a function of oxygen partial pressure. The film obtained at 2 μTorr shows diffraction features of crystalline scandium, and was opaque. All other films instead showed diffraction peaks that are identified with the (222) and (440) peaks of cubic Sc_20_3. (b) The FWHM of the (222) peak increases and the peak position decreases to smaller angles with oxygen partial pressure, indicating an increase in the lattice parameter due to increased strain. 105
Figure 57: Stress in Sc_2O_3 films with (a) variation in the beam voltage and (b) variation in the oxygen partial pressure. 106
Figure 58: Electron paramagnetic resonance spectra for Sc_2O_3 films deposited at different oxygen partial pressures. A line shape analysis of the spectra is used to identify the defects and

determine their density. An increase in the signal intensity correlates with a larger density of defects. 107
Figure 59: Absorptivity of amorphous Sc_2O_3 films deposited using (a) different oxygen partial pressures and (b) different beam voltages. The triangle symbols identify a set of samples grown without use of the assist source. Both sets of data show an increase in absorptivity with oxygen partial pressure. The increase in absorptivity correlates with the increase in the density of oxygen defects. 108
Figure 60: Normalized absorptivity for Sc_2O_3 films at λ = 1064 nm and λ = 514 nm. The data was normalized to the value of the absorptivity at λ = 1064 nm for the film deposited at a beam voltage of 1250 V........ 110
Figure 61: Standing wave electric field for capped and uncapped HfO_2........ 113
Figure 62: Partial pressure measurement of UHV chamber with sample installed. 115
Figure 63: Diagram of UHV damage test apparatus........ 116
Figure 64: Picture of UHV beam director........ 117
Figure 65: The zero % probability LIDT results of single layers tested in clean air (FS damaged at 47 ± 2.35 J/cm^2) 119
Figure 66: The zero % probability LIDT results of Sc_2O_3 basecoat series tested in clean air (FS damaged at 47 ± 2.35 J/cm^2) 120
Figure 67: The zero % probability LIDT results of HfO_2 basecoat series tested in clean air (FS damaged at 47 ± 2.35 J/cm^2) 120
Figure 68: The zero % probability damage onset curves for Sc_2O_3 basecoat series tested in clean air 121
Figure 69: The zero % probability damage onset curves for HfO_2 basecoat series tested in clean air 122
Figure 70: The zero % probability LIDT results of single layers tesed in air and vacuum (FS damaged at 47 ± 2.35 J/cm^2 in air and at 52.6 ± 2.6 J/cm^2 in vacuum) 123
Figure 71: The zero % probability LIDT results for Sc_2O_3 basecoat series tested in UHV (FS damaged at 52.6 ± 2.6 J/cm^2) 125
Figure 72: The zero % probability LIDT results for HfO_2 basecoat series tested in UHV (FS damaged at 52.6 ± 2.6 J/cm^2) 126
Figure 73: The zero % probability LIDT results for Sc_2O_3 basecoat series tested in UHV 127
Figure 74: The zero % probability LIDT results for HfO_2 basecoat series tested in UHV 128
Figure 75: Typical 100 on 1 damage site on 10 nm SiO_2 capped Sc_2O_3 128
Figure 76: The zero % probability LIDT results for Sc_2O_3 basecoat series tested in air and vacuum (FS damaged at 47 ± 2.35 J/cm^2 in air and at 52.6 ± 2.6 J/cm^2 in vacuum)........ 129
Figure 77: The zero % probability LIDT results for HfO_2 basecoat series tested in air and vacuum (FS damaged at 47 ± 2.35 J/cm^2 in air and at 52.6 ± 2.6 J/cm^2 in vacuum)........ 130
Figure 78: Example of damage probability curve and corresponding least squares fit for HfO_2 single layer. 132

Figure 79: Corresponding defect density found using least squares fit of the damage probability curve for bulk absorption in HfO_2. 133
Figure 80: Surface defect densities for single layers tested in clean air. 134
Figure 81: Surface defect densities for Sc_2O_3 basecoat with different capping layers tested in air 136
Figure 82: Volume defect densities for HfO_2 capped Sc_2O_3 basecoat series tested in air 136
Figure 83: Surface defect densities for HfO_2 basecoat series tested in air 137
Figure 84: Surface defect densities for fused silica tested in air and vacuum. 139
Figure 85: Surface defect densities for single layers tested in air and vacuum. 140
Figure 86: Surface defect densities for Sc_2O_3 basecoat series tested in air and vacuum 141
Figure 87: Surface defect densities for HfO_2 basecoat series tested in air and vacuum. 141
Figure 88: Diagram of UHV damage test apparatus. 163
Figure 89: Zero percent probability LIDT of single layers tested in-air and at UHV. For reference the fused silica substrate damaged at (47±2) J/cm2 in-air and at 53±3 J/cm2 at UHV. The error bars are associated mainly with the uncertainty in pulse duration, ±4%. 166
Figure 90: Zero percent probability LIDT of Sc_2O_3 capped with SiO_2, HfO_2 and Ta_2O_5 tested in-air and at UHV. 167
Figure 91: The 0 % probability LIDT for HfO_2 basecoat series tested in air and in UHV 168
Figure 92: Damage probability versus fluence for Sc_20_3, HfO_2 and capped layers Sc_2O_3 capped with HfO_2 and HfO_2 capped with Sc_2O_3 for tests carried out in-air (left) and in UHV (right). Both of these traces show scattered data points or shoulder at low (<30%) damage probability. 169
Figure 93: Figure 93 (b) Defect densities of the Sc_2O_3 basecoat series extracted from the damage probability curves in air and in UHV from the fit with Eqs. (1) and (2). (a) Defect density in the HfO_2 basecoat series. 171

CHAPTER I. INTRODUCTION

Optical systems that contain multiple elements, or by their design require light to interact with fewer elements many times, would suffer unacceptable losses if not for the advent and use of interference films. These films make use of the wave nature of light and what is known as the Bragg condition, where the optical path length of at least two different transparent materials, each having a unique optical index, is tailored to make use of interference effects to either enhance or diminish the light intensity on one side of the coating stack. Many variables play into the design of these stacks including the wavelength of the light being used, the required bandwidth, environmental conditions the film will see, how much stress can be allowed in the film, and the optical intensity these films will be exposed to.

The most common materials for use in optical interference coatings are Sc_2O_3, HfO_2 and Ta_2O_5 as the high index material and SiO_2 or Al_2O_3 as the corresponding low index material. For use in high energy applications this list is often reduced to Sc_2O_3 or HfO_2 paired with SiO_2. In general, for high purity target materials grown using optimal deposition conditions, the laser induced damage threshold (LIDT) value of these materials scales with the effective band gap of the oxide in question [1].

The published values for the band gaps of these materials vary, sometimes by significant amounts. Reported values of the bandgaps for the oxides we are discussing are listed in table 1. These values lead to a natural ranking of the LIDT performance of the respective films composed of these oxides. Unfortunately, the story is not as simple as this in practice. A physically realizable film is never truly defect free. Moreover, in an amorphous film one would naturally expect a gamut of point defects as vacancies and interstitials. The work presented in

this thesis is a culmination of the research we have done at Colorado State University attempting to understand the origin of and influence that point defects, both native and laser induced, have on the chemical and physical properties of these materials, and ultimately on the laser induced damage threshold LIDT performance of thin films designed using them.

Table 1: Band gap energies of metal oxides

Metal Oxide	**Band Gap, E_g(eV)**
Ta_2O_5	3.8[2]
HfO_2	5.1[2]
Sc_2O_3	5.7[3], 6.3[4]
SiO_2	8.3[2]

Currently both anti reflection (AR) and high reflecting (HR) thin film structures are the limiting optical elements of all high energy laser systems. Any improvements that can be made in the laser damage performance of these films are highly desirable and in many cases required for the advancement of compact high energy laser source development.

While the development of high damage threshold optical thin films continues today, this problem is not a new one. Soon after the advent of the laser in 1960, development on optical coatings exhibiting high damage thresholds became a priority. So much work was directed to this issue, in fact, that a symposium dedicated to understanding laser damage phenomenon, the Boulder Damage Symposium, was chartered in 1968 [5]. Over forty years of work in the area of laser damage of optical materials has greatly enhanced our understanding of these light/matter interactions. Unfortunately, while there have been a multitude of models developed and used to predict the expected performance of a given material in a specific application, these models

cannot be applied in a general case with much accuracy. In short, it is not difficult to find contradictions between any two existing models and even more so between measured results and modeled behavior. Some of this inconsistency is due to the difficulty in reproducing the experimental conditions of any given test. This is true even for tests performed at the same lab over long periods of time. After decades of work we are still left wondering if the best models of the damage process incorporate enough of the defining variables to be an accurate description of the damage phenomena. For now, the most useful information a researcher can have is theoretical and empirical data specific to the coating process and application he or she is using.

Goal of This Study

The work we did at Colorado State University was aimed at gaining fundamental understanding of how different process parameters, specific to our process of ion beam sputtering, influence the mechanical and optical properties of the thin film oxides HfO_2 and Sc_2O_3, together with SiO_2 and Ta_2O_5. This work focuses on laser damage studies in an effort to optimize these materials' performance in different environments, in controlled air and vacuum. The results of our studies have highlighted the extreme care that must be taken to ensure the correct amount of oxygen is incorporated into these oxides to ensure a fully stochiometric but not over oxygenated material [6]. Additionally, the relative influence of the deposition energy was studied to assess the resulting thin films performance from a laser damage perspective.

Results of the work presented herein show that in a standard atmospheric environment the relative ranking of the LIDT for our high index materials follows the expected trend for the relative band gaps of these materials. When these same materials are tested in a reducing environment the LIDT ranking changes, displaying a material dependent sensitivity to vacuum

conditions. The influence of a modified first surface is then investigated by introducing very thin capping structures and retesting these samples in both air and vacuum. The results of these tests show a strong damage dependence on the first surface material in both environments, air and vacuum, as well as giving a relative sensitivity of these different materials to a reducing environment. Specifically, Sc_2O_3 and Ta_2O_5 are more sensitive to vacuum than HfO_2, while SiO_2 shows almost no difference in its performance when tested in air or vacuum.

While many different deposition techniques are used to grow optical films, ion beam sputtered (IBS) coatings possess several characteristics that are highly desirable for use in laser damage resistant environmentally stable films. Ion beam sputtering is a relatively high energy process that is capable of producing near crystalline packing densities in an amorphous structure [7]. Compared with lower energy coating processes such as E-beam deposition, IBS coating's increased density results in a less porous, higher optical density material. This fact results in a less sensitive material to environmental conditions as well as requiring fewer coating pairs to achieve a desired reflectivity. Unfortunately, as mentioned before, higher energy deposition techniques also suffer from difficulties that are less severe or are not seen at all in lower energy processes. One of the most useful aspects of the IBS coating technique is the many degrees of freedom this process offers. This versatility lends itself nicely to researching the influence of coating processes on the damage performance of the films produced.

The materials we have grown for our studies were deposited using a Vecco Spector dual ion beam sputtering machine [8]. This chamber is equipped with a cryo-pump rather than a turbo molecular pump to evacuate the deposition chamber. A cryo-pump's unique ability to effectively reduce the vapor pressure of any water near the cold finger to essentially zero allows for a clean and dry deposition environment. Generally cryo-pumps are capable of reducing the

water content in a vacuum below what a standard turbo molecular pump is capable of for an equivalent pumping time. The Spector coating tool allows for the independent adjustment of nearly every aspect of the coating process. Some of the adjustable parameters include the fact that the sputtering rate can be adjusted while maintaining the same accelerating voltage by altering the amount of argon present in the ion gun. The system can be used with or without the additional ion assist which is traditionally used to help randomize and level the layers as they are laid down. The coating layers can be grown identically over a very large number of samples by making use of a planetary sample holder that spins on two separate axes to help fully randomize the location where each substrate is during film deposition. This fact is invaluable when large numbers of tests need to be performed on a single sample set. Coupled with the traditional adjustment "knobs" common to other deposition processes, including deposition rate, chamber pressure, deposition energy, target purity, substrate used, substrate temperature and beam current the parameter space available is extremely large. This fact alone makes IBS coating techniques favorable to researching process parameter influence on the LIDT performance of thin films. The fact that IBS films are environmentally insensitive, high density, and already display high laser damage thresholds suggests this technique is the most promising to realize maximum index, long term stability and the highest damage threshold optical films possible.

Narrowing Parameter Space

As already mentioned, the dual ion beam sputtering process is attractive from a research standpoint owing to the size and scope of the process parameter space that can be explored for optimizing specific material characteristics. This versatility is attractive but also presents research staff with more options than can reasonably be explored due to expense and machine

availability constraints. For these reasons it was necessary to limit our areas of study to those process parameter studies we believed would most directly contribute to our understanding of how to produce low optically sensitive defect density materials that can act as the high index layers in thin film structures.

Given that we only had metallic targets available from which to grow our high index metal oxides, the influence of the relative concentration of oxygen in the deposition chamber during film growth was an obvious starting point. The parameter space available for these oxygen partial pressure experiments extended from the point where we confirmed the growth of metallic films to well beyond the point where we always found fully stoichiometric bonding environments with oxygen for the base metal in our films.

The second of the major parameter variations that this work reports on is the influence of primary ion energy on the material and optical properties of the films produced. The methodology behind the decision to study this parameter space was the insistence of a large and well recognized contingent within the laser damage community that was confident in their belief that lower energy deposition processes, like e-beam deposition, were always going to be a superior growth method for producing high damage threshold materials. This belief was based on the measured performance of e-beam deposited films relative to other higher energy processes. It has been suggested that porous films are better able to handle, without fracturing, the rapid temperature variations seen during laser exposure if appreciable absorption is present in the films. One of the principle benefits of a higher energy deposition process like IBS is the lack of a porous structure in the films produced. This fact directly results in a more environmentally insensitive material. In paying what we believe to be reasonable deference to the opinions of others who had been working in this field longer than our research group we chose to probe this

parameter space to quantify the influence of the primary ion energy on the inclusion of optically sensitive defects in our films.

When measuring the laser damage performance of these materials we are again presented with a large parameter space from which to choose in terms of what laser source to use, what spot size to choose, what pulse width is most useful, etc. Many of these testing parameters were chosen for us simply by the fact that we had a system with an already defined set of operating parameters available to us. If we were to insist on using something different it was going to cost a great deal in terms of convenience and expense. Still, some testing parameter considerations might require these prices to be paid if the integrity of the data would be compromised otherwise. Longitudinal mode beating is one of those parameters that cannot be tolerated when measuring laser damage performance. In our case a mode locked Yb:KYW oscillator insured a constant phase relation between all the potential modes in the cavity. The gratings in the pulse stretcher impose a linear chirp which preserves the fixed phase relationship between the shorter and longer wavelengths under the gain envelope. The choice of the testing laser spot size was a practical limitation imposed by the fact that our samples were only one inch in diameter. Had we used a larger spot size, which would have better characterized the samples performance as a whole, the number of test sites would have been reduced giving us less statistical information on the performance of the material to a given probing fluence. This is obviously a trade off that one can argue from either perspective. The choice of the testing pulse width is seemingly less critical given the well known $t^{1/2}$ pulse width dependence, which can be used to scale the damage performance measured at one pulse width to the expected performance at a second pulsewidth. This scaling has been shown to work well if other influences don’t alter the results.

Unfortunately, stimulated Brillouin scattering (SBS) is a consideration that must be accounted for when operating at very small spot sizes or at longer pulsewidths. The use of ~375 ps pulsewidths and ~100 μm FWHM spot sizes allowed us to ignore the influence of SBS in our analysis. Of course, the choice of the probing wavelength, ~1 μm, was imposed on us generally by the prevalence of lasers operating at this wavelength in the industry but also specifically by the principle sponsor of this research. These considerations were the major influences on the direction of the research at the time the decisions were made. Other considerations were necessarily addressed during the course of the work but these were generally of less significance.

Previous Research on Laser Damage in the Infrared

As noted before, there have been decades of work probing the origin and evolution of laser induced damage in optical materials. This work has given us a much improved understanding of the influence of many of the significant contributors to the LIDT performance of a given film or coating stack. It is informative to separate the variables that influence the laser damage behavior of optical coatings into those effects that are light source dependent (frequency, pulsewidth and spot size) and those that are not strictly light source dependent. As the laser wavelength is decreased the fluence needed to initiate damage is reduced [10]. This effect is material dependent. For an ideal, and hypothetical, material that has a band gap of 3 eV, LIDT testing using photons of 1 eV would require sufficient intensity to drive three photon processes to bridge the band gap, approximately 10^{10}-10^{11} W/cm^2, while a single 3 eV photon could provide the energy needed. This behavior can be seen in the LIDT performance of a material tested at different wavelengths as shown in figure 1 below.

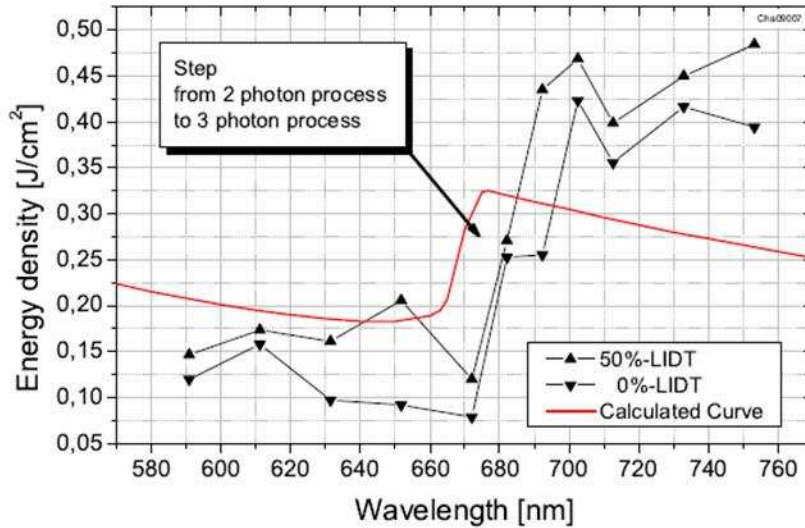

Fig. 7. LIDT of TiO_2 -single layer in dependence on the wavelength. Below approx. 670nm two-photon absorption is observed. At 680nm the predicted step of the LIDT towards three-photon absorption is evident.

Figure 1: Taken from Jupe et al.[11]. Demonstration of multi photon absorption in laser damage processes

In the case of a less ideal material, one that included optically sensitive defects but having the same band gap (3 eV), cascaded single eV processes may be capable of imparting enough energy to excite electrons across this potential barrier [10, 11].

The pulse duration of the laser used for testing plays an equally influential role in the damage initiation process. Generally laser damage testing is broken into two distinct groupings based on the laser pulsewidth. This break in behavior is seen at short time scales below ~10 ps pulsewidths. Laser damage from continuous wave (CW) down to around 10-20 ps pulses is associated with thermal processes, meaning there is time for the energy deposited by the laser to diffuse into the material surrounding the laser focal volume [12]. This process is governed by the photon-phonon energy transfer time. For pulses shorter than ~10-20 ps there is no time for the lattice to absorb energy, only for the electronic transitions driven by the photons themselves and subsequent free electron heating. These electronic transitions have time constants on the

order of a few femtoseconds where the time scale needed for the dissipative Joule heating of the electrons to translate to the crystals momentum (phonon creation) occurs on time scales of a few to hundreds of picoseconds [13, 14]. In the case of short pulse damage on dielectric materials the description of the heat transfer is complicated by the intermediate state of the material during the absorption process.

For a crystalline metal, heat absorption and conduction is accomplished by the electrons only. Heat transfer to the lattice happens primarily at lattice discontinuities by inelastic scattering of the electrons. If the crystalline material is instead a dielectric, heat conduction is exclusively a phonon process. Short pulse damage is initiated by high order absorption populating the conduction band of the material. This results in a hybrid condition where both electrons and phonons transport energy through the lattice. The speed of these energy transporting quanta and the mean free path in the material determines the rate at which the heat can transfer from the high temperature electron cloud to the lattice of the material. Amorphous materials typically have shorter mean free paths compared with crystalline structures of the same composition. Even so lattice heating of amorphous materials is still much too slow to efficiently react to femtosecond heating. Stuart et al. showed a $t^{1/2}$ dependence of the LIDT with the laser pulsewidth for pulses longer than ~10ps, shown in figure 2. This is generally considered to be the start of the long pulse or thermal damage response. In the case of optical coatings this short pulse response is quite unwanted and practically impossible to escape, however, the field of laser micromachining relies on this type of short pulse interaction to minimize the collateral damage outside the laser spot [3, 15].

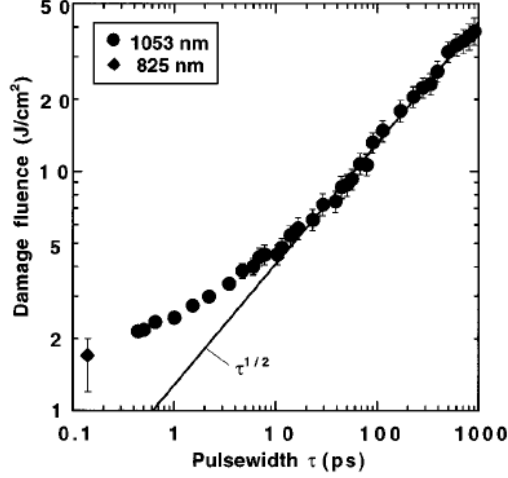

FIG. 3. Pulse width dependence of threshold damage fluence for fused silica.

Figure 2: Taken from Stuart et al. [15]

Stuart modeled the heating and collisional ionization of conduction band electrons using the Fokker-Planck expression shown in equation 1.

$$\frac{\partial N(\varepsilon,t)}{\partial t} + \frac{\partial}{\partial \varepsilon}\left[R_J(\varepsilon,t)N(\varepsilon,t) - \gamma(\varepsilon)E_p N(\varepsilon,t) - D(\varepsilon,t)\frac{\partial N(\varepsilon,t)}{\partial \varepsilon}\right] = S(\varepsilon,t) \qquad (1)$$

where $S(\varepsilon,t) = R_p(t) - R_I(\varepsilon)N(\varepsilon,t) + 4R_I(2\varepsilon + U_I)N(2\varepsilon + U_I,t)$

$N(\varepsilon,t)$ is the electron distribution function. $R_J(\varepsilon,t)N(\varepsilon,t)$ describes the Joule heating of the electrons and $D(\varepsilon,t)\frac{\partial N(\varepsilon,t)}{\partial \varepsilon}$ describes the diffusion of the electron distribution's energy. The rate of energy transfer from the electrons to the lattice is described by $\gamma(\varepsilon)E_p N(\varepsilon,t)$ where $\gamma(\varepsilon)$ is the rate constant. The $S(\varepsilon,t)$ term represent all sources and sinks for electrons in the system, where $R_p(t)$ and $R_I(\varepsilon)$ are multiphoton ionization and impact ionization terms respectively. In the case of femtosecond LIDT testing the multiphoton ionization term strongly dominates the sourcing function while for lower intensity testing multiphoton ionization only seeds the

avalanche ionization process which then quickly dominates the electron source term. Generally these expressions are used to model idealized materials, meaning a defect free band gap. There is, however, no reason this expression, with slight modification, could not be used to model the behavior of a material with mid-gap defect states.

The spot size used for LIDT testing can also strongly influence the shape and slope of a damage curve. For the sake of understanding, a damage probability curve is a statistical measure of the likelihood of a surface or bulk material to display a permanent laser induced modification as a function of laser fluence. Figure 3 shows an example of two hypothetical damage onset curves. Generally, each data point plotted represents the ratio of damage events to the number of test shots at a constant fluence, $\frac{Number\ of\ shots\ that\ damaged}{Number\ of test\ shots\ at\ a\ constant\ fluence}$. If we assume the two plots in this figure were damage tests performed on the same material we might expect the red curve to have been measured using a larger spot size.

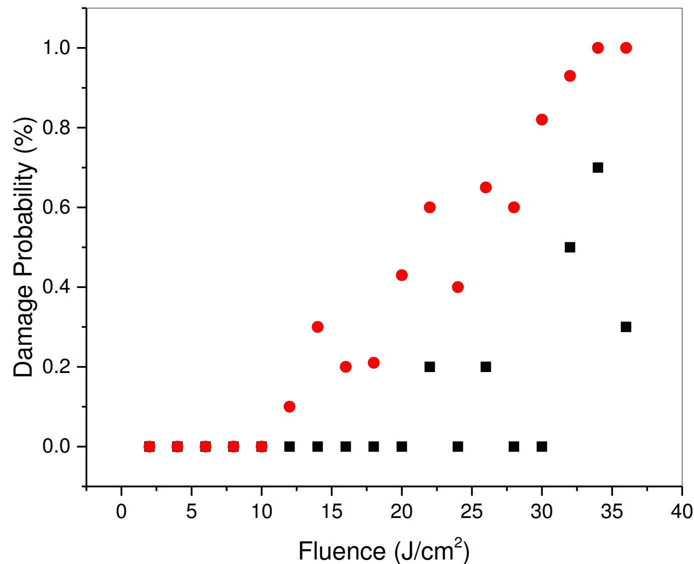

Figure 3: Hypothetical damage onset curves using two different laser spot sizes. Red points represent testing with a larger hypothetical spot size than the black squares.

These differences in a measured onset curve can result in very different values, or at least different uncertainty in this value, for the measured onset fluence in any given test [16-18]. Ultimately, these differences are not real representations of the laser damage resistance of the film as a whole. With larger spot sizes it is more probable that if there were extrinsic defects in the film, such as dust or other macroscopic inclusion, those defects would be exposed to sufficient energy to initiate damage. Where the same sample is tested with a small spot size (~10 micron) it is possible to interrogate areas having no extrinsic defects. In this case it is possible to have individual test sites damaging at fluences that are different by orders of magnitude on the same optic. Damage onset curves plotted with data collected using small spot sizes typically show huge errors in the measured onset values. Intrinsic material, by contrast, does not necessarily imply defect free material but rather a homogeneous material that may possess nanoscale defects as long as they are uniformly distributed throughout the layer or bulk. Sometimes it is useful to test with very small spot sizes if there is an interest in comparing process parameter influence on bulk, or intrinsic, materials but these data are of limited use in real world applications [16]. In general, it is a good idea to keep the testing spot size as large as reasonably possible. The peak fluences achievable are strongly dependent on spot size for a fixed laser energy and it is important to keep individual test sites on an optic far enough away from each other that one site does not contaminate another site during the damage testing.

From a light source independent perspective, there are many contributors to the damage threshold performance of an arbitrary thin film, including the substrate used, the deposition process, target purity, deposition energy, substrate roughness, and the atmosphere the film is tested in.

The material on which the film is deposited plays an important role in providing a uniform and stable platform on which to grow the amorphous dielectric film. Work studying the influence of the thermal conductivity of the substrate on the LIDT performance of a thin film has shown the ability of the substrate to act as a heat sink for the structures grown on it. A high conductivity substrate, such as sapphire or copper, can improve the laser damage performance of a thin film in the case of long pulse damage testing [19]. Additionally, the substrate can influence the uniformity and interface roughness in the coating stack if the substrate has grinding or polishing marks before the film is deposited. These inhomogeneities and interface defects can lead to a decreased damage resistance in the film due to subsurface impurities trapped in polishing marks or local field enhancements at roughened interfaces [20-22].

The deposition process used has major implications for the physical and chemical properties of the thin films that are produced. Consequently, the deposition process may be one of the best indicators of the potential LIDT performance of the film. There are a large number of different processes that have been developed for thin film deposition. The two major categories that encompass thin film growth processes are Chemical Vapor Deposition (CVD) and Physical Vapor Deposition (PVD). While CVD processes are very useful for applications requiring conformal and low stress deposition, they can leave organic contaminants in the film that in many cases compromise the film for high fluence applications.

Most high damage threshold optics rely on PVD deposition to produce the films they use. A great deal of work has been devoted to advancing many of the PVD processes hoping to securely claim theirs as the best method for producing high damage threshold optical coatings. Unfortunately, no single process stands out for use in all high energy laser applications. Until recently, electron beam (EB) evaporation has been the preferred deposition process for high

fluence applications. One of the major detractors to the use of EB evaporated films is the porous nature of these films. There has been a great deal of discussion surrounding the utility of a porous film for use in high energy laser (HEL) optics [3]. The general point of the argument has been that if a film is not very dense then the film is more capable of surviving large temperature gradients and by extension large local expansion and contraction cycles without cracking or spalling. While this is very likely true for low density films, the fact that the film is not dense and has a porous structure presents any material composed of these films with other undesirable traits including low optical density (index) and surface voids that can be filled by contaminants, the most common of which are carbon and water.

In PVD processes generally there is a localized target from which material is evaporated or ablated before it is deposited on the substrate. This target can take any one of a number of different configurations in the coating chamber but the purity of the thin film that is produced is directly related to the purity of the target used. For our purposes, targets are generally either a pure metallic target or an oxide of that metal. If a metallic target is used the atmosphere in the coating chamber is tailored to ensure the metal is fully oxidized on or before reaching the substrate. This process is referred to as reactively grown films [23, 24].

As the name of this type of deposition suggests, there is a physical interaction used to create the vapor that is deposited as a thin film. This process of creating the vapor phase oxide requires some amount of energy to drive the solid target into a vapor phase. In PVD processes this energy level is one of the key variables that is used to tailor the optical and mechanical properties of the films produced. In EB evaporation the energy the evaporated material has when it reaches the substrate is generally quite low in comparison with other common PVD processes. Previous work has acknowledged that higher energy deposition processes are more likely to

produce nonstoichiometric oxides given the higher probability of preferentially sputtering the lighter oxygen when these oxides are hit with high energy particles or clusters [25-30]. Many advantages are available to higher energy coating processes, however, that are not possible for lower energy deposition methods. The ability to tailor the energy used to deposit a single layer or coating stack may be invaluable in the effort to produce high optical index, high damage threshold environmentally stable films. The influence of deposition energy on the mechanical and optical performance of high index films will be discussed in some detail later.

As mentioned earlier, the interface roughness of a film is important from a damage threshold perspective, but it is also important from an optical loss perspective. For most modern thin films, optical absorption is measured in parts per million (ppm). Losses on these orders are not generally major impediments to the optical throughput of a system. While absorption is generally the metric of greatest concern when discussing the resistance of a film to laser induced damage, the quality of the optic as a whole must include all loss terms such as transmission, reflection losses and scattering losses in addition to absorption. Surface roughness on the order of a few nanometers does not directly correlate with the LIDT performance of a film but it can significantly influence the scattering losses of the film and in more extreme cases may contribute to a lower conductivity and mechanical stability of the film structure [31, 32]. The deposition process, and even more so the deposition parameters used, can massively influence the interface roughness of a given film.

The environment in which a film is tested also influences the damage performance of a film. If the environment is dusty, the debris resting on the surface of a film can cause the film to fail at a much reduced fluence. A more subtle influence on the performance of the film is in the composition and partial pressure of the atmosphere the film is tested in. Earlier work has shown

reduced damage resistance of a film tested in an atmosphere with high moisture content [18]. Hydrocarbon influences have also been studied [33]. Other combinations of gasses have been investigated in an attempt to better isolate the primary contributors to surface damage onset [34]. At the other end of the spectrum, there is significant interest in the performance of metal oxides when used in a vacuum environment. Metal optics show very little difference in their LIDT values when measured in either air or in vacuum. Instead, interference films composed of metal oxides display a reduction in their damage onset values when measured in vacuum as compared to their in air values [34]. Specific examples of optical thin films used in vacuum include compressor optics used in chirp pulse amplifiers (CPAs), space based optics, gravitational wave interferometer mirrors (LIGO), as well as others [35]. Earlier work on the influence of vacuum on the LIDT performance of these films has given some insight into potential causes of damage, but no study has been able to conclusively determine what is the mechanism that leads to such dramatic reductions in the damage onset values. The more likely reasons for this reduction in LIDT performance in vacuum are the reduced thermal conductivity of a surface devoid of water and air to help carry energy away, carbon contamination and laser induced surface defect creation. Reducing the amount of water on the surface could have two effects. The first being a reduced thermal conductivity [36] and the second being a fracturing effect when the water is vaporized. Either or both of these are very likely to be contributors to the damage performance of some materials. Regardless of the partial pressure of water in the vacuum chamber, a reduced air pressure will also reduce the heat removing capacity of the environment above the damage site. While this is not expected to be a major contributor it is still present. The last possible source mentioned was increased surface absorption due to the creation of defects, possibly in the form of nonstoichiometric oxides [34]. Other work has shown the single shot LIDT behavior of these

films is nearly the same in vacuum as when measured in air [34]. Only after multiple laser pulses are applied to the test site does the LIDT behavior begin to significantly change from the in air performance. This of course implies some kind of laser induced surface modification. We discuss this phenomenon in some detail later in the thesis.

While many aspects of measured laser damage performances do not always show consistent trends when studied by different groups, it is generally accepted that damage initiation is most often seen in the high index material of a coating stack [37]. Naturally, most of the effort to increase the LIDT performance of HR and AR films then requires improvements in the high index material.

CHAPTER II. PREVIOUS WORK ON HfO_2 AND Sc_2O_3

HfO_2 and Sc_2O_3 grown by ion beam sputtering are the focus of our work. These materials are used in combination with SiO_2 to engineer interference coatings for high energy infrared laser applications. HfO_2 has been well studied by both the high energy laser community as well as by the semiconductor industry, where it is useful as a high dielectric constant alternative to SiO_2 [2, 3, 7, 16, 28-30, 33, 36-97]. In the following chapter specific examples of previous research are discussed as they relate to the mechanical or optical properties of the materials we are investigating.

Previous Work Specific to Hafnia

Previous work has shown HfO_2 is more sensitive to deposition conditions than SiO_2 in terms of its structural and optical properties [29]. Wang et al. suggests intermediate deposition energies might be preferred to either lower or higher energies, if the thin film is grown using a sputtering process, as HfO_2 changes from weakly monoclinic to amorphous to strongly monoclinic with increasing momentum of the sputtering ions.

M. Alvisi et al. studied the influence of ion momentum on the LIDT performance of HfO_2 tested at λ=248nm using 30ns laser pulsewidths. They found a ~2.1 J/cm^2 damage threshold for their best materials. They also found an abrupt phase change from random monoclinic to an oriented monoclinic when increasing the momentum of the deposition process [38]. The results of these efforts suggest lower energy sputtering may reduce the number of optically sensitive defects in the deposited material. Additionally, this work found that HfO_2 sputtered from an HfO_2 target in argon only, with no oxygen, was found to be amorphous. When

oxygen is present during the deposition the film is found to be polycrystalline [39]. In addition to being prone to other defect types polycrystalline HfO_2 can trap moisture on dangling bonds located at grain boundaries [40].

Thielsch, R., et al. discussed that ion beam sputtered HfO_2 films showed oxygen deficiency when bombarded with ions. There is evidence correlating oxygen deficiency with higher biasing voltages in the case of IBS SiO_2 films. This condition for the SiO_2 films was persistent after deposition and was likely caused by ion bombardment [28].

In an effort to corroborate this apparent link between high energy sputtering and oxygen deficient films, Toldedano-Luque, M. et al. made use of a relatively high chamber pressures to nearly thermalize evaporated material through collisions before deposition [39]. The results of this work are compelling but films produced in this way lacked the physical and optical qualities desired in IBS deposited materials, namely high index and high density.

Additional work on the influence of deposition energy on the properties of the films produced was done by Papandrew, A.B., et al. They also insist that careful selection of the deposition energy is required to ensure fully stoichiometric material while not imparting too much energy to the newly formed surface. This work also asserts that deep nodular defects play a larger role in laser damage than shallow nodular defects [30]. Depending on the type of films being considered this may or may not be an obvious conclusion. In any case, this assertion has particular significance to our damage results which will be discussed later.

Roberson et al. published a discussion on common optically sensitive defect states in HfO_2 films. Two of these include both oxygen vacancies and interstitials [41]. Both of these are defects we know to exist in some of our films grown using a range of oxygen partial pressures with the intention of studying these defect types. Examples of these defect energy levels are

shown and discussed in this paper. Gavartin et al. concluded that thin films of HfO_2 have much higher defect densities than SiO_2 grown using similar techniques [42]. These same trends have also been seen in our IBS grown films. Gavartin, et al. further discuss HfO_2 films grown from metallic targets may have metallic clusters embedded in them. The conclusions of this work also show the propensity of HfO_2 to grow in columnar structures. Columnar growth can lead to point to point variation in the mechanical contact between interface layers and can strongly influence the heat flow through the film and across the boundary. This work further discusses the fact that HfO_2 surface and bulk defect levels can be as high as two orders of magnitude that of SiO_2, again grown using similar techniques, which is further substantiation of the findings already discussed in other work [43]. Post deposition annealing of these films was able to reduce this defect density by roughly an order of magnitude [44]. An important observation in these groups' research was the fact that when HfO_2 films are grown thinner than 2nm the defect densities are kept much lower. In light of our results, discussed later in the thesis, this critical dimension of 2 nm should be studied further.

LIDT testing of E-beam and laser evaporated HfO_2 films at 248nm using a 20ns pulse on $\lambda/4$ thickness films damaged at 2 J/cm^2 and 4 J/cm^2 respectively. Dual Ion Beam Sputtered (DIBS) HfO_2 damage tested at 308nm using 15ns pulses damaged at 3 J/cm^2. E-beam HfO_2 tested at the same wavelength damaged at 7 J/cm^2 [45]. These kinds of comparisons are the reason many groups in the past have considered E-beam coating better for use in high damage threshold applications.

Work with ion beam sputtered coatings for λ=1064nm and damage tests using 12ns pulsewidths was done by Xinghai Fu et al. [16]. Their work found slightly SiO_2 doped films of Sc_2O_3 and HfO_2 demonstrated damage onset value of 10 J/cm^2 and 7 J/cm^2 respectively. These

values were found using spot sizes of ~70 microns with slightly higher values recorded for 50 micron spot sizes. Some of our more recent work with these same materials has demonstrated the highest LIDT values for both HfO_2 and Sc_2O_3 films we have seen for any coating process reported in literature. These results are presented and discussed in chapter six.

Foster, A. S. et al. found that annealing HfO_2 in oxygen above 500°C results in crystalline, fully stoichiometric films. Working with ZrO_2, a very similar material to HfO_2 due to homological outer shell electronic configuration, suggests that oxygen diffuses from the surface into the bulk of the material in atomic form [46]. Again, as with HfO_2, oxygen interstitials and vacancies are common defects in ZrO_2. Interstitials and positively charged oxygen vacancies can trap electrons near the bottom of the conduction band in both HfO_2 and SiO_2 [46]. This defect signature is detectable using electron paramagnetic resonance (EPR) scans and examples of these types of defects will be presented and discussed later in this paper.

Previous Work Specific to Scandia

Sc_2O_3 thin films, by contrast, have received much less attention, likely due to their increased cost and difficulty to purify. Nevertheless, the allure of a higher band gap material for use in high damage threshold coatings has resulted in several exploratory efforts over the years.

Early work on Sc_2O_3 showed resistive heater evaporated scandia was oxygen deficient unless grown in a reactive atmosphere [47]. This group also found post deposition annealing of reactively grown Sc_2O_3 increased the absorption coefficient when compared with the as grown values.

Dip coated films of Sc_2O_3 were grown for use at 351nm by D. Grosso [3]. The resulting films had an optical index of n = 2 at 351nm and a bang gap of 5.7eV. These films had a porosity

of 16% and a measured damage threshold of 8.4 J/cm^2, using a multiple pulse per test site, N-on-1 testing technique. These measurements were made at 351nm using a 0.7ns S polarized beam at 45deg to the test optic's surface. HfO_2 films tested using the same conditions measured 14-15 J/cm^2 onset values.

Metal Organic Chemical Vapor Deposition (MOCVD) of Sc_2O_3 films was investigated by Xu, Z et al. [48]. Their work studied the relation between the optical index and the substrate temperature during film growth. The films grown at 450°C were amorphous and had low surface roughness. Those films grown at higher temperatures were progressively more crystalline resulting in a denser film with a more lossy interface due to surface scattering. The densification of the films grown at higher substrate temperatures resulted in higher optical index materials.

Liu, Guanghui et al. studied E-beam deposition of Sc_2O_3 as the substrate temperature was varied to monitor this influence on the material properties and LIDT performance [49]. Films grown at 50°C were amorphous but signs of crystalline growth were beginning to be seen when the substrate temperature was 150°C. At this point it is worth noting a low temperature crystallization of Sc_2O_3 was also seen in portions of the work we conducted at Colorado State, but owing to other factors that data is not discussed beyond this confirmation. The band gap of these materials, studied by Liu Guanghui et al., decreased as the substrate temperature increased. Damage testing in their case was done using pulses of 8ns at λ= 355nm with a spot size of 440 microns. The damage threshold was 2.6 J/cm^2 for films grown at 150°C and 1.1 J/cm^2 for films grown at 250°C.

Additional work on E-beam deposited Sc_2O_3 was carried out by Al-Kuhaili, M.F. et al.. They were interested in the influence of substrate temperature and oxygen partial pressure on the

material properties of the films produced. They saw crystallization of the Sc_2O_3 at 300°C with amorphous films being grown at lower substrate temperatures [50].

L. Chang et al. worked on pulsed laser deposition of Sc_2O_3 [51]. They suggest that this method of deposition might allow the target to remain stoichiometric as opposed to preferentially sputtering away the lighter elements. This work studied the influence of oxygen pressure on the properties of the films produced. They saw slightly too much oxygen in their films when grown at higher O_2 pressures.

De Rouffignac et al. grew Sc_2O_3 films using atomic layer deposition [52]. Their films showed increased crystallinity when heated to 450°C and another phase change when heated to 1000 °C. Their material also showed slightly too much oxygen after deposition. In their work this was attributed to trapped hydroxyl groups.

Work on other metal oxides that specifically address excessive oxygen content after deposition include Vink, T.J., et al. and Pérez-Pacheco, Argelia et al. where physically trapped oxygen was found in reactively sputtered MoO_3 [53] and reactive DC sputtering of TiO_2 [54].

Earlier work on how the process conditions of ion beam sputtered material influence the material and optical properties of Sc_2O_3 was reported by our research group in Menoni et al. Damage testing results at 50fs, 1ps and 400ps were reported [7]. Further work by our group was published in Langston et al. where the conclusions of the study are summarized in the quoted abstract below.

> We show that the concentration of oxygen interstitials trapped in Sc_2O_3 films by ion beam sputtering from metal targets can be controlled by modifying deposition conditions. We have identified point defects in the form of oxygen interstitials that are present in Sc_2O_3 films, in significantly high concentrations, i.e., ~1018 cm^{-3}. These results show a correlation between the increase of oxygen interstitials and the increase in stress and optical absorption in the films. Sc_2O_3 films with the lowest stress and optical absorption loss at 1 μm wavelength were obtained when using a low oxygen partial pressure and low beam voltage [6].

Representative Damage Testing on HfO_2 and Sc_2O_3 Done at Atmosphere

Of course our principle interest in these materials and their thin film properties is for their use in optical coating for NIR lasers with high damage threshold applications. As mentioned before, many groups have been working on increasing the laser damage performance of metal oxide coatings for some time. For the sake of orienting the reader to some of the historical work as well as the recent research we will highlight some of the more applicable results next.

M. Mende et al. published work on Ion Beam Sputtered (IBS) mixed oxides of Sc_2O_3 and SiO_2 [55]. This work was an effort to correlate optical, material, and substrate qualities to the laser damage performance of the films produced. Two different sources were used for the damage testing. One light source was a 510 fs, λ=1030nm laser using a spot size of 40 microns at $1/e^2$. The second laser was a 5 ns, λ=355nm source testing with a 200 micron spot. The Sc_2O_3 single layers tested had an onset value of >5 J/cm^2 at λ=355nm and 3.1 J/cm^2 at λ=1030nm. It is also worth noting that the researchers recorded a slightly higher oxygen content in their films than would be expected for fully stoichiometric material.

L. Gallais et al. studied the relative LIDT performance of high index metal oxides [56]. Using a 500fs, λ=1030nm laser testing with a 49 micron 1/e spot size they tested ion beam sputtered $\lambda/2$ (at 1064nm) films of SiO_2, HfO_2, Ta_2O_5 and Sc_2O_3 all grown on fused silica. The highest threshold material was SiO_2 at ~ 5 J/cm^2 followed by Sc_2O_3 at 4.6 J/cm^2 then HfO_2 at 2.6 J/cm^2 and finally Ta_2O_5 at 1.7 J/cm^2. This ranking of damage thresholds follows well the predicted behavior (Equation 2) of these materials to a femtosecond laser source based on their relative band gap energies [2].

$$F_{th}\left(E_g, \tau_p\right) = \left(a + bE_g\right)\tau_p^{\kappa} \tag{2}$$

$E_g$is the band gap of the material, $\tau_p$is the pulsewidth of the laser, a and b are material dependent values and $\kappa \approx 0.30 \pm 0.03$.

X. Fu et al. recently tested composites of Sc_2O_3 and HfO_2 with SiO_2 using both a 500fs, λ=1030nm and a 12ns, λ=1064nm source [16]. These materials were ion beam sputtered and deliberately tested with small spot sizes to determine the material's intrinsic damage threshold as opposed to extrinsic defect driven damage. With only slightly doped Sc_2O_3 (< 2% SiO_2) the LIDT value measured was ~10 J/cm^2 at 12 ns and ~1.8 J/cm^2 at 500 fs. The values measured for HfO_2 were ~7 J/cm^2 at 12 ns and ~3.1 J/cm^2 at 500 fs. The concentration of SiO_2 was increased in each of these base materials to study the LIDT performance of tailored index materials. In all the cases studied they found the higher the concentration of the low index material, in this case SiO_2, the higher the LIDT performance of the material, with a corresponding decrease in the index of the film. These results were used to develop a numerical model of defect size and densities from damage onset data.

C. R. Wolfe et al. studied laser conditioning of HfO_2 and SiO_2 thin films [57]. This work compared E-beam deposited films with ion beam sputtered films. They recorded an increasing LIDT performance for films where moisture is driven off the surface. This would seem to contradict earlier work dealing with the same issue [58]. In their sample analysis, they identified a paramagnetic point defect in amorphous SiO_2 [57]. This defect originates from the fact that electrons fill oxygen vacancy states as a result of UV illumination. It was found that after conditioning of the test optics, E-beam films performed better than ion beam films in terms of their LIDT.

As energy is deposited into these materials by the laser there is a rapid buildup of heat in a very localized area. This rapid buildup of heat will necessarily greatly increase the local stresses in the films and the substrate. It is generally believed that if a thin film structure is under stress the film is more susceptible to laser induced failure [59]. While this is generally taken as fact, work done by Rainer, F., et al. does not show a strong correlation between film stress and damage threshold [37]. It is worth noting, however, that this work was done on E-beam deposited films which are known to be less stressy than higher energy deposition processes.

The Influence of Surface Water on the LIDT Performance of Thin Films

Atmospheric conditions can affect the LIDT of thin films owing to the fact that water and hydrocarbons inevitably adsorb to the film's surface. Previous work studying the influence of surface water on the damage performance of oxide thin films includes work done by Ling, X. et al. [58]. They found that water desorption from the surface of E-beam sputtered coatings reduced the LIDT performance of these films. Other independent work found that water on the surface of thin films tends to increase the damage threshold by increasing the thermal conductivity of heat away from the test site [36].

Additional research comparing the performance of E-beam deposited films with IBS and Ion Assisted Deposition (IAD) grown material, tested in air and vacuum, found a common spectral shift towards shorter wavelengths in the transmission spectra of the E-beam coatings. This shift is commonly associated with water vapor desorption. No spectral shift was seen in the IBS and IAD grown films. When LIDT testing these samples in vacuum they found a 5x reduction in the E-beam deposited film's damage threshold when compared with their in air values. Their conclusions were that the dehydration of the more porous E-beam films was

causing increased tensile stress in these films. The IAD and IBS coatings, which are much less porous, showed no change in their performance when tested in air and vacuum [60].

In chapter 6 of this dissertation we discuss the influence of vacuum on the LIDT performance of thin film metal oxides. Our research suggests other factors can play a dominant role in the reduction of the LIDT values of certain film types.

The Influence of Surface Hydrocarbons on the LIDT Performance of Thin Films

As was already mentioned, the presence of a very thin layer of carbon containing species are nearly always covering surfaces exposed to the atmosphere. This adventitious carbon may or may not be a major contributor to the damage performance of a test optic under normal circumstances but more substantial deposits of carbon certainly can be. Local enhanced concentration of carbon has been found inside the illuminated area of the laser spot by a number of different groups [33, 61].

The process by which carbon builds up inside the laser spot is known to be cracking of carbonaceous molecules by incident photons and/or by secondary electrons ejected from the optical surface. Becker describes a phenomenological model of this carbon deposition on silica from gaseous toluene using λ=532nm photons [33]. The absence of carbon contamination uniformly on the optic's surface suggests any chemical reactions must take place on the surface in the irradiated areas only. For this to be the case adsorption of toluene molecules on the surface is a necessary first step. The carbon deposits seen are more than a monolayer in thickness so to estimate the surface coverage rate without laser irradiation a Brunauer-Emmett-Teller (BET) isotherm description is used.

$$\theta(T) = \frac{Pe^{\frac{U_1-U_2}{RT}}}{(P_{sat}-P)\left[1+\left(e^{\frac{U_1-U_2}{RT}}-1\right)\frac{P}{P_{sat}}\right]} \quad (3)$$

In this expression θ is the surface coverage rate, U_1 is the interaction energy between the toluene molecules and the surface, U_2 is the interaction energy between the toluene molecules themselves, P is toluene partial pressure, P_{sat} is the saturation pressure of toluene, R is the gas constant and T is the temperature. The dissociation energy needed to drive carbon from toluene is ~3.8 eV requiring a two photon event at λ=532nm. At this wavelength a photolytic reaction begins the decomposition of toluene. After an extended period of exposure time to the laser irradiation the local temperature in the irradiated spot is seen to rise abruptly, ΔT ~ 250C. This temperature increase begins a pyrolitic reaction that greatly increases the thermal dissociation of toluene. The rate of thermal dissociation is described by the following expression.

$$k_{th}(T) = 10^{15,\ 45}e^{-\frac{371,\ 9x10^3}{RT}}(s^{-1}) \quad (4)$$

Similar work done at λ=1064nm with a pulse width of 3.5ns [62] also saw carbon deposition even though the peak fluences tested were < 10^9 W/cm^2, far below the intensities needed to drive four photon processes needed for unassisted photolytic reactions. Their work suggests some type of photo catalytic process may facilitate the chemical dissociation of toluene. This type of carbon contamination has been shown to reduce the LIDT performance of optical surfaces by as much as an order of magnitude [62]. LIDT testing on metal oxide thin films have also demonstrated this decrease in the damage onset values with carbonation [63]. A discussion

of the mechanism by which this growth occurs from gaseous toluene is also given by R. R. Kunz et al.[64].

The work done by Becker S. et al. is of particular interest to our work given that their research was specific to ion beam sputtered films [33]. In their study IBS grown films were shown to be less susceptible to hydrocarbon contamination due to the fact that IBS films are more dense, fully closed surfaces that present fewer features for contaminant adsorption.

Surface Defects and Their Creation

When studying the interaction of light with the thin film materials it is necessary to understand how a surface is distinct from bulk material. In the case of a crystalline material the bulk is often characterized in terms of its macroscopic properties, i.e. density, optical index, band gap, hardness etc. These easily measureable macroscopic properties are a consequence of the microscopic arrangement and bonding of the elements that make up the material. On a microscopic scale a bulk crystal is characterized by the bond strength, the arrangement of the atomic nuclei in a matrix and the periodic spacing of these nuclei along crystal axes.

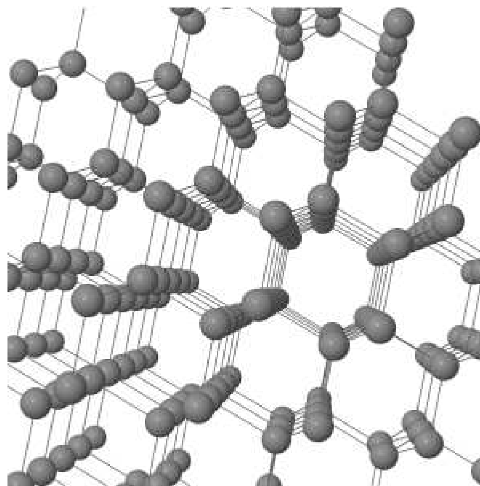

Figure 4: Generic crystal lattice

The principle assumptions that are made when discussing a bulk material are that the material is continuous and uniform. Figure 4 [98] is a representation of bulk crystalline structures such as carbon, silicon, silica or other covalent materials. The bulk is in fact composed of huge numbers of molecules arranged in a self-repeating matrix. Figure 5 [65] shows two silicon atoms from a larger matrix like the one depicted above of SiO_2. These two silicon atoms sit inside four oxygen atoms arranged in a tetrahedron. The oxygen atoms are shared between two tetrahedra in what is called a networked covalent bond, or shared electron pair bonds. Each silicon atom is said to have a half share in all the surrounding oxygen atoms resulting in the SiO_2 stochiometric ratio, 4 x ½ = 2 [65].

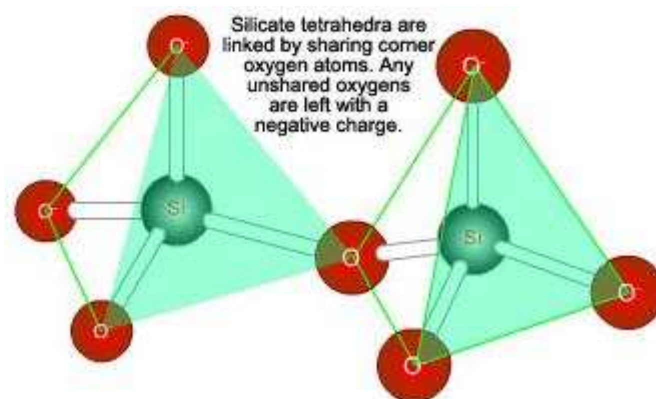

Figure 5: Silicon-oxygen bond arrangement [65]

Figure 6 [66] shows the molecular arrangement along the different axis of a quartz crystal. As can be seen the microscopic arrangement and bonding of the constituent elements and the molecules they form can result in a different lattice parameter which will then influence many of the macroscopic properties we generally associate with quartz and other crystalline materials, like optical index and hardness.

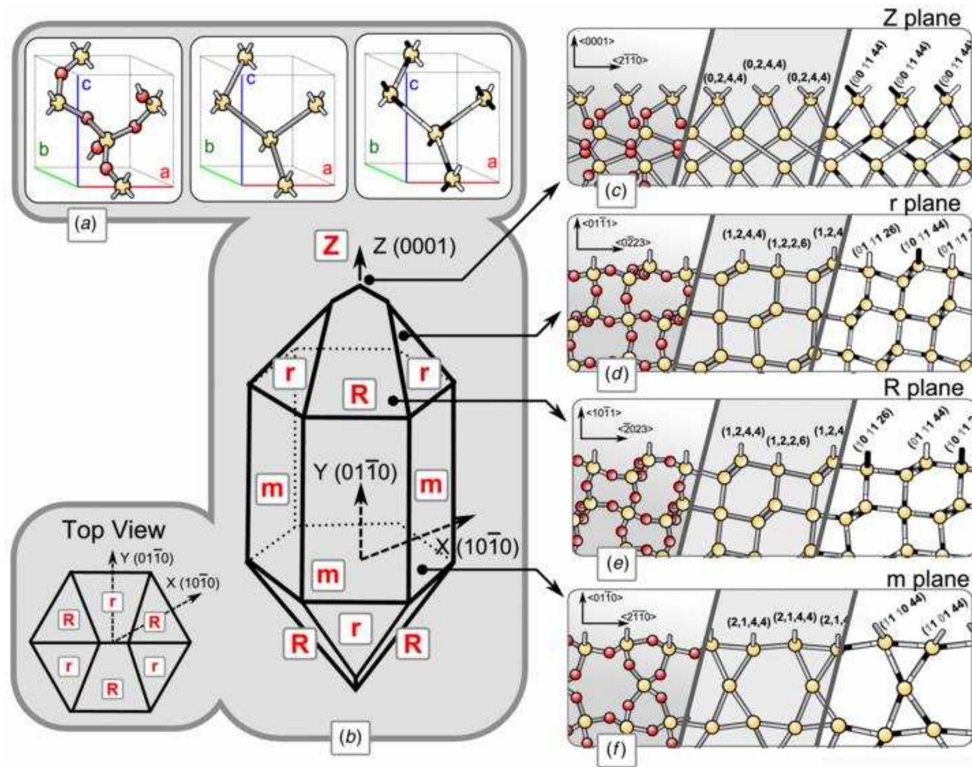

Figure 6: Quartz crystal lattice structure [66]

Like many other materials, SiO_2 can also exist in an amorphous state as opposed to the crystalline quartz we just discussed. What is meant by amorphous is a lack of large scale order in the bulk material. While the SiO_2 molecule still preserves a certain range of bond angles the tetrahedral with four oxygen atoms does not repeat over long unit cell distances. In almost all amorphous materials some areas of local order still exist, but if these features are <10 nm in extent the material is generally considered to be fully amorphous. Figure 7 [67] shows single crystal silicon with an amorphous layer of SiO_2 grown on top. Amorphous materials can be quite homogenous without being periodic and are not observation angle dependent in terms of either their microscopic or macroscopic properties.

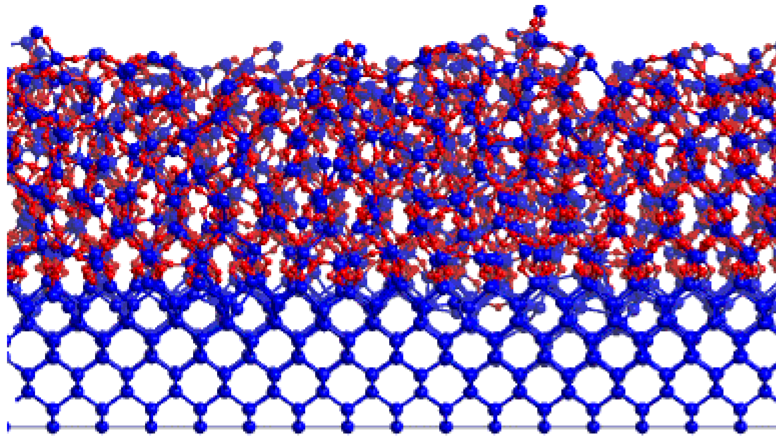

Figure 7: Amorphous SiO_2 grown on single crystal silicon [67]

Bulk materials, either crystalline or amorphous, behave very differently from monolayers or thin films. Due to the electromagnetic interactions inside the bulk, the homogenous materials enhance the electronic and vibrational coupling throughout the bulk. This close coupling allows the material to behave as an extended three dimensional single body. The periodicity and electronic arrangement, or the average intermolecular spacing and bond lengths if working with an amorphous material, are not interrupted in any given axis even though the material's properties may differ along different axes, in the case of a crystal. At an interface, or surface, the periodicity or average intermolecular spacing is interrupted. These discontinuities result in a greatly increased number of scattering sites for either electrons in the case of conductors or phonons in the case of insulators. This fact greatly influences the thermal and electrical properties of these materials. Another important consequence of a surface or interface is the fact that the bonding environment for the molecules at the surface is incomplete. Any unshared oxygen atoms in the SiO_2 molecule is thus negatively charged. These dangling bonds can be optically sensitive in one of two ways. First, these charged oxygen atoms can quickly bond to impurity. Second, if the bond is left dangling these electrons that are ordinarily coupled to the

silicon ion are able to inelastically interact with the electric field from an intense laser source possibly leading to a reduced LIDT performance. Give the extremely large number of broken or dangling bonds at a surface this electronic environment predominates at the surface.

Other work has found that strained bonds can cause disorder related defect states that can absorb single photons in high band gap materials [59]. These states may also enhance the absorption cross section for two photon events. Surface specific defects have been shown to be created in the form of E' centers which can serve as electron traps [68]. These defects can be created by mechanically abrading the surface of SiO_2.

Earlier work using high average power Ar+ lasers on metal oxide films showed a decrease in the transmission of these films when used in vacuum [69]. This behavior was ascribed to either photoinduced oxygen depletion or color center creation. It was found that if these films were not too degraded, in terms of their absorption, they could recover the original transmission by exposing the surface to both oxygen and the laser light.

Semiconductor work on oxygen diffusion barriers has demonstrated O_2 diffusion from an SiO_2 layer through 30 nm of tungsten at 400°C [70]. This work demonstrates the difficulty in stopping oxygen diffusion through very dense materials.

Material defects such as grain boundaries and microcracks allow increased thermally activated oxygen diffusion through the barrier material. The increased density of sputtered metal oxides provides greater resistance to oxygen diffusion when compared with evaporated films [71].

He, J.Q., et al. studied the diffusion of oxygen through SiO_2 and found that amorphous thin films had a diffusion rate five times higher than fused silica [72]. A faster oxygen diffusion

rate is expected through amorphous HfO_2 when compared with crystalline HfO_2 due to the reduced mass density of the amorphous films.

It stands to reason that it is more difficult for an oxygen diatom to diffuse through a solid material than for a single oxygen atom. An energy of 3.79eV is needed to dissociate one oxygen atom from an Sc_2O_3 molecule [73]. This value of ~3.8eV is significant as it equals the energy needed to chemically dissociate Toluene as was discussed earlier [33]. The fact that one micron light was capable of cracking the carbonaceous molecules demonstrates the possibility of similar reactions taking place in Sc_2O_3, or on other oxides, using only ~1eV photons.

Vacuum annealing has been shown to slightly reduce the surface of a TiO_2 thin film creating single oxygen vacancies [74].

Several groups have noted the electrical and chemical properties of ZrO_2 and HfO_2 are so similar that their oxygen diffusion coefficients are nearly identical and more importantly very high [75, 99]. Values for the ionic conductivity of ZrO_2, in which oxygen was the only significant contributor to the current flow, were measured by Arun Kumar et al. [75]. Their experiments were performed as a function of temperature and oxygen pressure. For temperatures below 600°C a more subtle dependence of the ionic conductivity was seen on the oxygen pressure when compared with the higher temperature tests. At atmospheric pressure the conductivity was measured to be ~$5*10^{-7}$ mho/cm. Using the Nernst-Einstein relation [76]

$$\kappa_{ion} = \frac{4F^2 D^*}{V_m RT} \tag{5}$$

where F is the Faraday number, D* is the oxygen diffusion coefficient, V_m is the molar volume of oxide, R is the gas constant and T the temperature, we can determine the oxygen diffusion

coefficient from the ionic conductivity. Below 600°C the oxygen diffusion coefficient for HfO_2 is ~ $2.11492*10^{-12}$ cm^2/s, while at 900°C the diffusion coefficient is closer to $3.12586*10^{-10}$ cm^2/s. These values decrease slightly with decreasing oxygen pressure only to increase again under high vacuum conditions.

This rapid diffusion of oxygen through HfO_2 can be greatly reduced, however, with the addition of Al_2O_3 in the film [77]. Al_2O_3 by itself has been observed to have a significantly higher resistance to oxygen diffusion when compared with HfO_2. Efforts specifically aimed at studying the ability of Sc_2O_3 buffer layers at impeding the diffusion of oxygen have found that Sc_2O_3 is a poor barrier material for oxygen diffusion [78].

Thin Film Metal Oxide LIDT Behavior in Vacuum

Previous work on vacuum damage testing of metal oxides found that E-beam deposited films perform better with neutral or even slightly compressive stress in the coating to help reduce the cracking or crazing of the film [80].

J. A. Kardach et al. studied the laser damage performance of over twenty different E-beam deposited metal oxides and fluorides in vacuum (10^{-8} torr) including HfO_2, Sc_2O_3 and SiO_2, specifically the emission of photoelectrons below and above the LIDT value of the films. They were using a 5ns, λ=1.06 micron laser with a ~300 micron spot size. Their work found that the damage threshold depends strongly on the thermal properties of the substrates used. Higher conductivity substrates damage at higher fluences. These tests were performed over many hours on a single test optic and confirmed earlier work suggesting the ability to condition optical surfaces by illuminating a test site below the damage threshold driving off near surface defects

[81]. Additional work by Lange et al. discusses the substrate's ability to influence the LIDT value tested in air, but this was expected for longer pulse testing not 5ns or 0.5ns pulses [82].

Other vacuum damage research found that a reduced gas heat conduction has very little effect on the peak temperatures seen in the coatings before and during damage [83]. These findings are consistent with the thermal modeling we present for our data showing little difference in the in air and vacuum thermal dissipation.

A comparison of E-beam deposited films with IBS and IAD grown films, tested in air and vacuum, showed that the denser IBS and IAD films perform much better than the E-beam films in vacuum. This improved performance was attributed to negligible water desorption from the surface of the denser films while the E-beam coatings were strongly affected by the off gassing of water [60].

S. Tamura et al. damage tested E-beam deposited Sc_2O_3 grown on fused silica (FS) in vacuum. The laser used was a 400ps, λ=355nm source. The spot size was 350 micron $1/e^2$ [84]. The results showed SiO_2 half wave thick films damaged at 4.6 J/cm^2 while Sc_2O_3 quarter wave films damaged at 2.3 J/cm^2. Anti-reflection stacks composed of Sc_2O_3/SiO_2 and Sc_2O_3/MgF_2 were also tested and showed very similar performance for films grown on an undercoat of SiO_2 deposited on the FS. When testing these films on the native FS surface the Sc_2O_3/MgF_2 films performed better than the Sc_2O_3/SiO_2. Similar work was done by the same group on high reflection coatings grown using the same materials, Sc_2O_3/MgF_2, also grown using E-beam deposition [85]. In this study it was found that oxides grown using higher deposition rates and higher oxygen pressures resulted in higher damage threshold values for the films produced. These results may help support the assertion that intermediate deposition energies are favored over both lower and higher deposition energies for damage threshold purposes.

Studies of the effects of a vacuum environment on IBS grown HfO_2 and SiO_2 thin films deposited at CSU was done by D. Nguyen et al. at the University of New Mexico [34]. They tested in air and in vacuum LIDT performance of these films as a function of pulse count and partial pressure. They also collected data on the influence of water vapor, nitrogen, oxygen and toluene on the LIDT performance of multishot testing. The base pressures tested were $\sim 3*10^{-7}$ torr and there were no in vacuum cleaning efforts made on the test optics. They saw no nitrogen or toluene influence on the LIDT performance of the films tested, however, they reported a partial improvement in the LIDT value with the introduction of molecular oxygen into the atmosphere surrounding the test optics. With the introduction of water vapor there was a complete restoration of the multishot LIDT performance of these films. They attributed the improvement in the performance both to the presence of oxygen and water. Bulk FS did not show a pressure dependence on its LIDT performance but no suggestions were given to explain this behavior. The authors suggest oxygen vacancy formation and possibly surface charging are responsible for the observed behavior of the thin films.

Metal Surfaces in Vacuum

Ultra high vacuum laser damage studies, 10^{-11} torr, on pristine copper surfaces found that copper damages at a higher fluence in vacuum than in air. The reason for this increased performance is believed to be little or no plasma formation directly on top of the surface immediately preceding the damage event. This plasma, just as with metal oxide damage events, is formed when near surface defects are super-heated and ejected from the surface. This ejected volume continues to heat in the laser field imparting energy to the test optic's surface while in close proximity. With no air above the surface to impede rapid expansion away from the target,

any plasma that is created would have less opportunity to damage the surface [86]. While there is a fundamental difference in the damage performance of metals compared with oxides, especially in vacuum, these results do apply to our work and will be discussed again in chapter 6.

Capping Layers for the Protection of Optical Coatings

A number of previous efforts have been directed at studying the impact of capping layers on the LIDT performance of thin films [87-95].

F. Rainer et al. studied the influence of both overcoat and undercoat layers on the laser damage performance of E-beam deposited HR and AR films of Sc_2O_3 paired with either SiO_2 or MgF_2 [87]. The influence of substrate material and temperature were also studied. They studied Sc_2O_3/MgF_2 high reflectors (HR) with either SiO_2 or MgF_2 half wave thickness overcoats at λ=248nm. They also studied AR films of Sc_2O_3/MgF_2 and Sc_2O_3/SiO_2 with half wave undercoats of SiO_2 and MgF_2. Their results showed that the overcoating improved the LIDT performance of all samples tested but that the MgF_2 improved more than the SiO_2. Thin film crazing was observed in the films grown on FS, likely due to differences in the coefficients of thermal expansion. All measurements in this work were made at λ=248nm and a pulse duration of 20ns. The median LIDT values of the different films tested without an overcoat was 3.1 J/cm^2 while the addition of an overcoat increased this value to 6.3 J/cm^2. Additional work by another group at λ=248 nm with similar materials showed similar results [88].

S. Tamura et al. also studied the influence of SiO_2 and MgF_2 capping layers on Sc_2O_3/SiO_2 HR films for use at λ=355nm [89]. These films were E-beam deposited and tested using a λ=355nm source with a 0.4ns pulsewidth and a 350 micron 1/e^2 spot size. HR films with a half wave thickness overcoat of SiO_2 showed a 25% improvement in their LIDT values. The

samples capped with a half wave of MgF_2 showed no improvement over the uncapped films even though MgF_2 has a higher band gap than SiO_2. The authors attribute this to a likely increase in the mechanical stability of the surface with the SiO_2 overcoat. Other LIDT work, at λ=1μm, agrees that the mechanical stability of the overcoat is a likely reason for a portion of the improvement in the damage threshold with the addition of a capping layer [90]. Stolz et al. suggest a combination of factors including a reduced electric field strength inside the high index material as well as the additional mechanical stability this half wave layer of SiO_2 both contribute to the improved LIDT values [91]. Damage testing E-beam deposited HR films with half wave overcoats of SiO_2 and MgF_2 using a λ=355nm, 8ns pulse duration laser source showed the SiO_2 overcoat increased the LIDT but the MgF_2 overcoat did not. The authors did not have an explanation for this behavior [92].

Wu Z. et al. worked with E-beam deposited films of HfO_2 and SiO_2 grown from Hf and SiO_2 targets suggests that if the overcoat has a higher thermal conductivity than air, it may play a major role in increasing the LIDT performance of the film. This would be accomplished by locally averaging and lowering the peak temperatures seen in the film [93]. This work also found that thicker overcoat layers were less likely to delaminate off polarizers. Delamination typically grows with additional pulses on the same test site and so it represents a particularly debilitating damage type. The results of their work imply very thin overcoat layers will be less mechanically stable than thicker layers [91].

Yao et al. studied TiO_2/SiO_2 HR mirrors for use at λ=532nm and λ=800nm. A half wave capping layer of SiO_2 was grown on these films. Damage testing the coating stacks at λ=532nm showed a 20% improvement in the LIDT values with the capping layer, while adding a full wave capping layer of SiO_2 on the λ=800nm films improved the LIDT values by 50%. The authors

attribute this effect to a many orders of magnitude difference in the thermal conductivity of SiO_2 over air. This should reduce the peak temperatures in the film for equivalent pulse energy and absorption [94].

Topcoat work on two of the materials discussed in this dissertation, HfO_2/SiO_2 and Sc_2O_3/SiO_2 coating, was done by S. Papernov et al. [95]. They studied different configurations of basecoat and topcoat films to judge the relative performance of these relatively thin structures, 25nm – 50nm. LIDT testing was done using a 0.7ns Nd:Glass slab laser. Their work was based on the assumption of nanoscale absorbing clusters as the only absorbers in these materials. The results of this work suggested that the HfO_2 films had 10nm sized absorbing defects. Thermal modeling was performed using Ansys to describe the local effects of nanoscale absorbers on the surrounding thin film material. Their work suggests that buckling of the topcoat happens before reaching the melting temperature of the thin film materials. The modeling required extremely high temperatures to describe the damage process as well as very high absorption at these local absorbers. LIDT testing found HfO_2 based films damaged at 5.6 J/cm^2 while the Sc_2O_3 based films damaged at 5.4 J/cm^2.

CHAPTER III. INTERFERENCE COATINGS

Interference coatings are stacks of non-absorbing materials whose spectral response is controlled by selecting the optical path length of each layer. This spectral response directly derives from Maxwell's equations. From the solution to Maxwell's equations in a continuous medium we have a description of a forward propagating electromagnetic wave with an electric field amplitude of E_0, angular frequency ω, traveling in the y-direction with speed c/n_r.

$$\vec{E} = \overrightarrow{E_0} \cos \omega(t - {}^{\tilde{n}y}/_{c}) \quad (6)$$

where $\tilde{n} = n_r - ik$

In this expression k and n_r are the imaginary and real components of the complex index of refraction. Specifically, the real part of the refractive index describes the wavelength dependent relative phase velocity of an electromagnetic wave in a material. The imaginary component accounts for absorption loss. In a lossy material, a non-zero free current density, J, proportional to the electric field and free charge density may not be zero. The modified wave equation then takes the following form:

$$\nabla^2 E = \mu\epsilon \frac{\partial^2 E}{\partial t} + \mu\sigma \frac{\partial E}{\partial t} \quad (7)$$

The last term in this expression describes the time dependent rate of change of the electric field which gives rise to electric potentials which give rise to currents. If the material is not a perfect conductor these currents generate losses which are optical absorption.

Of course there is the corresponding equation for the magnetic field which is not shown here. The solutions for these modified equations are similar to the earlier expressions but with the additional requirement that the wave number be complex.

$$k^2 = \mu\epsilon\omega^2 + i\mu\sigma\omega \qquad (8)$$

This expression is commonly written in the following form:

$$\tilde{k} = k + i\kappa \qquad (9)$$

where $k = \omega\sqrt{\frac{\mu\epsilon}{2}}\left[\sqrt{1+(\frac{\sigma}{\epsilon\omega})^2}+1\right]^{1/2}$

and $\kappa = \omega\sqrt{\frac{\mu\epsilon}{2}}\left[\sqrt{1+(\frac{\sigma}{\epsilon\omega})^2}-1\right]^{1/2}$

In the case of a wave traveling through a lossy material the solutions then takes the following form:

$$\vec{E} = \overrightarrow{E_0}e^{-\kappa y}\cos(ky-\omega\, t) \quad \text{or} \quad \vec{E} = \overrightarrow{E_0}e^{-\kappa y}e^{i(\omega t-ky)} \qquad (10)$$

The complex component of the optical index describes the absorption of light in a material. Using a simple Beer's law description and substituting terms from the decaying exponential in the above solutions gives us a familiar expression for the absorption coefficient of a material.

$$I(y) = I_0 e^{-\alpha y} \rightarrow \alpha \equiv 2\omega k/c \quad (11)$$

Interference films, by design, attempt to eliminate all absorption at the wavelengths of interest. If we then assume a lossless material in our present discussion, Fresnel reflections and subsequent transmission dictate the response of interference coatings to different wavelengths of light.

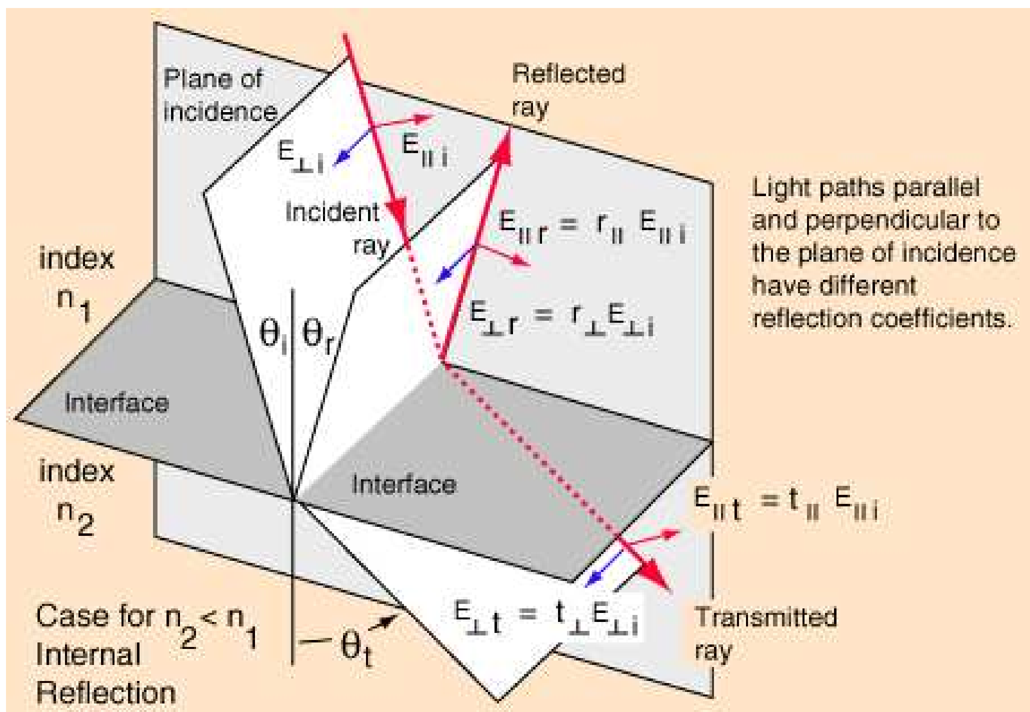

Figure 8: Light at an interface [100]

Where the reflection coefficients are given by:

$$r_{parallel} = \frac{\tan(\theta_i - \theta_t)}{\tan(\theta_i + \theta_t)} \quad (12)$$

$$r_{perpendicular} = -\frac{\sin(\theta_i - \theta_t)}{\sin(\theta_i + \theta_t)} \quad (13)$$

And the transmission coefficients are:

$$t_{parallel} = \frac{2\sin\theta_t \cos\theta_i}{\sin(\theta_i + \theta_t)\cos(\theta_i - \theta_t)} \tag{14}$$

and

$$t_{perpendicular} = \frac{2\sin\theta_t \cos\theta_i}{\sin(\theta_i + \theta_t)} \tag{15}$$

Figure 8 depicts the incident, reflected and transmitted wave as a function of polarization and angle of incidence. If additional layers, or interfaces, are grown then we have successive interfaces each of which contributes not only to the reflected wave but also to the transmitted.

The optical thickness of the individual layers can be controlled with enough precision to tailor the contribution of these individual interface responses such that the total optical response can be engineered. Figure 9 shows a front and back surface response from a single layer in air.

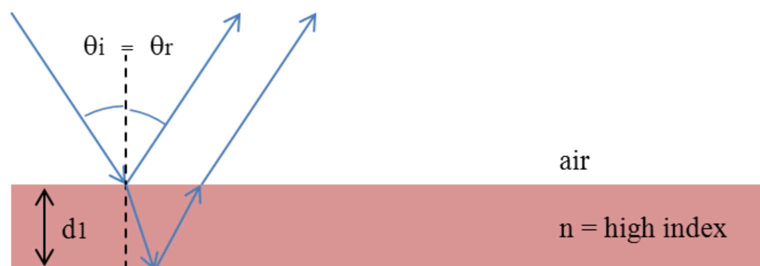

Figure 9: Single layer in air

Equations 12 through 15 are satisfied for a single interface. In a multilayer film the contributions from multiple interfaces add when the following condition is met:

$$d_1 \cos(\theta_i) = (2m+1)\frac{\lambda_1}{4} \quad (16)$$

where λ_1 is the wavelength of light in the material of interest, d_1 is the physical thickness of the layer in question and m is an integer, m = 0, 1, 2, …. For destructive interference instead the following condition is met.

$$d_1 \cos(\theta_i) = 2m\frac{\lambda_1}{4} \quad (17)$$

These expressions account for the half wave phase shift that occurs at an interface when the wave travels from a low index material to a high index material, which does not occur when the wave travels from a high index material to a low index material, as shown in figure 10.

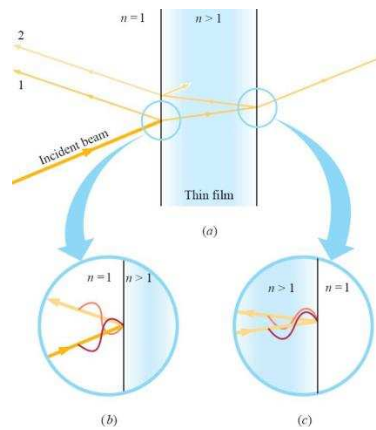

Figure 10: Phase shift at an interface [101]

These simple expressions can be generalized to structures with multiple interfaces (Figure 11) to further enhance or reduce the reflection of an electromagnetic wave from a multilayer structure.

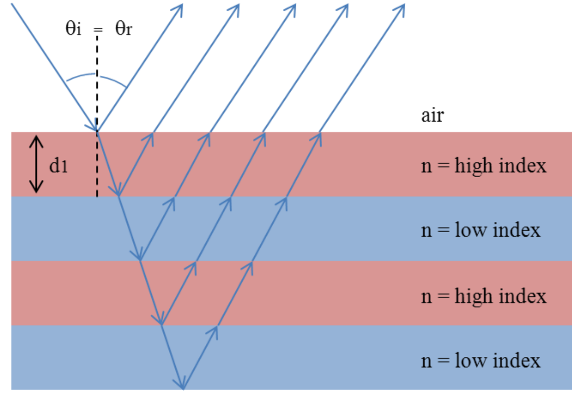

Figure 11: Multiple surface reflections

If we consider a linearly polarized plane wave normally incident on a sequence of thin films composed of homogeneous and isotropic materials separated by parallel featureless surfaces we can describe the reflected and transmitted waves using the so called Matrix Model [102]. The reflected and transmitted waves will preserve the plane of polarization of the incident wave and the phase factor of the wave is given by $e^{[i(\omega t-kz)]}$. The characteristic admittance of the surface is defined as the ratio of the magnetic and electric field amplitudes, 'y'. The matrix model begins by describing the tangential electric and magnetic fields at the final surface of coating stack. The transformation of the two fields from one interface to the next is given by a simple matrix multiplication where the film "*f*" is terminated by the interface *a* in front and interface *b* behind.

$$\begin{bmatrix} E_a \\ H_a \end{bmatrix} = \begin{bmatrix} cos\delta_f & \frac{isin\delta_f}{y_f} \\ iy_f sin\delta_f & cos\delta_f \end{bmatrix} \begin{bmatrix} E_b \\ H_b \end{bmatrix} \tag{18}$$

Here the phase thickness is given by $\delta_f = 2\pi(n - ik)\, {}^{d}/_{\lambda}$ where d is the physical thickness of the film and λ is the free space wavelength. For an arbitrary number of thin film layers the expression is written:

$$\begin{bmatrix} B \\ C \end{bmatrix} = \left\{ \prod_{j=1}^{q} \begin{bmatrix} cos\delta_f & \frac{isin\delta_f}{y_f} \\ iy_f sin\delta_f & cos\delta_f \end{bmatrix} \right\} \begin{bmatrix} 1 \\ y_{emergent} \end{bmatrix} \tag{19}$$

where B and C are the electric and magnetic field amplitudes at the incident surface.

Given that there is no counter propagating wave in the "emergent" material, or the material the wave exits into, the surface admittance of the "emergent" surface is the characteristic admittance of the emergent material, $y_{emergent}$. The reflectance and transmittance are then given by:

$$R = \frac{(y_0 B - C)(y_0 B - C)^*}{(y_0 B + C)(y_0 B + C)^*} \tag{20}$$

and

$$T = \frac{4 y_0 Re y_{emergent}}{(y_0 B + C)(y_0 B + C)^*} \tag{21}$$

where y_0 must be a real number.

If the surface off which the reflection is happening is not smooth on the scale of the wavelength of light, then that surface will scatter light (Figure 12). Scattering can take the form of either forward scattering light, in the case of transmissive optics, or backscattered light. The amount of light scattered is dependent on the roughness of the surface or interface.

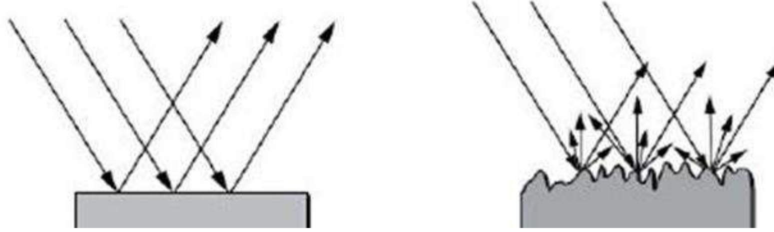

Figure 12: Specular vs diffuse reflections [103]

In multilayer structures interface roughness leads to losses. While roughness is generally not directly related to the laser damage performance of an optic except in extreme cases, it can result in a significant loss for an optical system. The loss term of greatest significance for laser damage studies is absorption. For the energy to be permanently transferred from the electromagnetic wave to the optical material some energy must be absorbed. In almost all cases, an increase in the low optical intensity absorption of a material will translate into a lower laser damage performance of that material. This increase is more pronounced when tested at long pulsewidths but is also seen in short pulse damage testing. The reason for this difference between short and long pulse damage threshold dependence on shallow defect concentrations is apparent when you consider the multiphoton absorption cross section. This cross section is expressed in units of Goeppert-Mayer (GM); 1 GM = 10^{-50}cm^4*s*photon^{-1}. In the case of long pulse excitation, with much lower peak intensities, there is little statistical probability that two or more photons will interact with a single electron at the same time.

$$\frac{d\Phi}{dz} = -N\sigma\Phi - N\sigma_2\Phi^2 \quad (22)$$

In equation 22 above Φ is the photon flux (in photons/(cm^2*s)), σ is the linear or single photon absorption cross section having units of cm^2 and σ_2 is the two-photon absorption cross

section in units of cm^4*s. N in this expression is the number of molecules or atoms the photon will interact with per unit length (cm^{-1}).

Models for Laser Damage

The mechanisms by which the radiation is transferred to the optical material during absorption have been the focus of a great deal of research over the years. Here it is necessary to make a distinction between low and high intensity absorption. In the low intensity regime absorption generally only happens due to impurities and intraband defect states. At high intensities direct multiphoton absorption and plasma absorption take place. A conceptual model of an ideal high band gap material is useful when discussing potential absorption mechanisms.

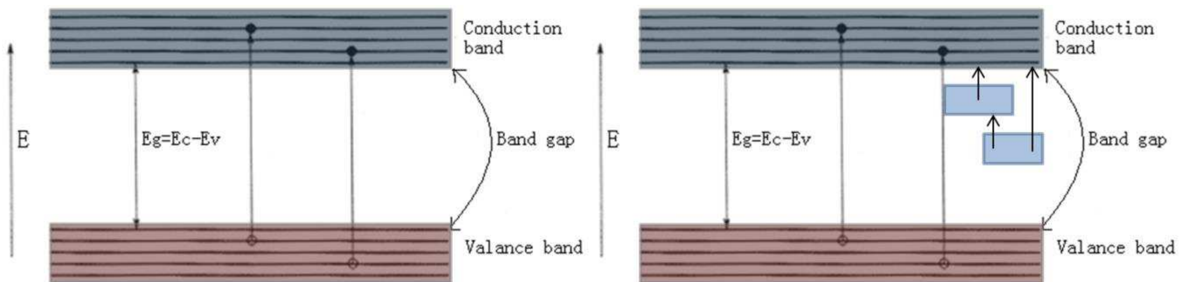

Figure 13: Idealized vs practical band gap [104]

The idealized band gap, depicted on the top in figure 13, is a theoretical model that is only useful as a reference for discussion. In practice, the band structure is complicated by the existence of defect states within the bandgap.

In an ideal crystal only intraband absorption is possible. In principle this mechanism is not present in metal oxides when the probe photon energy is below the band gap energy. If, however, there exists an intermediate defect site below the conduction band or above the valence band it is now possible for a lower energy photon to be absorbed by the material, as shown in

figures 13b and 14. In the case of an amorphous material these defects form broad bands within the band gap. Models describing the influence of optical absorption on materials have been developed based on this defect laden band gap structure. One such model, a rate equation model, keeps track of the electronic transitions that take place in a non-ideal high band gap material [105].

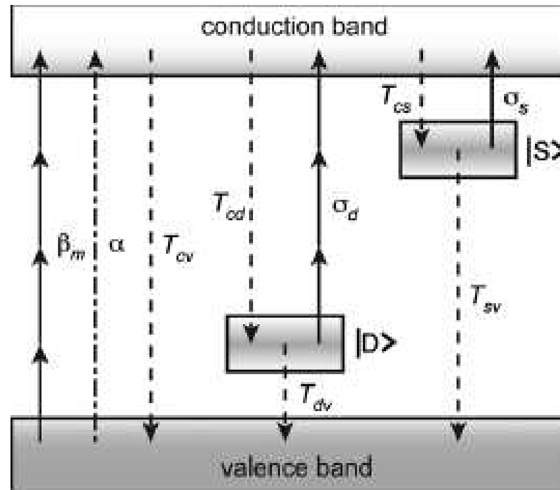

Figure 14: Transitions in a defect laden high band gap material [105]

From the depiction of a defect laden high band gap material shown in figure 14 a series of populating and depopulating terms for the different energy states can be written. These rate equations describing these processes are given in equations 23-25.

$$\frac{dN}{dt} = \alpha N(t)I(t) + \beta_m I(t)^m - \frac{N(t)}{T_{cv}} - \frac{N(t)}{T_{cs}}\left(1 - \frac{N_s(t)}{N_{s,max}}\right) + \sigma_s N_s(t)\left(\frac{I(t)}{h\nu}\right) - \frac{N(t)}{T_{cd}}\left(1 - \frac{N_d(t)}{N_{d,max}}\right) + \sigma_d N_d(t)\left(\frac{I(t)}{h\nu}\right)^{m'} \quad (23)$$

$$\frac{dN_s}{dt} = \frac{N(t)}{T_{cs}}\left(1 - \frac{N_s(t)}{N_{s,max}}\right) + \sigma_s N_s(t)\left(\frac{I(t)}{h\nu}\right) - \frac{N_s(t)}{T_{sv}} \tag{24}$$

$$\frac{dN_d}{dt} = \frac{N(t)}{T_{cd}}\left(1 - \frac{N_d(t)}{N_{d,max}}\right) + \sigma_d N_d(t)\left(\frac{I(t)}{h\nu}\right)^{m'} - \frac{N_d(t)}{T_{dv}} \tag{25}$$

$\alpha N(t)I(t)$ is the populating term due to avalanche ionization and $\beta_m I(t)^m$ is the increase in the conduction band electrons due to direct multiphoton excitation of order *m*. The following terms in the first expression are the depopulating terms due to conduction band to shallow defect relaxation $-\frac{N(t)}{T_{cs}}$, conduction band relaxation to valance band $-\frac{N(t)}{T_{cv}}$ and conduction band relaxation to deep defect states $-\frac{N(t)}{T_{cd}}$. The other excitation manifolds are to describe electron excitation from either the shallow or deep defects by means of linear or multiphoton absorption. The terms $\left(1 - \frac{N_s(t)}{N_{s,max}}\right)$ and $\left(1 - \frac{N_d(t)}{N_{d,max}}\right)$ are there to limit the maximum population density of these shallow and deep defect states. The σ terms are absorption cross sections for these processes. A full description of all these terms and their effect on the electron densities in these different states is given in Emmert et al. [105].

These expressions are meant to model the behavior of materials with preexisting defect densities, or those defects that exist as a result of material impurities, deposition related defects, surface abnormalities or handling errors. For laser induced defects to be included in these calculations additional excitation manifolds need to be considered.

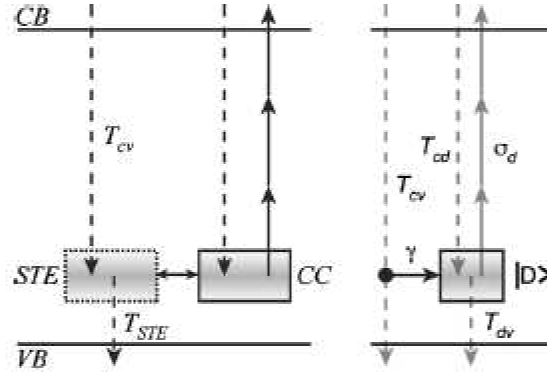

Figure 15: Induced defect states [105]

$$\frac{dN_{d,max}}{dt} = \gamma \frac{N(t)}{T_{cv}} \left(1 - \frac{N_{d,max}(t)}{N_0}\right) \tag{26}$$

In this case, shown in figure 15, the possibility of a long lived laser induced defect state is added to the original deep defect state already considered in the previous expressions as shown in equation 26. Laser induced defects states are incorporated into this model by allowing a small number of self trapped exitons (STE), defined by the branching ratio γ, to be converted into color centers [66]. Once converted to color centers these defects are treated like native deep defect states. Damage in these rate equation models is defined as the fluence that creates a conduction band electron density equal to the critical electron density for a plasma, which scales as $1/\lambda^2$ where λ is the wavelength of the illumination.

$$\omega_p = \sqrt{\frac{Nq^2}{\varepsilon_0 m^*}} \tag{27}$$

Equation number 27 is the plasma frequency expression as a function of wavelength.

A good description of the evolution of this absorption process in metal oxides is given by Stuart et al.

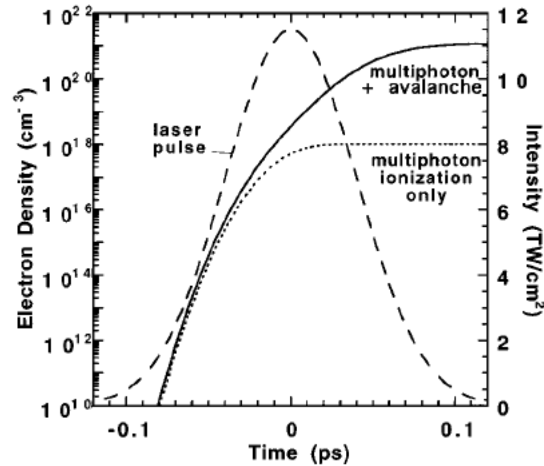

Figure 16: Conduction band electron density due to multiphoton ionization only and with the addition of avalanche ionization [15].

Figure 16 shows a rapid increase of electron density in the conduction band early in the laser pulse. These first electrons are promoted to the conduction band either by higher order absorption processes or from shallow defect sites that are one or two eV below the conduction band. At this point in the damage process the density of electrons in the conduction band is not sufficient to significantly affect linear absorption but in the presence of a strong electric field these electrons can be accelerated. If these electrons are given enough energy to drive additional electrons into the conduction band when they impact an atom, avalanche ionization can then take place.

At a wavelength of one micron a critical electron density is in the range of 10^{19} cm^{-3} - 10^{21} cm^{-3}. As might be obvious, laser damage at λ=1μm, in a high band gap material is not a purely linear absorption process as multiphoton absorption can take place. Of all the processes that can and do take place before and during a damage event two photon absorption and self-focusing are some of the higher order effects to be seen. When peak intensities approach a few GW/cm^2 two photon absorption starts to play a significant role [83]. As the peak intensities

continue to increase even higher order processes can occur but these are not a significant contribution at the pulsewidths of interest in this work, ~375 ps.

In the case of testing with one micron radiation the principle concern is with the shallow defect states, either preexisting or laser induced, that are within one or two eV of either the top or the bottom of the band gap. These states can be directly populated via one or two photon absorption and potential subsequent avalanche ionization. Additionally, cascaded single photon absorption events can occur. These types of cascaded events potentially yield much higher effective absorption cross sections than a single higher order process [10]. Any reasonable attempt to model these absorption processes must take all these manifolds into account including depopulating mechanisms. Modeling these processes requires one to estimate absorption cross sections, time constants and number of defect states, which can be difficult to evaluate. With the level of uncertainty that exists for these estimates and the many degrees of freedom that these systems have it is a significant achievement to have a numerical simulation produce numbers on the order of measured values. These facts help to explain the difficulty these models have in accurately predicting the outcome of any given set of tests.

In the process of photon absorption, a large population of phonons is created. The dynamics of the phonon population affect heat transport and therefore the thermal properties of the material. Assuming we have a sufficiently good understanding of these properties it may be possible to surmise information about the dynamic absorption of a material from the results of damage testing. Numerical modeling done on optical films grown in our IBS chamber has resulted in reasonable numbers for the required fluences to damage the different film types [106] but assumptions have to be made of the dynamic absorption mechanisms, some of which are difficult to measure. Improvements to our estimates of these absorption numbers can be made by

approaching the problem from a different perspective. By using the measured fluence necessary to cause damage onset together with the previously measured low intensity absorption it may be possible to get an estimate of the laser induced defect density and total dynamic absorption from thermal modeling. Uncoupling these estimates of laser induced defect densities from other likely absorption processes would be necessary as these models and measurements are refined, but preliminary results can certainly be used to bound the maximum absorption needed to initiate damage in these materials. Efforts we made in this regard are shown and discussed in the next chapter.

CHAPTER IV. ION BEAM SPUTTERING OF METAL OXIDES

Ion beam sputtering (IBS) is the process of driving material from a solid phase target into a vapor phase by means of eroding a surface with accelerated noble gas ions that are directed at a target. Depending on the sputtering conditions this vapor phase sputtered mass is directionally ejected from the target and deposited onto a substrate. Our metallic thin film dielectrics were grown by reactive sputtering.

As was discussed in chapter 2, IBS thin dielectric films have been grown and studied extensively. While commercially available dielectric IBS films are relatively common, the process conditions used to grow these films and the influence these conditions have on the optical and mechanical performance of these structures are still the subject of active research. In what follows, I summarize the main characteristics of metal oxides grown by IBS.

M. Mende et al. found that IBS films of Sc_2O_3/SiO_2 mixtures tend to show slightly higher oxygen content than is necessary for fully stoichiometric material [55]. They found damage onset values for single layers of Sc_2O_3, tested at 5ns, 355nm with a 200 micron spot size ($1/e^2$) of just over 5 J/cm^2. When tested at 510 fs, 1030nm, using a 40 micron ($1/e^2$) spot size the damage threshold was 3.1 J/cm^2.

X. Fu et al worked with IBS composites of Sc_2O_3 and HfO_2 with SiO_2 [16]. Attempting to study the intrinsic properties of the materials they deposited they deliberately damage tested with small spot sizes to reduce the possibility of encountering defects in the materials that would skew their results. Their work showed the higher the concentration of low index material, in their case SiO_2, the higher the LIDT performance of the composite material. In the case of the slightly

doped Sc_2O_3 (< 2% SiO_2) the measured LIDT value was ~10 J/cm^2 at 12 ns and ~1.8 J/cm^2 at 500 fs. For composites of HfO_2 the values were ~7 J/cm^2 at 12 ns and ~3.1 J/cm^2 at 500 fs.

C. R. Wolfe et al. studied laser conditioning of both HfO_2 and SiO_2 thin films [107]. Their work compared the performance of E-beam deposited films with ion beam sputtered films. As moisture was driven off the surface of the optics under test they recorded an increased LIDT for the films. During their sample analysis, they identified a paramagnetic point defect in amorphous SiO_2 resulting from UV illumination. Their results suggest that after test optic conditioning the E-beam deposited films had a better LIDT performance than their IBS films.

As discussed in chapter 2, work done by Riede, W et al. compared the performance of E-beam deposited films with IBS and IAD grown material, tested in air and vacuum. Their results showed a common spectral shift towards shorter wavelengths in the transmission spectra of the E-beam coatings. This shift is most often associated with water vapor desorption. Their data showed no spectral shift in the IBS and IAD grown films. LIDT testing of these samples in vacuum showed a 5x reduction in the E-beam deposited films damage threshold when compared with their in air values. From these results they concluded that the desorption of water from the surface of the more porous E-beam films was causing increased tensile stress in these films. The IAD and IBS coatings showed no change in their performance when tested in air and vacuum [60].

Becker S., et al. studied hydrocarbon contamination of IBS grown films. They found IBS films were less susceptible to this type of contamination given the more dense, fully closed surface common to IBS films [33].

D. Nguyen et al. [34] studied IBS grown HfO_2 and SiO_2 for their LIDT performance in air, in a synthetic gaseous environment and in vacuum. They concluded that both water and

oxygen partial pressures play a significant role in mitigating surface susceptibility to laser damage.

Our work at Colorado State University focuses on the growth conditions used to produce high damage threshold material at 1 micron using the Ion Beam Sputtering (IBS) technique. This work was used to determine growth conditions for producing optimal material for in air damage performance. Methods to improve in vacuum performance were also studied. We have used a Vecco Spector dual ion beam sputtering system, shown in figure 17, to grow all the films for the work discussed in this thesis.

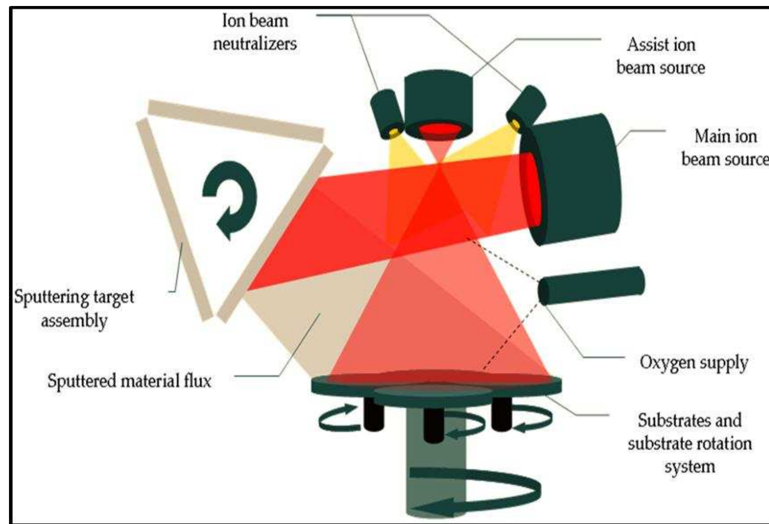

Figure 17: Vecco Spector dual ion beam sputtering system diagram

<u>The Ion Sputtering Process</u>

It is important to have an understanding of the operating basics of an IBS system for the purposes of the discussion in this section. As with most coating methods, a relatively large evacuated chamber is required for material deposition. In all of our runs the base pressure was

set to ~ 10^{-7} torr. During the sputtering, argon is supplied to the main source and through neutralizers to start the discharge and generate the Ar^+ beam.

The Ar ions are created and accelerated in a microwave plasma source located ~1m from the target (Figure 17). Argon is flown into an inductively coupled microwave cavity where that energy is used to dissociate and ionize the noble gas. The noble gas ions can be accelerated towards the target using an accelerating potential, defined by a 3-piece grid system. The grid accelerating potential defines the Ar^+ energy.

In addition to the main ion beam our Vecco Spector is equipped with a second ion source called an assist source. The assist beam and its location are also depicted in figure 17. This ion source is identical in operation to the main ion source but is physically smaller. The purpose of this second source is to bombard the growing film. Energy transfer from the assist ions to the adatoms results in increased adatom mobility helping to find the lowest energy configuration for the deposited material. This source can also be used to clean water and hydrocarbon residue from the substrate before laying down clean material in the form of a thin film.

Most of the work that is presented in this thesis is limited to HfO_2, Sc_2O_3 and SiO_2, however, we did expand our measurements in the capping layer work to include Ta_2O_5. In the case of this fourth target material one of the two high index materials was removed and the tantalum target was installed. This three target turret is rotated, between sputtering cycles, when a new material is to be deposited. Given the extreme amount of heat deposited in these targets during the sputtering process the copper backing plates for each target are water cooled and kept at a constant temperature.

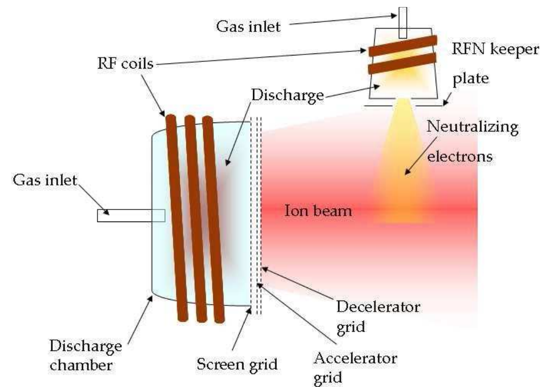

Figure 18: Sputtering ion source in the Vecco Spector [108]

To minimize the space charge effects, as well as any outside field influence, neutralizers are used. This is accomplished by spraying the ion beam with an electron beam. Our system is equipped with two neutralizer guns mounted on either side of the secondary ion source depicted in figure 18.

The process of ion beam sputtering is best described using a Sigmond-Thompson model. Together, Sigmond and Thompson describe the collision cascade expected after an ion impacts a solid surface as well as the energy distribution that can be expected of the sputtered material [75].

High energy sputtering, defined as ion energies above 10KeV, are exemplified by a fully developed collision cascade where the directionality of the momentum of the incoming ion is not preserved and the sputtered material follows a cosine distribution, about the surface normal, regardless of the ion's angle of incidence.

Lower energy collisions, those below 5KeV, allow for some preservation of information with regard to the incoming ion's velocity vector giving a somewhat specular material ablation (Fig. 19).

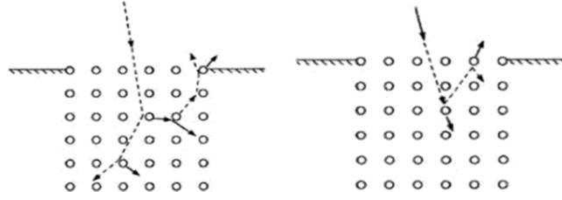

Figure 19: Collision cascade [109]

Thompson's contribution to the Sigmond-Thompson description was to develop a numerical model of the energy distribution (Fig. 20) of the ejected atoms and molecules from a sputtering event. This energy distribution is given by:

$$f(E) = \frac{E}{(E+U_0)^3} \tag{28}$$

which peaks at $\frac{U_0}{2}$. Uo is the surface binding energy of the target material.

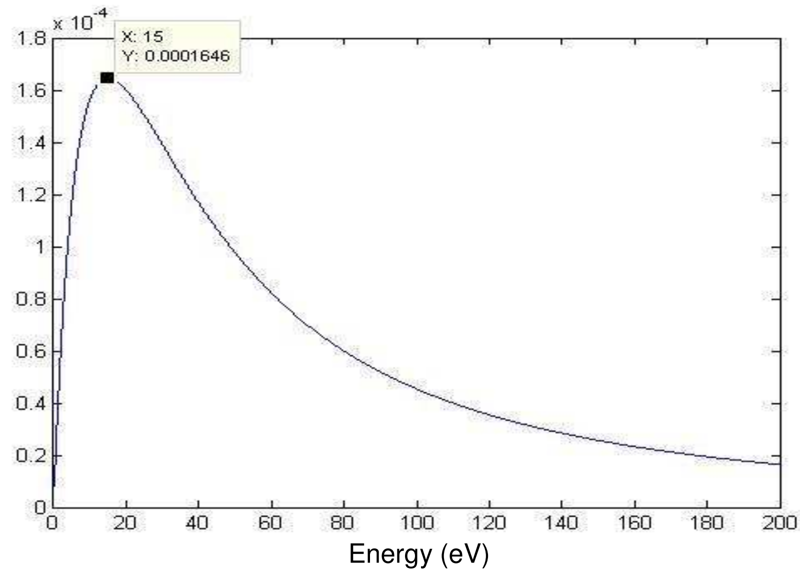

Figure 20: Thompson's energy distribution of sputtered material

Using SRIM to model the sputtering process we can visualize what is happening at the surface of the target for different incident ion energies and masses [76].

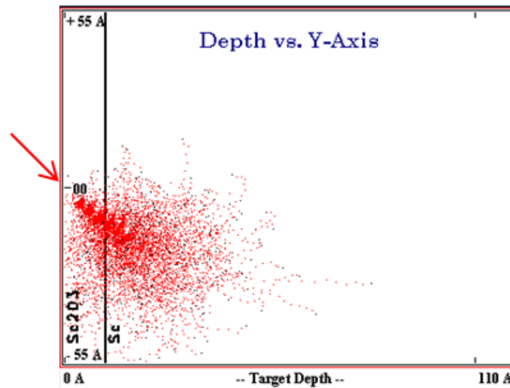

(a)

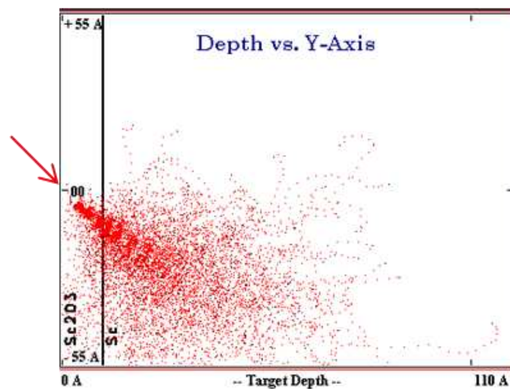

(b)

Figure 21 (a) and (b): 600 eV and 1.2 KeV Ar+ impacting and penetrating into an oxidized (10 angstrom) scandium target at 45 degrees from the surface normal.

Figures 21 (a) and (b) show Ar+ of two different energies incident on a Sc metal target with a thin oxidized skin on the surface. Higher energy ions penetrate more deeply into the target material. As the sputtering energy is increased the bulk of that energy is deposited deeper in the target mostly in the form of heat, as shown in figure 22, but some of the energy is transferred to the sputtered material.

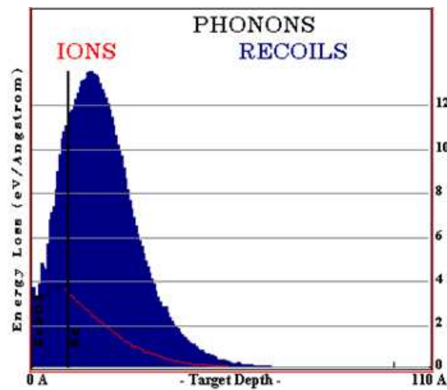

Figure 22: Energy lost to phonon creation in the target from the incoming ions (red curve) and recoiling target atoms (blue curve). 600 eV Ar+ incident on the target at 45 degrees from the surface normal.

As will be discussed shortly, the surface of the target, from where all the sputtered material originates, is an oxide. The sputtering process is a transfer of momentum from the incoming ions to the clusters, molecules and individual atoms in the target. How efficiently the incoming ions energy is transferred to the target atoms' useful kinetic energy is determined by the angle of incidence, the mass of the target atom, the mass of the ion and the chemical and physical environment the atom is in. In practice, when a target is composed of a compound like Sc_2O_3, this results in nonuniform sputtering yields for the different constituent atoms. This condition is called preferential sputtering.

Figure 23 shows the depth into the target's surface where the atoms are being disturbed by incoming ions through the cascade process. Because of how the simulation was set up, the target is only oxidized to a thickness of ~10 angstroms. This is why we see oxygen only in the first few nanometers of the target. Intermixing of the target surface with the bulk scandium is seen in the fact that oxygen exists deeper in the target than was originally defined in the

simulation. This intermixing makes it difficult to know the true state of the target during film growth.

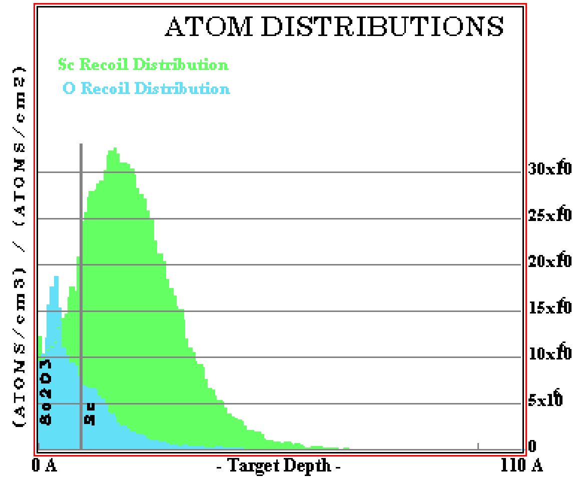

Figure 23: Oxygen and scandium dislocated in the target for 600 eV Ar+ impacting at 45 degrees from the surface

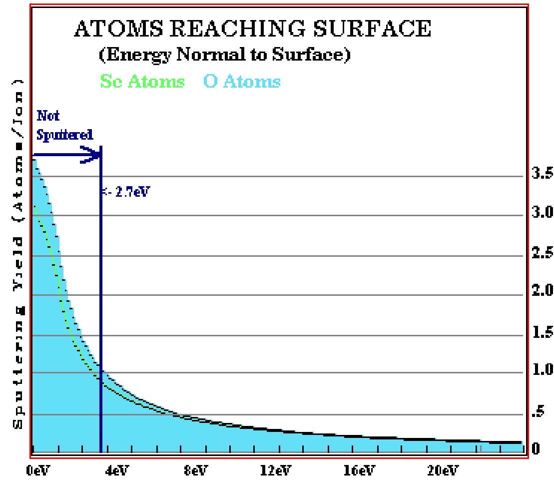

Figure 24: Sputtered atoms of oxygen and scandium for 600 eV Ar+ impacting at 45 degrees from the surface normal.

For an ion energy of 600eV, SRIM predicts a sputtering yield of 0.73 for scandium and 1.44 for oxygen with an atomic energy of 20.91 eV and 9.77 eV respectively. When the ion energy is increased to 1.2KeV the sputtering yield increases to 1.25 for scandium and 2.11 for oxygen, where scandium has 27.48 eV and oxygen 11.99 eV per atom. Figure 24 shows the relative amounts of each atom that are sputtered and the energy threshold below which this material is not released from the target. In the example simulations just shown it is clear that we do not drive off stoichiometric values for oxygen and scandium even from an oxidized surface.

Reactive Sputtering

All of the high index materials that we studied in this work were grown from solid metal targets. While metallic thin films are sometimes used in high energy mirrors they are much more lossy, in terms of absorption, than dielectric interference films. Additionally, metallic films cannot be used on transmission optics. For this reason we need to reactively sputter metallic targets to form high band gap oxides. Oxide creation takes place at the target surface and at the substrate surface. Three body reactions seldom take place in free space. Earlier work on the growth of an oxidized surface during sputtering confirms this to be true [65].

Figure 25 shows the oxide coverage of a metal target plotted against oxygen partial pressure. The plot also shows the metallic sputtering rate, again as a function of oxygen partial pressure. From this plot we can see that for oxygen partial pressures much above $4e^{-5}$ torr the vast majority of the material sputtered from the target surface is an oxide. A more complete description of the oxide formation is discussed in Erik Krous' thesis [108]. The oxygen in this reaction is fed into the vacuum chamber at a single location and is directed at the target.

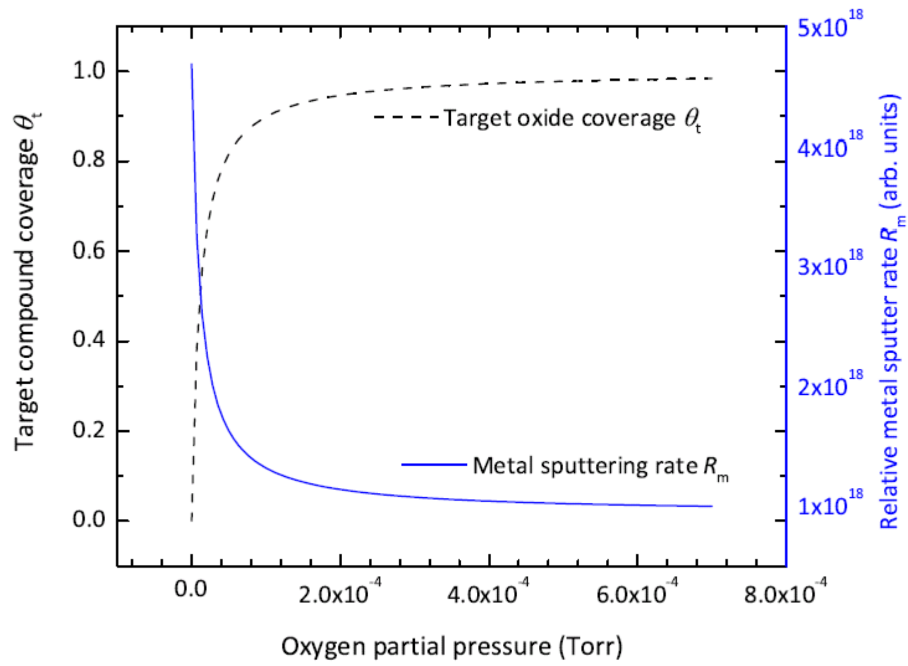

Figure 25: Oxide coverage of a metal target plotted against oxygen partial pressure [110].

CHAPTER V. THIN FILM CHARACTERIZATION

A suite of optical and material measurement techniques were available to characterize the metal oxides grown using our ion beam sputtering technique for the work described in this thesis. This chapter describes the basis of the characterization tools used to evaluate the optical and mechanical performance of our films.

Spectrophotometer

Generally, the first measurements made on a film once it is removed from the deposition chamber are transmission measurements. These are made using a Hitachi U-2010 UV/Vis Spectrophotometer. The data from this measurement give us information on the bandwidth of light that can transmit through a material we've grown or the amount of light reflected off a coating structure as a function of wavelength. This technique gives us as close as we have to a direct measurement of the effective optical band gap of the material. Figure 26 shows a typical transmission spectrum for a representative single layer thin film that we grew.

For a defect free high bandgap material the absorption is negligible for photon energies below the bandgap. This is not the case for practical amorphous metal oxides. Transmission data near the band edge can be used to generate a Tauc's plot from which the effective band gap of the material can be extracted.

Figure 27 shows two direct transition Tauc's plots that were generated from transmission data on representative Sc_2O_3 single layers. This plot shows the subtle influence of post deposition annealing on the effective band gap of the material.

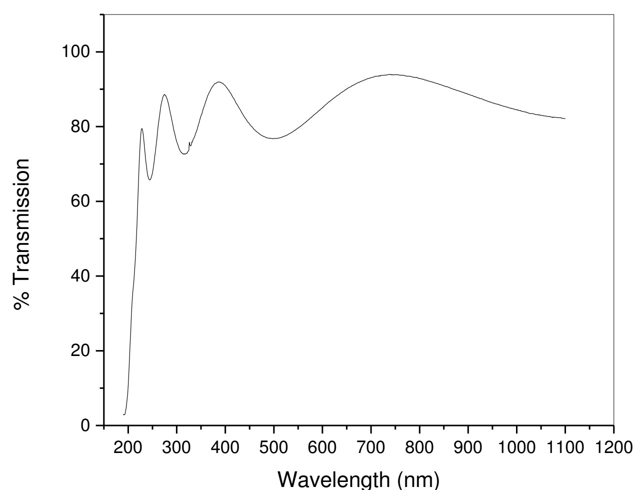

Figure 26: Typical spectrophotometer trace.

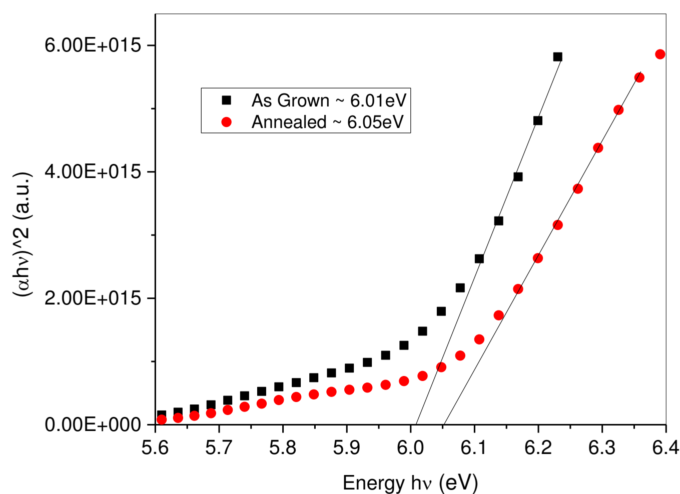

Figure 27: Example Tauc's plot of Sc_2O_3 single layers one as grown and one annealed.

A linear extrapolation to the horizontal axis, photon energy, shows the effective band gap using the following expression:

$$\alpha h\nu = B(h\nu - E_g)^{0.5} \tag{29}$$

If a single layer is being characterized the spectrophotometer is capable of detailing material specific information, however, if the film being measured is a multi-layer structure some of this information may not be easily resolved.

Spectroscopic Ellipsometry

An ellipsometer is a tool used to measure the layer thickness and the complex refractive index as a function of wavelength. The basic operation of this instrument is depicted in figure 28 where linearly polarized light illuminates the sample at different angles. The reflected light is collected after passing through the analyzer which is simply a second polarizer.

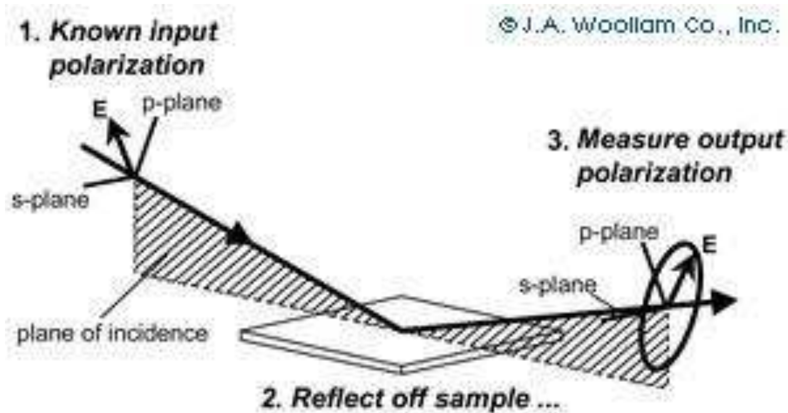

Figure 28: Diagram of Woollam ellipsometer operation. [111]

The changes in reflection vs wavelength for two polarizations are measured. These changes are represented by Ψ, an amplitude ratio, and a phase difference Δ, whereby the ratio of the polarizations is given by:

$$\rho = \tan(\Psi)e^{i\Delta} \quad (30)$$

With this expression and the angles of incidence “pseudo” optical constants can be found.

$$\langle\tilde{\varepsilon}\rangle = sin^2(\phi)\left[1 + tan^2(\phi)\left(\frac{1-\rho}{1+\rho}\right)^2\right] \quad (31)$$

Regression analysis is used to fit all measured data including any other known values, for example, film thickness. Values for n and k are found using the Cauchy-Sellmeier relationship where Cauchy gives a value for the wavelength dependent optical index and Sellmeier forces Kramers-Kronig consistency. From this relationship the extinction coefficient can be determined. The more data that are available to the regression analysis the more accurate the modeling is. A good overview of the operating principles of an ellipsometer is given on line by the J. A. Woollam Company [112].

Film Stress

IBS thin films are characterized by high compressive stress due to the high packing densities that result from this energetic process. Large amounts of internal stress are not desirable in thin films for a few reasons. Excessive stress can lead to film delamination over time and high stress in these films can also contribute to a lower LIDT performance in the form of stress related defect states [59]. To measure the relative and absolute stress resulting from a particular

deposition process we used a Twyman Green interferometer to profile the surface curvature of a thin test optic both before and after the film was deposited.

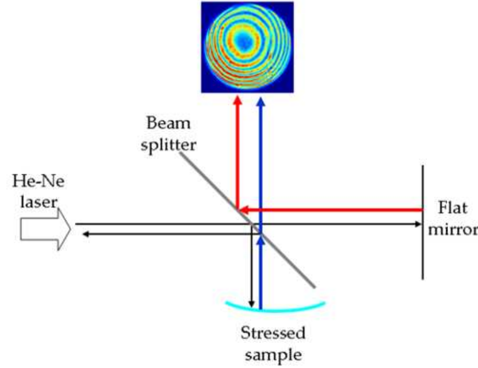

Figure 29: Twyman Green interferometer

Knowing the material properties of the thin substrate and the measured curvature observed after the film was applied we can use Stony's equation to quantify the amount of stress the film is under.

$$\sigma_f = \frac{E_s d_s^2}{6 d_f (1-\nu_s)} \left(\frac{1}{R} - \frac{1}{R_0} \right) \tag{32}$$

R is the curvature of the substrate and thin film system, R_0 is the radius of curvature of just the substrate, d_f and d_s are the film and substrate thickness respectively, E_s is Young's modulus of the substrate and $\nu_s$accounts for biaxial stress in the film. This expression is only valid when the thickness of the substrate is thin enough to allow our deposited film to influence the surface curvature of the test optic [113]. The stress of the films studied in this work were characterized using this method and found to vary from 0.55 GPa to 1.3 GPa over the range of deposition conditions we used.

Photo-thermal Common Path Interferometer (PCI)

One of the most heavily used analytical tools in this work was the Photo-thermal Common path Interferometer. This instrument uses a pump/probe configuration to make high sensitivity absorption measurements at a given wavelength. The probe beam is a low power, high stability laser, generally a HeNe, that needs to emit at a wavelength that is not strongly absorbed by either the thin film or the substrate on which the film is grown. No measureable heating is done with the probe beam, given its relatively low power density on the test optic, however, if the film or substrate absorbs the probe beam there will be no information transmitted outside the system regarding the pump beams influence on the test optic. The pump beam is chosen to be at the wavelength of interest in terms of the amount of this color of light that is absorbed. The pump beam is generally much higher power than the probe beam, in addition to being focused at the surface of the test optic. The pump beam is modulated so as to be able to distinguish its influence on the test optic from background noise in the sensing photo diode. The pump and probe beams are aligned to be coincident at one point in space where the pump beam is at its waist. When the pump beam is incident on the test optic surface it locally heats the film which then heats the substrate. The much larger probe beam (>10x) is then modified by any index change in the test optic that produces a phase modulation of $e^{-i\Delta\phi}$. This phase modulation is small and can be approximated as:

$$e^{-i\Delta\phi} \approx 1 - i\Delta\phi \tag{33}$$

Most of the larger probe beam is unaffected by the thermal lens created by the heating pump beam except at the center of the probe beam. Here there is a dn/dT variation that results in

a positive lensing effect on the probe beam. Essentially there are now two waves, the original probe wave represented by the unity term and the much weaker wave represented by $-i\Delta\phi$. Just at the test optic's surface the two waves produce no interference pattern due to being out of phase by $-\pi/2$. The diverging portion of the probe beam interferes with the collimated portion of the same beam as the two waves propagate through the focus of the weak wave. The point of maximum intensity contrast resulting from the two probe beams interfering is located at the Rayleigh range of the weak wave and has a value of $\Delta\phi = \frac{\Delta I}{I}$ [114].

The point of highest contrast of the interference is imaged onto a photo-diode and, using a lock in amplifier, the signal is plotted as a function of the test optics z-position. A representative PCI scan is shown in figure 30. A schematic of the method and a photograph of the system are shown in figures 31 and 32.

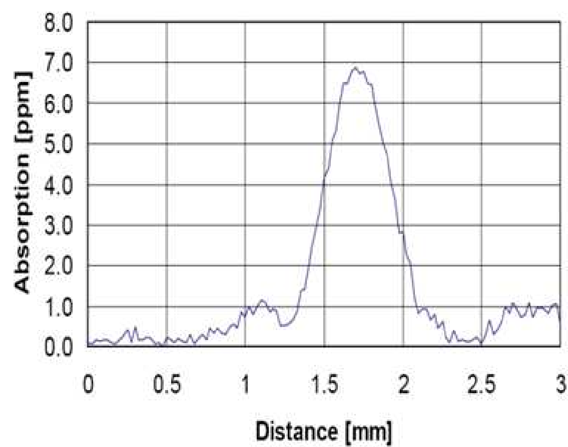

Figure 30: Typical PCI surface absorption signal

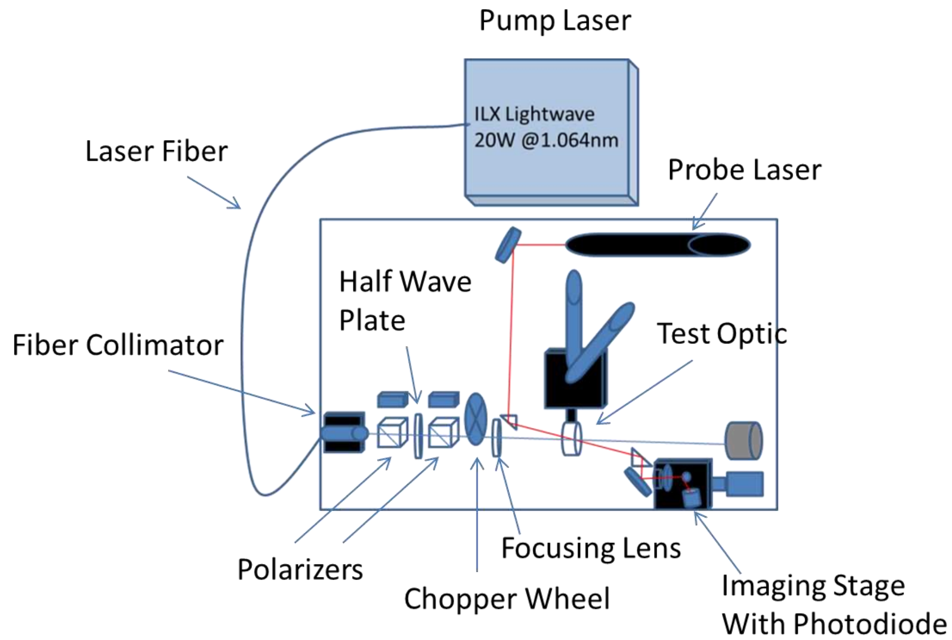

Figure 31: PCI schematic

Figure 32: Picture of PCI at Colorado State University

This technique is capable of scatter insensitive absorption measurements in the parts per billion. To correlate linear absorption and damage threshold in this work we carried out PCI measurements on all our samples that were grown.

Nomarski Imaging

Given that many different groups are researching similar topics at many different locations all with unique sources and experimental setups, a standard was developed to help the results from these different research groups understandably relay their findings to each other and to a broader audience. The most broadly accepted standard for laser damage testing is ISO21254-1:2011 defined and refined in the context of the Boulder damage conferences over the past several decades. One of the critical pieces of damage analysis is the use of a Normarski phase contrast microscope. This tool makes use of Fourier optics to interrogate the subtle phase changes in areas of otherwise low contrast. A traditional bright field microscope is not capable of resolving these types of material modifications. If there was a contradiction between in situ damage identification and postmortem Normarski analysis we always deferred to the Normarski results in our research.

Total Integrated Scatter (TIS)

Losses in an optical system are not limited to absorption and specular reflections alone. Anywhere there is an interface, or change, in the optical index of a material some transmission, reflection, and perhaps absorption will take place. The interplay of these three processes defines the function of the interface. In the case of an optically smooth surface, transmission and reflections are said to be specular. If there is, however, some finite roughness to the surface scattering will also occur. While scattering is not necessarily a contributor to laser induced damage except in extreme cases, it is a contributor to inefficiencies in the system. While practical systems are always a balance between gains and losses it is generally not a good idea to improve one aspect of a component's performance at the egregious expense of another. For this

reason we performed measurements of the total integrated scatter, both forward and back scattered, of our thin films as a function of the parameter changes in our LIDT investigations.

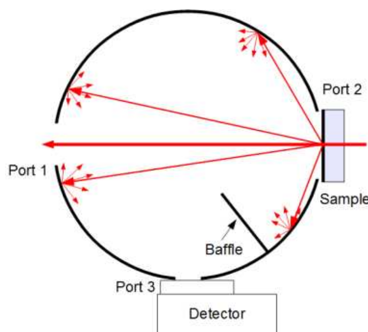

Figure 33: Total integrated scattering sphere, sample and diode [115].

Figure 33 is a depiction of an integrating sphere used to quantify the amount of scattered light from the films we grew. This measurement technique was used to ensure we did not introduce significant scattering losses for different deposition process conditions.

X-ray Photo-electron Spectroscopy (XPS)

One of the principle materials analysis tools we made regular use of in our research was the X-ray Photo-electron Spectrometer. XPS measurements are capable of identifying the elemental composition of a sample as well as giving the user information on the chemical bonding environments of the atoms. XPS operates on the principle that an element can be uniquely identified by the energy spectrum of emitted electrons ejected from an inner orbital, or core level states. Each electron emitted by an atom will have a velocity unique to the element it came from. This energy fingerprint is described by the following expression:

$$K.E._e = h\nu - B.E. - \phi_{spectrometer} \quad (34)$$

where the kinetic energy of the emitted electron is equal to the incident x-ray energy, minus the core level binding energy of the atom, minus the work function of the spectrometer. The energy of the incident x-rays is known precisely. Generally the Kα emission from copper, aluminum or magnesium targets are used to probe samples. When the x-ray energy exceeds the binding energy and work function of the target materials, electrons from the core orbitals are removed from the solid. These electrons are directed using a hemispherical analyzer to spatially separate electrons by their relative energies. Once the electrons' energy is known the core level binding energy can be found. From this value we can identify which elements are present and their relative concentrations.

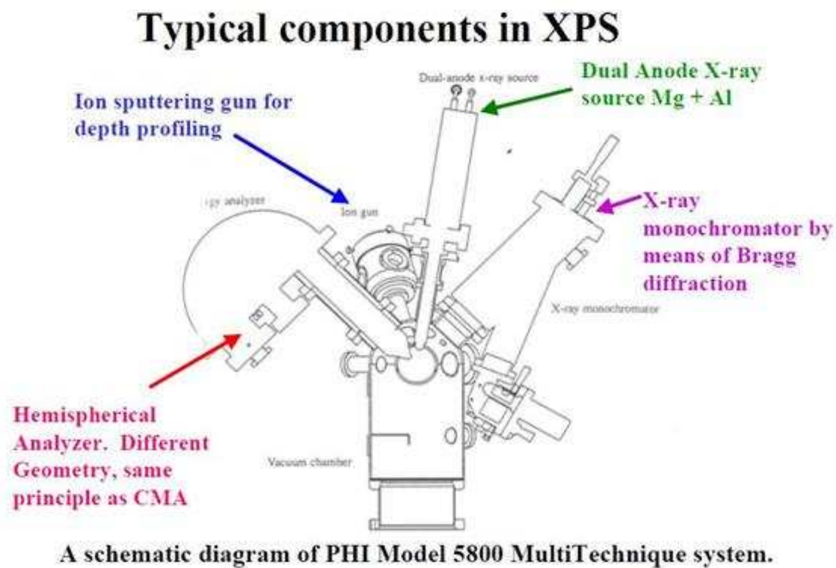

Figure 34: XPS diagram

When the material of interest is a compound rather than a pure element the influence of additional chemical bonding environments can and do influence the energy spectra of the emitted

electrons. For example, the presence of an oxide has the tendency to increase the binding energy of the system by allowing less electron screening of the nucleus.

XPS is essentially a surface specific measurement tool. Because of the surface specific nature of this measurement technique it is often times necessary to sputter clean, or remove the outer few nanometers of the surface to ensure that you are not measuring surface contamination. In the case of HfO_2 and Ta_2O_5 thin films this sputter cleaning with Ar+ significantly altered the chemical makeup of the surface.

In figures 35 and 36 we see a 4f peak of hafnium in a high resolution scan. In figure 35 the 4f peak is associated with hafnium bound to oxygen in an HfO_2 molecule. Figure 36 is a scan over the same binding energy on an HfO_2 sample after sputter cleaning the surface with Ar+s. Here we see two binding environments for hafnium, with the lower binding energies associated with metallic hafnia. Both the metallic hafnium and the oxide appear as two peaks due to spin orbital splitting. Slight shifts in the location of the oxide peaks are likely due to surface charging during the sputtering process.

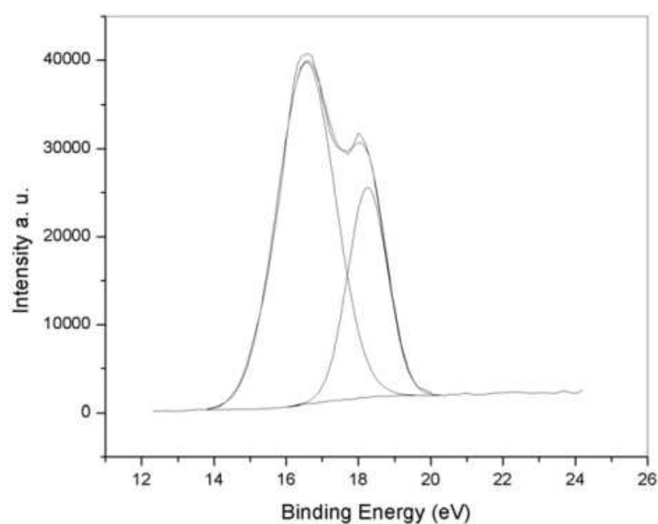

Figure 35: HfO_2 XPS 4f peak

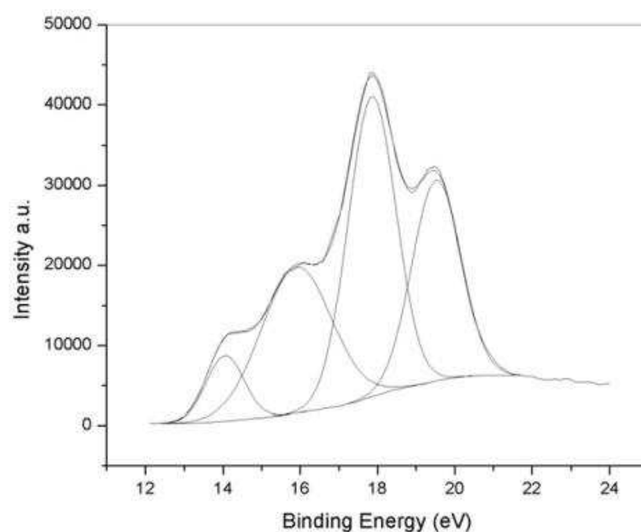

Figure 36: HfO_2 and hafnium XPS 4f peak

In the case of figure 36, the oxygen was preferentially sputtered away during cleaning. Sc_2O_3 films proved to be immune to this sputter mediated reduction, however, a fact that we exploited in most of our material studies.

Fourier Transform Infra-Red Spectroscopy (FTIR)

During the course of our analysis on several samples it became necessary for us to be able to categorically state that we had no chemical bonds between scandium and carbon or between scandium and oxygen bound in a hydroxyl group. Several of the analysis techniques we had used up to this point were leading us to believe that we had excess oxygen in our films that was not bound to a metal. Both carbon and hydrogen readily combine with oxygen and these elements are ubiquitous on nearly any surface. While XPS gave no evidence for the existence of carbon on or in our films after cleaning, hydrogen cannot be seen using XPS. To assess whether these two bonding environments existed in our films it was decided we would use another

technique to probe for these potential bonds. Fourier transform infrared spectroscopy is a common measurement tool used to probe chemical bonds. The operating principle of this technique is to make use of the relationship between the spatial information available in a broad band interferogram and the frequency information in the same image by use of a Fourier transform. For a polychromatic, broad band light source the recorded interferogram is related to the absorption spectrum by:

$$I(x) = \frac{1}{2\pi} \int_{-\infty}^{\infty} B(\nu) cos2\pi\nu x d\nu \qquad (35)$$

and conversely the absorption spectra is related to the interferogram by:

$$B(\nu) = \int_{-\infty}^{\infty} I(x) cos2\pi\nu x dx \qquad (36)$$

where B(ν) is the intensity of the source as a function of frequency and x is the displacement of a movable mirror that selects the wavelength of light. Figure 37 shows an example of the intensity measured at the detector as a function of the mirror position.

Figure 38 shows representative absorption spectra for Sc_2O_3 samples grown in our studies. As can be seen in the figure there are three features in the absorption spectra. The first is the gamma peak which we were not able to identify but we can confirm it is not associated with water or hydrocarbon absorption. The second peak is near 633 cm^{-1} which we have identified as a Sc – O bond vibration and the third much weaker peak near 1110 cm-1 is a silicon oxygen bond. In these absorption spectra we saw no evidence for hydrogen-oxygen or hydrogen-carbon bonding.

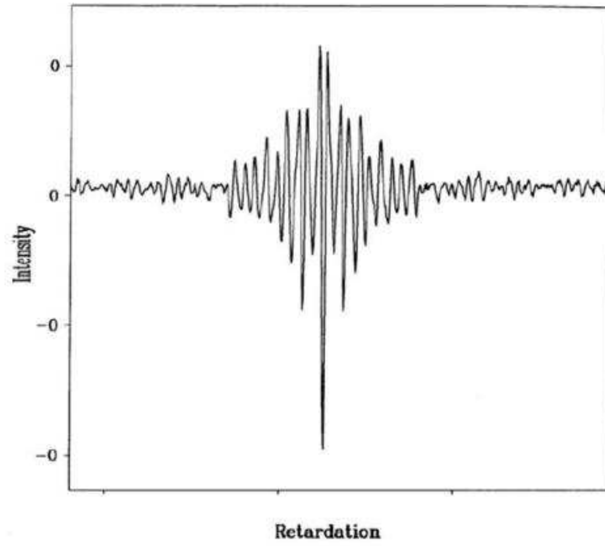

Figure 37: FTIR spectra [116]

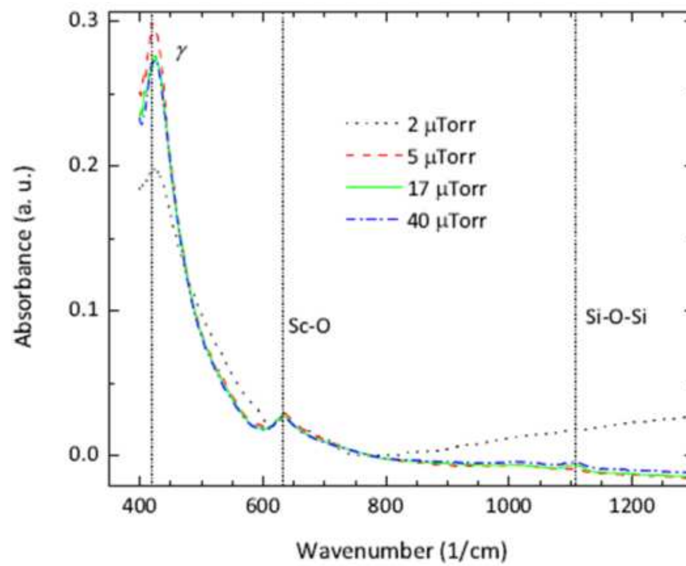

Figure 38: Example FTIR spectra of an Sc_2O_3 films grown on Fused Silica

Atomic Force Microscopy (AFM)

We used atomic force microscopy for surface profiling of our films to measure roughness and to determine if clustering or nodular formation was occurring. A more in depth explanation of the work our group did on this topic is given in Jonathan Tollerud's thesis [115].

The principle of operation for an atomic force microscope is that a very small needle like probe is suspended very near to the surface that is to be measured. This probe is attached to an oscillating lever arm whose motion is monitored by a laser bouncing off this arm. When the probe tip is very near the surface of a sample the ionic repulsion of the atoms on the probe tip and on the sample will modify the oscillating frequency. This change is used to measure the distance between the probe tip and the sample. In this way a topographical map of the sample surface can be built up revealing nanometer sized bumps or pits and used to quantify the overall roughness of the surface.

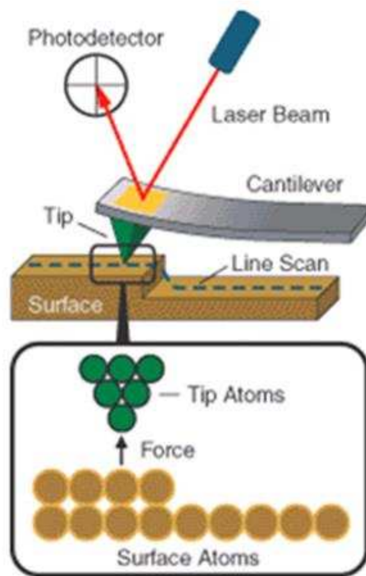

Figure 39: AFM explanatory diagram [117]

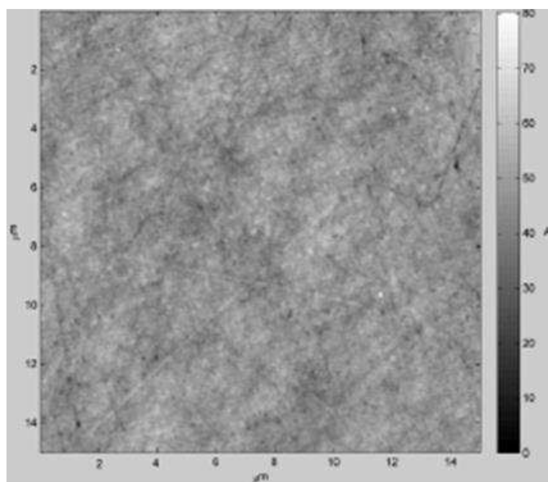

Figure 40: Representative AFM scan of a 100 nm thick HfO_2 film

A representative AFM scan on a 100 nm thick HfO_2 film is shown in the above figure. Typical roughness values for the 100 nm thick Sc_2O_3 films were 0.6 nm while the 100 nm thick HfO_2 films measured 0.7 nm.

Scanning Electron Microscope/Energy Dispersive X-ray (SEM/EDX)

While AFM can produce data of higher resolution it is not always useful for identifying surface features particularly over a large area. For this work we generally made use of a Scanning Electron Microscope. If elemental analysis was also useful the same SEM was used in an Energy Dispersive X-ray measurement. The principle of operation for an SEM is the use of electrons in the place of photons to image the target's surface. The benefit of this process over optical microscopy is the much higher resolution offered by the DeBroglie wavelength of an electron over lower energy photons. Representative SEM images of damage sites from different films grown in our studies are shown in figures 41 - 42.

In single shot damage testing these images can yield a good deal of information on the type and degree of early onset damage. This information is often times key to understanding the

nanometer scale processes that occur during our extremely short time scale damage events. When testing multiple shot damage on a single test site this kind of information is often obscured by the fact that subsequent laser pulses often exaggerate the events of the earlier laser pulses.

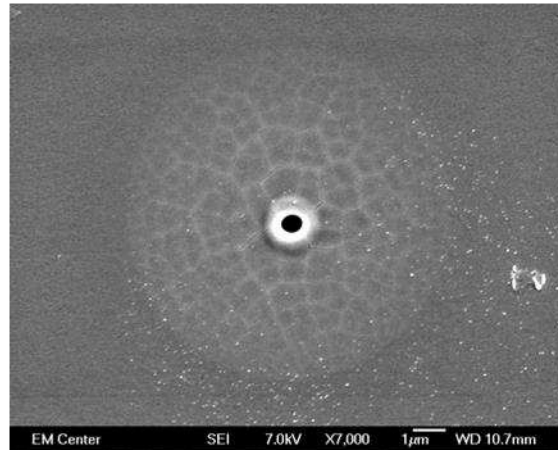

Figure 41: SEM image of a damage site on a Sc_2O_3 single layer film

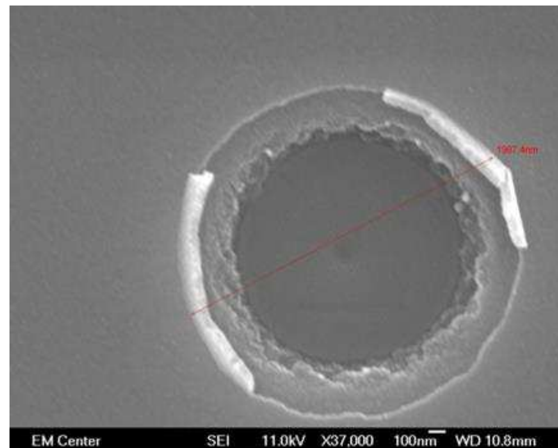

Figure 42: SEM image of a damage site on a HfO_2 single layer film

X-Ray Diffraction (XRD)

X-Ray Diffraction is the measurement technique we used to determine the level of crystallinity and crystallite size in our films. Our aim was to produce films that were completely

amorphous which would result in a feature free XRD scan. XRD's operating principle is basically the same as for the optical thin films we are studying in our work.

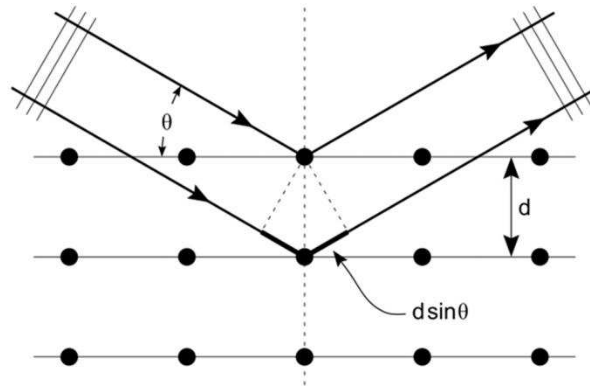

Figure 43: XRD Bragg diffraction [118]

Bragg diffraction governs the response of a crystal to the incident x-rays. Specifically the expression:

$$2dsin\theta = n\lambda \quad (37)$$

which describes the relationship between the lattice spacing of atoms and the wavelength of ight that will result in constructive interference between the x-rays reflecting off atoms. In a crystalline material the orientation of the lattice relative to the incident x-rays will alter the diffraction pattern. For an amorphous material the orientation should have no influence. By keeping track of the position of the diffraction peaks as well as any changes in the width of these peaks we are able to deduce not only the crystallite size but also the influence of local stresses in the material.

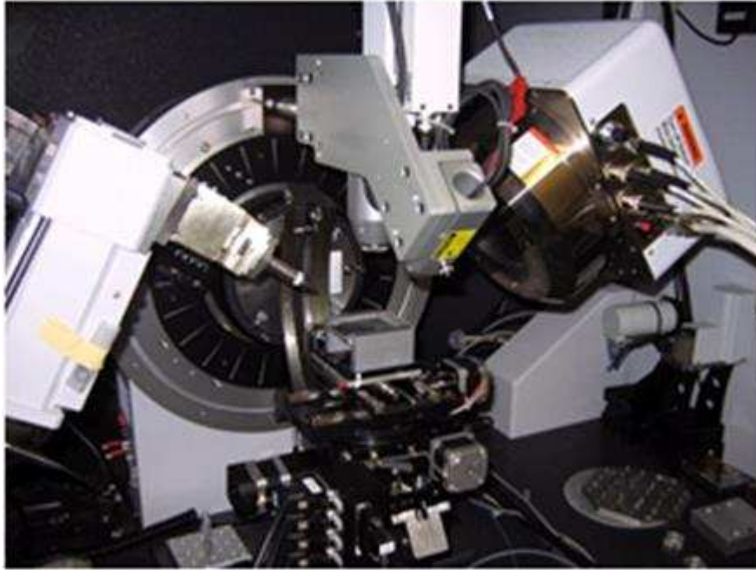

Figure 44: XRD system

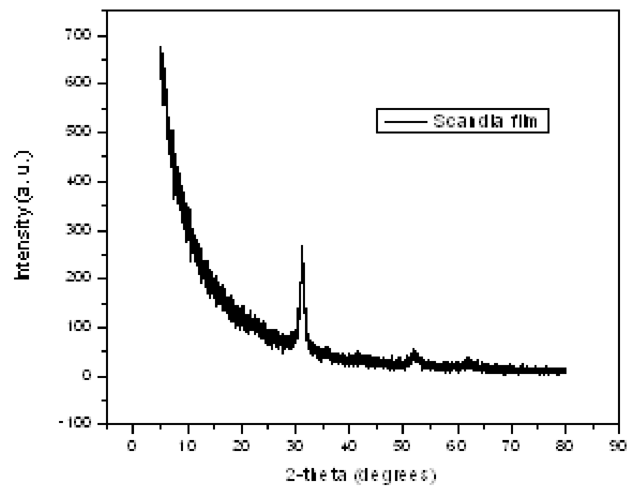

Figure 45: Example XRD scan of an Sc_2O_3 film

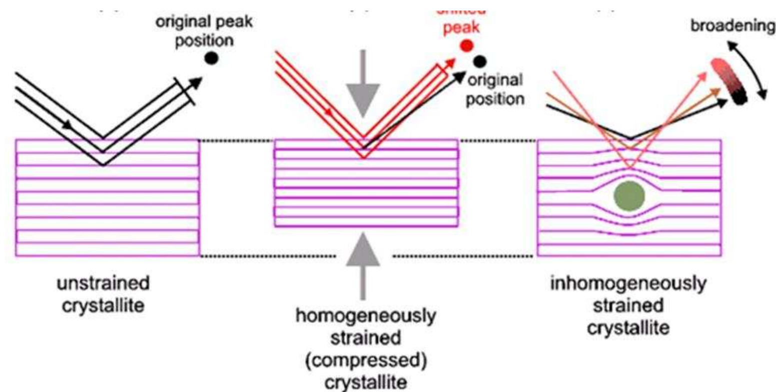

Figure 46: Mechanisms to strain broaden an XRD peak [119]

Peak shifts are attributable to changes in the lattice spacing while peak broadening can be due to either lattice parameter changes or to strain broadening (Fig. 46). Figure 45 is a representative XRD spectra we recorded on a Sc_2O_3 thin film.

Electron Para-magnetic Resonance (EPR)

Electron Para-magnetic Resonance spectroscopy is a measurement technique that probes a sample for unpaired electrons, as might be found when chemical bonds are broken or were never completely formed. We chose to use this measurement technique given the likelihood that nonstoichiometric ratios of oxygen and metal are likely to be a significant contributor to laser damage onset in our materials as well as being paramagnetic sensitive defects. Previous work on ZrO_2 showed an EPR signal that was associated with unbound oxygen in the film having a g tensor of $[gxx, gyy, gzz] = [2.0045, 2.0105, 2.0304]$ [120].

The principle of operation for this instrument is based on the Zeeman Effect that shows the presence of an applied magnetic field splits a single orbital energy into two levels for the magnetic moment of the electron (Fig 47). These two states are defined by the projection of the

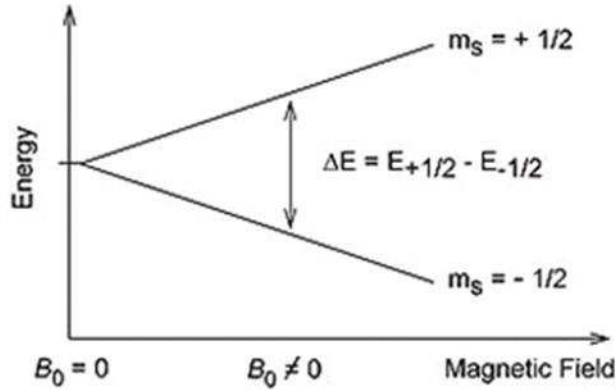

Figure 47: Zeeman split of one energy level [121]

electrons spin (m_s) onto the applied magnetic field. The state that is parallel to the magnetic field, $m_s = -\frac{1}{2}$, is the lower energy state and the antiparallel state, $m_s = \frac{1}{2}$, is the higher energy orientation. For an electron, the magnetic moment is given by:

$$\mu = m_s g_e \mu_B \tag{38}$$

where μ_B is the Bohr magneton and g_e is the g-factor of a free electron which has a value of ≈ 2.0023192778. The energy of these states is then given by:

$$E_{1/2} = 1/2\, g_e \mu_B B_0 \tag{39}$$

and

$$E_{-1/2} = -1/2\, g_e \mu_B B_0 \tag{40}$$

The energy difference between these two states is:

$$\Delta E = g_e \mu_B B_0 \tag{41}$$

These expressions describe an electron in free space. For most practical uses of these expressions consideration has to be given to the influence of the nearby molecules. The total angular momentum must now include an orbital angular momentum. While this contribution is generally small for electrons in the ground state, higher energy states can influence the ground state electrons by spin orbital coupling. All these contributions are generally accounted for by changing the $g_e$to simply g. Now if we equate the difference in energy between these two Zeeman split states and the energy of an external photon we have an expression of the form:

$$g \mu_B B_0 \; = h\nu \tag{42}$$

or solving for the g value

$$g = \frac{h\nu}{\mu_B B_0} \tag{43}$$

where ν is the frequency of the photon, B_0 is the external magnetic field, h is Planks constant, μ_B is the Bohr magnaton and g is the Landé g-factor or simply the g-factor. Because it is generally more difficult to sweep the output frequency of a microwave source than it is to sweep the

magnetic field strength of an electromagnet, the B_0 term is generally the one that is varied. Figure 48 shows a schematic of a typical EPR measurement apparatus. Figure 49 shows a representative EPR absorption derivative on two samples grown with different oxygen partial pressures. The area under the absorption peaks can be used to determine relative defect densities for different samples measured. The fitting of the trace with the Easy Spin Matlab ® code allows one to obtain the g-factor. Theoretical analysis has calculated the g-factor for different point defects for the two materials we are most concerned with. The values for this defect in Sc_2O_3 are: [g_{xx}=2.017, g_{yy}=2.022, g_{zz}=2.055]. The values for HfO_2 are: [g_{xx}=2.018, g_{yy}=2.019, g_{zz}=2.057]. The values for Ta_2O_5 are not available.

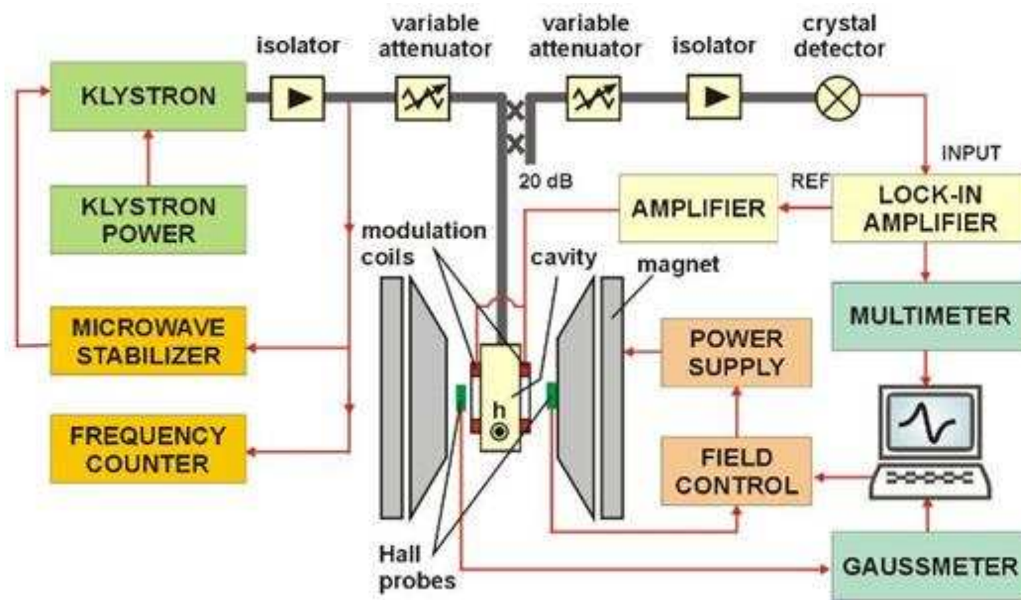

Figure 48: Diagram of an EPR cavity, magnet and support equipment [122]

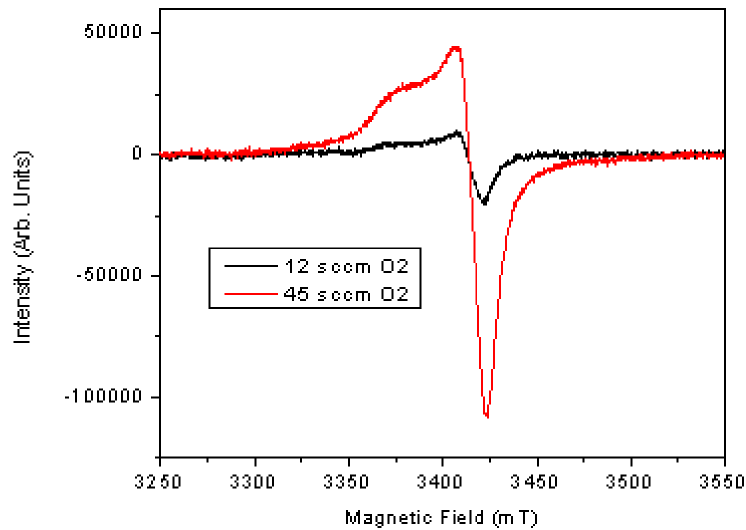

Figure 49: Example EPR spectra of two Sc_2O_3 films grown using different oxygen partial pressures.

Laser Damage Testing of Thin Films

A good deal of work was devoted to constructing laser damage test apparatus for in air and vacuum testing. These apparatus are described in the following sections.

In-Air LIDT Testing

Once the films are fully characterized in terms of their optical and mechanical properties we are ready to test these thin films for their ability to resist damaging in a high fluence environment. The LIDT testing that was done used one of two different methods depending on where we were in the development process and what exactly we were trying to study. For the majority of the early work studying process parameter influence on laser damage performance of our materials the LIDT testing was done using what is called a 1-on-1 test protocol. In this test every laser shot illuminates a fresh location on the test optic. After a single shot a new target location is selected and another single shot is taken. Ten sites are evaluated at preselected

fluences. This was repeated as many times as necessary until all ten test sites, illuminated with an identical fluence, were damaged, or until we ran out of fresh test sites on the test optic's surface.

The second test method that was employed was only used during the controlled environment testing we did. This included the in vacuum testing. Owing to the fact that single shot testing cannot display the multipulse LIDT reduction effects we wished to study, a new R-on-1 protocal was used, with 100 shots per test site. This method was identical to the 1-on-1 testing just described with the exception of the fact that one hundred equal energy laser pulses were shown on each test site before a new test site was targeted. To preserve the statistics from the earlier testing we still chose ten unique sites to illuminate with an identical fluence. The fluence was increased until all ten test sites damaged at the same fluence value or until we ran out of real estate on the test optic.

Laser damage testing requires a significant amount of precision in pre-test characterization of the damaging laser, positional sensitivity of the test optic and the repeatability of both. Ideally, for our purposes, we would like a diffraction limited laser spot to be used in our testing. Because this is a practical impossibility we then need to be confident that our transverse beam profiles are consistent from shot to shot. This is accomplished, for our single shot testing, by capturing a beam profile of each laser pulse. When testing 100-on-1 measurements we capture a single representative beam profile for each 100 pulse train. The pulsewidth of the damage laser was measured using a second harmonic autocorrelation of the pulse [83]. The energy delivered to the target is calibrated with a power meter as a half wave plate is rotated through 90 degrees in front of a polarizer. The positional accuracy of the beam waist is determined to better than 50 microns using focusing lenses having Rayleigh lengths measured in millimeters. Once we have a calibration curve for the power versus wave plate position and

corresponding beam profiles we can then make use of the captured beam profiles during testing to precisely determine the peak fluence on axis at every test site.

To give us some statistical information on the damage performance of our different materials we chose to illuminate ten unique test sites at a given fluence. Generally, we began with an educated guess as to where we might expect to see damage for a given film type. This guess was based off previous testing we had done on these materials. After dialing in the starting fluence, generally 2-3x lower than the expected damage threshold, a gentle flow of dry nitrogen was turned on that would force surface debris down and away from fresh test sites. Control software written to help automate the testing would allow a predetermined number of pulses through an external shutter and onto the test optic's surface. A 16 bit iKon Andor camera was used to capture a representative beam profile from each burst of pulses. In situ damage identification is made using a Mitex or Lumenera camera behind a 10x telescope in a dark field scattering configuration. An external 5mW HeNe is focused coincidently with the damaging beam on the test optic's surface. The focal spot of the HeNe is nominally set to match or be slightly larger than the IR beam footprint. Figures 50 and 51 show a diagram and a picture of the in air test setup.

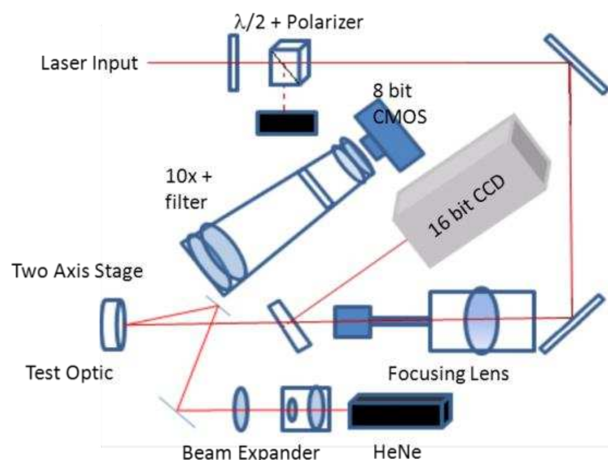

Figure 50: Diagram of in air LIDT test setup

Figure 51: Picture of in air LIDT test setup

In-Vacuum LIDT Testing

As was mentioned earlier, our interest in the damage performance of the films we have grown extends beyond the traditional in air testing we have discussed so far. The growing interest in using metal oxide films in vacuum necessitates the thin film industry fully understanding the degradation mechanisms these materials see when in vacuum. I built a vacuum LIDT testing system shown in figure 52 with its components shown in figure 53.

Performing damage testing in vacuum can be done relatively simply if little attention is given to the cleanliness of the testing environment and if the base pressures of interest are not too low. In our case we were specifically interested in being able to present a pristine optical surface for damage testing. This requirement, while easy to say, represents a massive increase in the level of complexity and effort. As discussed earlier, the four most likely contributors to the reduced LIDT performance of metal oxides when tested in vacuum were water impregnation

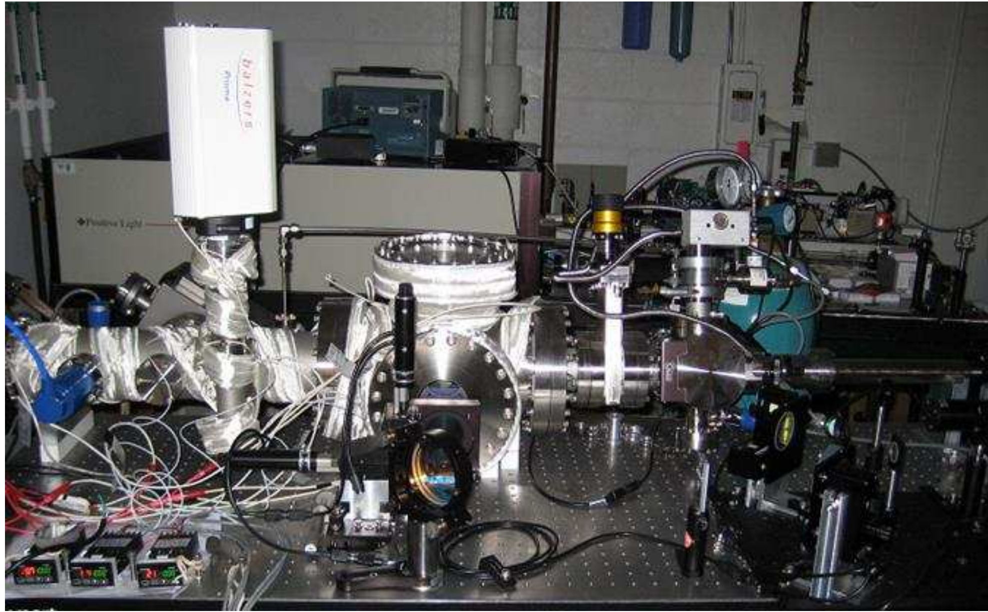

Figure 52: UHV damage test apparatus

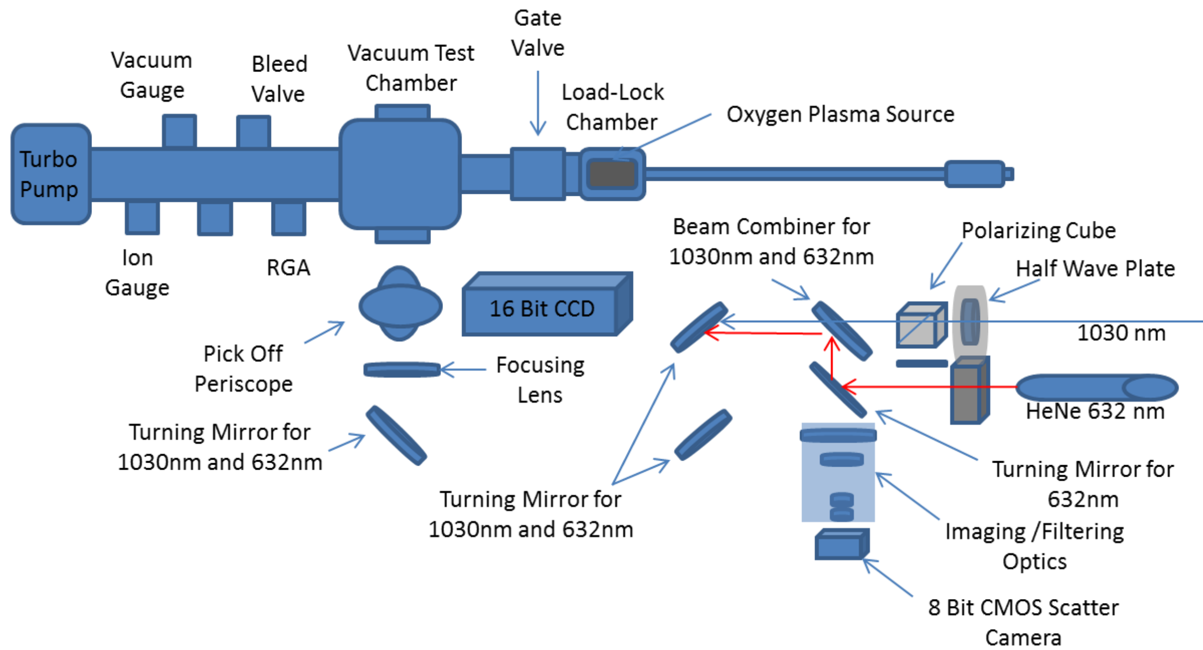

Figure 53: Schematic of UHV damage apparatus

and subsequent explosion beneath the surface (during testing), reduced thermal conductivity from water desorption off the surface, hydrocarbon contamination or carbon cracking, and

surface defect creation, likely in the form of oxygen dissociation. The extremely dense nature of IBS coatings has been shown to be immune to the first of these possibilities by presenting a fully closed surface to the outside environment [18]. The fact that water desorption from the surface can reduce the thermal conductivity of the area surrounding the test site is modeled later in one of the technical chapters with the results of that work discussed there. To address the possibility of carbon contamination is something our hardware choices were designed to address and the results of these efforts are shown in the data. We decided early on that operating in the Ultra High Vacuum (UHV) was desirable to ensure as clean a surface as possible. Removal and introduction of a test optic into a vessel, while preserving a clean environment, can be very time consuming. We fitted our UHV chamber with a load lock to facilitate these sample changes and allow us to return to testing within eight hours of introducing a new sample at room temperature. To remove the hydrocarbons from the sample and sample holder before introduction into the UHV chamber the load lock was fitted with an XEI oxygen plasma cleaner [98].

Figure 54: XEI plasma cleaner used to remove hydrocarbon contamination from test optic surfaces before introduction into the testing vacuum chamber [123].

This plasma cleaner was used to clean the front and back surfaces of each sample before being inserted in the test chamber. An example of the relative cleanliness of our vacuum chamber after the introduction of an XEI cleaned test optic is given in figure 55.

Once the test optic was loaded into the UHV chamber we pumped on the sample for eight hours, nominally, always reaching a base pressure of < $5e^{-9}$ torr before any testing was done.

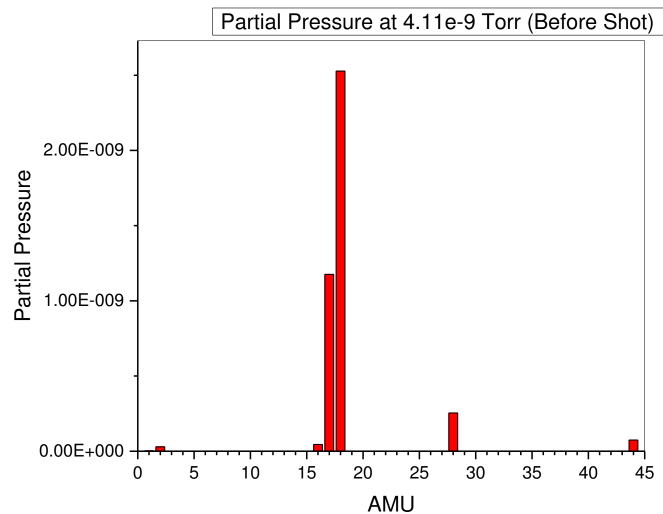

Figure 55: Partial pressure measurement made on the UHV chamber with a sample inside after 8 hours of pumping.

The vacuum vessel itself was physically large and several hundred pounds in weight. This required that we direct our damaging laser across the test optic's surface rather than simply scan the test optic around the focus of a stationary beam. To always present a beam normal to the test optic's surface we used two computer controlled Zaber mirror mounts in conjunction with a computer controlled stage that held the focusing lens. This arrangement was able to accurately and repeatably raster the incoming laser pulses across the test optic's surface with no significant changes to the beam profile or spot size. The pulse energy was also computer controlled by rotating a half wave plate positioned just in front of a polarizer. Beam profiles were taken of a representative pulse from the damaging pulse train using a cooled 16 bit Andor iKon camera. In

situ damage identification was accomplished using both a front surface scatter probe imaging the damage site, illuminated with a 5mW HeNe, and also viewing the beam profile of the transmissive HeNe and one micron beam deformation after passing through the test optic. Taken together, there was perfect correlation between these two in situ damage ID methods and post damage Nomarski microscopy.

The vacuum conditions in the vessel were constantly monitored by use of a Brooks Automation Ion Trap [67]. Representative partial pressure scans are shown in figure 55. The vacuum vessel was equipped with numerous additional ports to allow for the introduction of other metrology tools, unique gas mixtures and multiple beams and cameras. The vessel was wrapped with resistive heating tape and could be used to test samples at temperature, however, our interests in this work were for room temperature testing only. The entire apparatus was mounted on a mobile optical table to allow us to move to and from different laser sources in our lab spaces.

With these tools in hand we attempted to probe the unaddressed explanations for a reduced LIDT performance when tested in vacuum: reduced thermal conduction with surface water removal and laser induced surface defect creation (possibly in the form of oxygen desorption and/or dissociation).

CHAPTER VI. DATA AND RESULTS

To this point we have highlighted earlier work other groups have done on the materials we are interested in. We have also given background information on the physical processes that occur in ion beam sputtering and on different measurement techniques that were used in the course of our research on the thin film samples used in the studies. The results of our research are now presented in the form of journal and conference papers either presented, submitted or in various stages of the review process for publication.

Paper #1: Point Defects in Sc_2O_3 Thin Films by Ion Beam Sputtering

Author List

P. F. Langston, E. Krous, D. Schiltz, D. Patel, L. Emmert, A. Markosyan, B. Reagan, K. Wernsing, Y. Xu, Z. Sun, R. Route, M.M. Fejer, J.J. Rocca, W. Rudolph, and C.S. Menoni

Publication Information

Received 4 September 2013; revised 9 December 2013; accepted 10 December 2013; posted 11 December 2013 (Doc. ID 196855); published 15 January 2014

Abstract

We show that the concentration of oxygen interstitials trapped in Sc_2O_3 films by ion beam sputtering from metal targets can be controlled by modifying deposition conditions. We have identified point defects in the form of oxygen interstitials that are present in Sc_2O_3 films, in significantly high concentrations, i.e. ~ 10^{18} cm^{-3}. These results show a correlation between the increase of oxygen interstitials and the increase in stress and optical absorption in the films.

Sc_2O_3 films with the lowest stress and optical absorption loss at 1 micron wavelength were obtained when using a low oxygen partial pressure and low beam voltage.

Introduction

Sc_2O_3 is a transparent dielectric with a bandgap of ~ 6 eV, and a refractive index of ~ 2 at wavelengths around 1 μm [49]. For these characteristics it is sought as the high index component of dielectric coatings operating at wavelengths ranging from the ultraviolet (UV) to the mid-infrared. Sc_2O_3 has been used in the fabrication of quarter wave stacks and anti-reflection coatings in combination with SiO_2 and MgF_2 for UV applications [87]. Due to its high permittivity, Sc_2O_3 is also a candidate for replacement of SiO_2 as a gate oxide. Wang et al. [124] recently employed atomic layer deposition (ALD) to deposit Sc_2O_3 on AlGaN/GaN devices to achieve good electrical properties for transistor operation. However, ALD Sc_2O_3 was found to be sensitive to moisture and an Al_2O_3 blocking layer was required. Mixed oxides that incorporate Sc_2O_3 have now been reported. Yakovkina et al. [125] synthesized $(HfO_2)_{1-x}(Sc_2O_3)_x$ alloys as a replacement for the SiO_2 in metal-insulator-semiconductor devices. The authors found that chemical vapor deposition (CVD) of Hf-Sc-O films within a narrow range of Sc concentrations produced high permittivity and low current leakage, ~ 10^{-8} A/cm^2, films. Sc_2O_3/SiO_2 mixed oxide films deposited by ion beam sputtering (IBS) have also been reported [55]. This work used oxide targets to produce amorphous films ranging from pure SiO_2 to Sc_2O_3. Investigations of the laser damage behavior showed that in the nanosecond pulse regime, the laser damage was governed by defect density and showed a large difference between Sc_2O_3 and SiO_2. In contrast, in the short pulse regime laser damage behavior was found to be independent of composition [55].

In this work we describe a study of the optical and structural properties of amorphous Sc_2O_3 thin films deposited by ion beam sputtering. In contrast to a recent report by Mende et al. [55], we employ a Sc metal target to deposit the Sc_2O_3 oxide film [7, 126]. Among the advantages of using metal targets is the ability to tailor process parameters such as oxygen partial pressure and ion beam energy. A main objective of this work has been to identify modifications in the Sc_2O_3 structural and optical properties that are linked with the deposition process parameters. The results show that point defects in the form of oxygen interstitials are present in Sc_2O_3 films in significantly high concentrations, i.e. ~ 10^{18} cm^{-3}. The density of these defects varies with deposition conditions. The results show a correlation between the increase of oxygen interstitials and the increase in stress and absorption in the films. Sc_2O_3 films with the lowest stress and absorption loss at $\lambda = 1$ µm were obtained when using a low oxygen partial pressure and low beam voltage. Under these conditions the density of the oxygen interstitials in the as-deposited Sc_2O_3 films is minimized.

Experimental

Thin films of Sc_2O_3 were grown by ion beam sputtering using a Veeco Spector ®. In one set of runs the beam voltage of the main Ar sputtering source was set equal to 1250 V, the current at 600 mA and the variable was the oxygen partial pressure. The O_2 partial pressure was varied from 2 to 40 µTorr. In a second set, the oxygen partial pressure was constant at 3 µTorr and the energy of the Ar sputtering ions was varied between 600 and 1250 eV. The target was Sc metal with 99.9 % purity and Ta impurity of < 0.05 %. Sc_2O_3 single layers were grown on fused silica substrates with a surface roughness of 0.6 nm. The surface roughness was measured to be ~0.6 nm from scans obtained using a NovaScan ESPM 3D Atomic Force Microscope (AFM) operated in tapping mode with a 5 x 5 µm scan area.

Glancing angle x-ray diffraction (GAXRD) and x-ray photoelectron spectroscopy (XPS) measurements were carried out to determine the degree of crystallinity and the composition of these films respectively. The thicknesses and optical constants of the transparent films were determined using a combination of transmission and ellipsometric data. Deposited films had nearly constant thicknesses, (205 ± 7) nm, and were transparent. The refractive indices of all films at $\lambda = 1$ µm, extracted from ellipsometric measurements, was equal to 2. The magnitude and sign of the stress in the Sc_2O_3 films, grown on 1 mm thick fused silica substrates, were determined using a Twyman-Green interferometer. Fits of five phase- shifted interference patterns to Zernike polynomials were used to determine the radius of curvature of the film-substrate structure. Stress was calculated from the inverse of the radius of curvature [127]. The optical absorption of the films was measured at two different wavelengths, $\lambda = 1.064$ µm and at $\lambda = 0.514$ µm using the photothermal common-path interferometry (PCI) technique [114]. A pump beam at $\lambda = 1.064$ µm and $\lambda = 0.514$ µm was used to excite a thermal response in the coating, respectively, while common-path interference of a HeNe probe beam at $\lambda = 0.633$ µm allowed for detection of the absorption of the film at each pump wavelength.

Electron paramagnetic resonance (EPR) studies were carried out at room temperature using a Bruker EMX EPR spectrometer with 100 kHz field modulation. Films were deposited on thin fused silica slides and placed in a quartz sample tube. EPR spectra for each deposition condition were taken for nearly equivalent film volumes, in the same cavity, on the same day and with the microwave propagation normal to the film surface. The microwave frequency used to probe the spin populations was 9.6 GHz for the measurements taken. Background spectra confirmed that the bare substrates and quartz sample tube signals were insignificant compared to the signals measured from the Sc_2O_3 films. This small background signal was subtracted from

the scans of the Sc_2O_3 films. The relative spin concentrations were determined from the relative areas of the absorption signals. The EasySpin Matlab library was used to fit the spectra to extract a g-tensor [108, 128]. (All the analytical tools employed in this report have been detailed elsewhere [108].)

Results and Discussion

Figure 56 shows x-ray diffraction (XRD) spectra from the set of films deposited at different oxygen partial pressures in the range of 2 μTorr to 38 μTorr. The most prominent feature in the XRD spectra is the (222) diffraction peak of the cubic Sc_2O_3. The films are considered amorphous, as the crystallite size was determined to be ~ 10 nm based on the FWHM of the (222) peak compared with the crystalline quartz standard. An increase of the oxygen partial pressure affects the spectra in two ways: the position of the (222) peak shifts towards smaller θ and the full width at half maximum (FWHM) of the (222) peak increases by approximately 50%. Increases in the FWHM could be due to reduction in the crystallite size, increased stress or a combination of both. The shift of the diffraction peak towards smaller diffraction angles with increasing oxygen partial pressure indicates a change in the lattice constant that is correlated with increased compressive stress in the films. Analysis of the XRD spectra in the Sc_2O_3 samples deposited using different beam voltages showed the (222) peak shifted by ~ 0.1% and broadened by ~ 10% between 600V and 1000V. Results from independent stress measurements are shown in Fig. 57. The stress varied from 0.55 GPa to 0.75 GPa when the beam voltage was varied from 600 to 1250V. The stress in the Sc_2O_3 films deposited using different oxygen partial pressures varied from 0.77 to 1.3 GPa. Thus, the combination of low oxygen partial pressure and low beam voltage results in Sc_2O_3 films with the lowest stress.

The Sc_2O_3 thin films were also characterized by x-ray photoelectron spectroscopy (XPS) to assess the stoichiometry and bonding environment. These results showed that the Sc in the IBS Sc_2O_3 films is in a single binding environment, while analysis of the O1s peak showed the

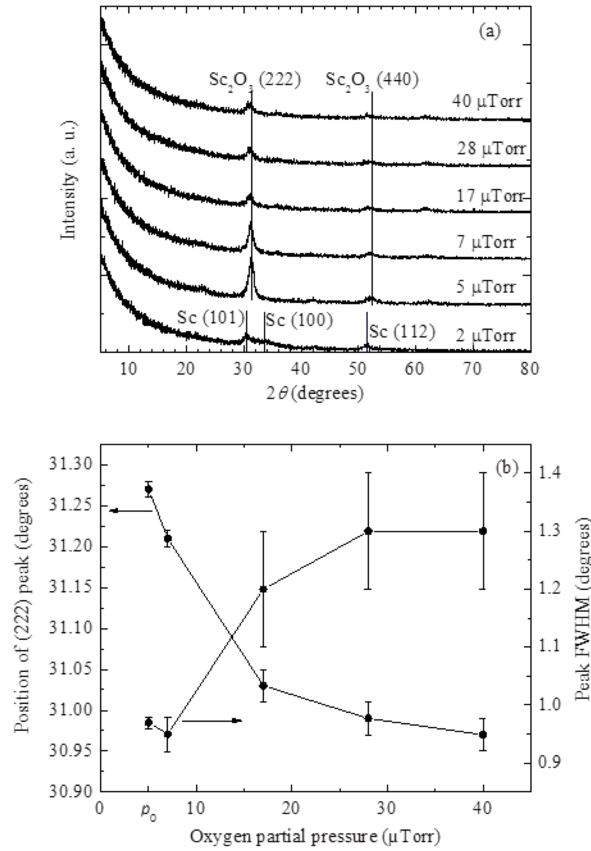

Figure 56: (a) X-ray diffraction spectra of amorphous Sc_2O_3 for films deposited as a function of oxygen partial pressure. The film obtained at 2 μTorr shows diffraction features of crystalline scandium, and was opaque. All other films instead showed diffraction peaks that are identified with the (222) and (440) peaks of cubic Sc_20_3. (b) The FWHM of the (222) peak increases and the peak position decreases to smaller angles with oxygen partial pressure, indicating an increase in the lattice parameter due to increased strain.

oxygen had more than one signature for all the measured samples, indicating oxygen trapped in the films. The stoichiometry in the films varied from 1.72 to 1.84 for beam voltages of 600V and 1000 V respectively. Instead, in the Sc_2O_3 films deposited using different oxygen partial pressures the stoichiometry varied from 1.84 to 2.05, showing excess O_2 in the films [7].

Figure 58 illustrates the characteristics of the EPR spectra from samples deposited using different oxygen partial pressures.

The signal was fitted using the EasySpin EPR Matlab tool to extract the g-tensor component values which for the dominant defect are: [g_{xx}=2.017, g_{yy}=2.017, g_{zz}=2.055]. This g-tensor corresponds to an oxygen interstitial defect [129]. EPR measurements on the samples deposited using beam voltages ranging from 600 V to 1250 V produced the same results in terms of the defect characteristics. The density of oxygen interstitials obtained from the spectra in Fig. 58 for the two sets of samples is presented in Table 1. These oxygen interstitial defect densities

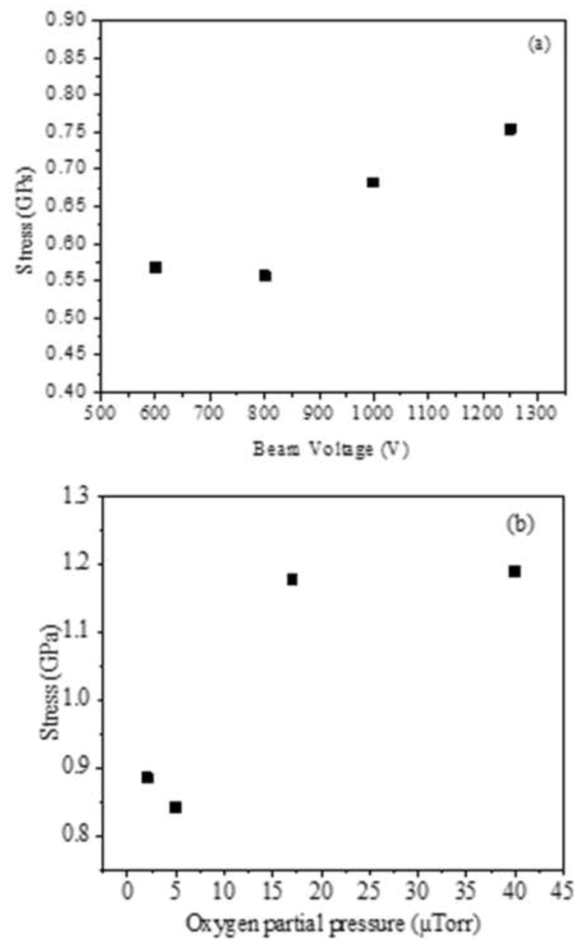

Figure 57: Stress in Sc_2O_3 films with (a) variation in the beam voltage and (b) variation in the oxygen partial pressure.

are 2-5 times lower in the samples deposited at different beam voltages than found in the sample set deposited at different oxygen partial pressures.

Figure 59 plots the absorptivity or absorption coefficient (m^{-1}) at λ=1.064 µm of the set of samples deposited by varying the oxygen partial pressure and beam voltage respectively.

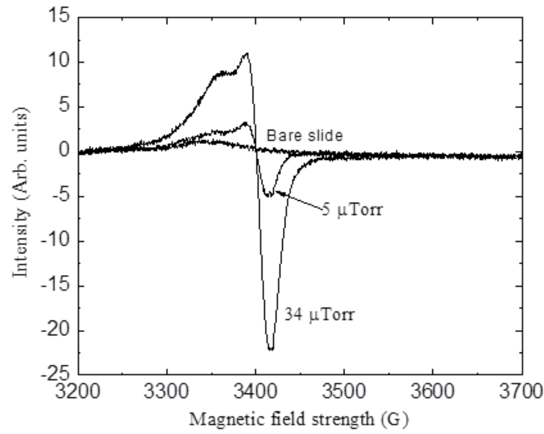

Figure 58: Electron paramagnetic resonance spectra for Sc_2O_3 films deposited at different oxygen partial pressures. A line shape analysis of the spectra is used to identify the defects and determine their density. An increase in the signal intensity correlates with a larger density of defects.

Table 1 Defect density determined from EPR for Sc_2O_3 deposited with different beam voltage and Sc_2O_3 deposited with different oxygen partial pressure.

Beam Voltage (V)	Defect Density (cm^{-3})
600	2.2×10^{18}
800	2.8×10^{18}
1000	3.8×10^{18}
1250	3.4×10^{18}
Oxygen Partial Pressure (µTorr)	Defect Density (cm^{-3})
5	1.3×10^{18}
7	3.9×10^{18}
38	1.04×10^{19}

The absorption coefficient increased with oxygen partial pressure by about a factor of 4x, while it only increased by 2x with an increase in beam voltage. The variation of the absorption

coefficient with process parameters correlates well with the variations in the density of oxygen interstitials. The data in Fig. 60 also show the absorptivity of the Sc_2O_3 films deposited using

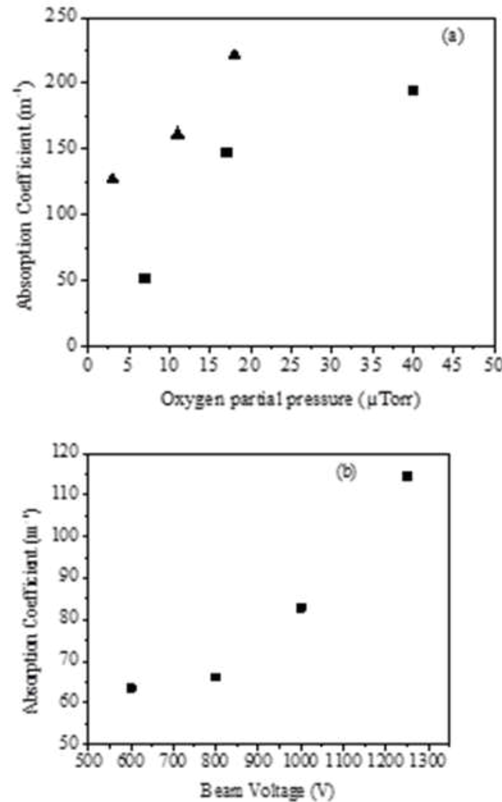

Figure 59: Absorptivity of amorphous Sc_2O_3 films deposited using (a) different oxygen partial pressures and (b) different beam voltages. The triangle symbols identify a set of samples grown without use of the assist source. Both sets of data show an increase in absorptivity with oxygen partial pressure. The increase in absorptivity correlates with the increase in the density of oxygen defects.

different oxygen partial pressure with the use of the argon assist source during deposition. We attribute the decrease in absorptivity with the use of the assist source to preferential sputtering of oxygen and associated reduction in the density of oxygen point defects.

The absorptivity of the Sc_2O_3 films was also measured at $\lambda = 0.514$ μm. These results showed the absorptivity to be significantly larger, ~ 10x, than at $\lambda = 1.064$ μm (Fig. 60). Absorption in the large bandgap Sc_2O_3 films is due to the presence of trap states. These results

suggest the presence of trap states at energies of 1.165 eV and at 2.412 eV near the band-edges. We do not have sufficient information to discern if these trap states are discrete energy states in k-space or a broad band as the absorption measurements were carried out at discrete wavelengths. Further studies are needed to identify the origin of the defect bands. This behavior is not unique to Sc_2O_3. We have shown that similar trap levels exist in IBS Ta_2O_5 and that the population and depopulation of these traps by electrons impacts the absorption of the films [130] .

The parameter space in IBS is very broad as there are many degrees of freedom to realize thin films with similar optical and structural properties. In these studies we choose to vary the oxygen partial pressure because this is a critical parameter for reactive sputtering of metal oxides. We choose to vary the beam voltage because it has a direct impact on the energy distribution of the sputtered Sc target neutrals, and on the energy of reflected Ar neutrals [131]. The sputtering rate is also reduced when reducing the beam voltage.

An increase of the oxygen partial pressure results in an increase of the oxide-to-metal target coverage and in the oxygen trapped within the growing film [108, 132, 133]. In both cases we have identified oxygen interstitials as being present. The concentration of oxygen interstitials was found to be an order of magnitude lower in the set of Sc_2O_3 samples deposited using different beam voltages compared with the set of samples deposited using different oxygen partial pressure. The scaling of the absorption and stress in the films with increased oxygen partial pressure suggests that these defects play a role in affecting the optical and mechanical properties of the Sc_2O_3 thin films.

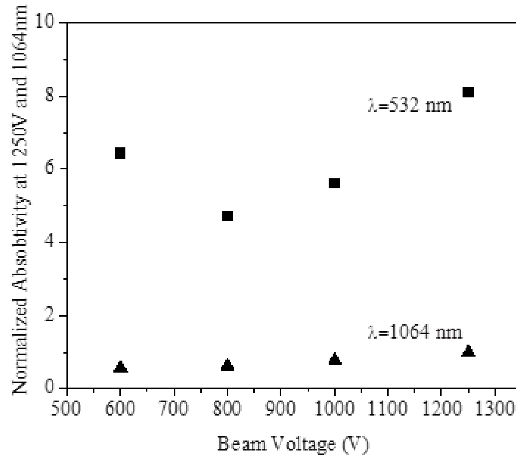

Figure 60: Normalized absorptivity for Sc_2O_3 films at λ = 1064 nm and λ = 514 nm. The data was normalized to the value of the absorptivity at λ = 1064 nm for the film deposited at a beam voltage of 1250 V.

Conclusions

Isolating the role of defects in IBS metal oxide thin films in the optical and mechanical properties of amorphous metal oxides is quite challenging. In this work, we have identified oxygen interstitials. Signatures of these defects were also found in IBS HfO_2 and Ta_2O_5 and were observed to scale with thickness of the film [134, 135]. However, it is possible that other types of defects, such as oxygen vacancies, could be affecting absorption, and stress in the amorphous Sc_2O_3. In crystalline HfO_2, model predictions show there exists a distribution of deep and shallow defects states within the bandgap [46]. Different experiments are required to identify other types of bulk defects. Moreover, the effect of surface and interface defects in the absorption and stress in Sc_2O_3 amorphous thin films should not be discounted.

This work was supported by the Office of Naval Research, and the High Energy Laser Program from the DoD Joint Technology Office, grants No. N00014-09-1-0049, N0014-07-1-1068 and W911NF-11-1-0007. It made use of facilities developed through the NSF Engineering Research Center Program.

Paper #2: Damage Performance of Optimized Sc_2O_3 and HfO_2 Single Layers Tested in Air and Vacuum Including the Influence of Very Thin Capping Structures

Abstract

A damage test apparatus was developed to allow testing of ion beam sputtered single layers and capped single layers of Sc_2O_3, HfO_2 and Ta_2O_5 in a controlled atmosphere and in an ultra-high vacuum environment. All damage testing was done using a 100-on-1 testing format at a wavelength of 1030 nm using a ~375 +/- 20 ps pulse duration. The in air damage testing measured a zero % probability LIDT value of 18 J/cm^2 for Sc_2O_3, a 13 J/cm^2 threshold for HfO_2 and a 10.9 J/cm^2 threshold for Ta_2O_5. The threshold values for these same films measured in the UHV were 8.5 J/cm^2 for Sc_2O_3, 9.2 J/cm^2 for HfO_2 and 4.9 J/cm^2 for Ta_2O_5. The influence of adding a 10 nm ultra-thin capping layer of SiO_2, Sc_2O_3, HfO_2 and Ta_2O_5 to basecoat films of Sc_2O_3 and HfO_2 were measured and the results are discussed. Lastly, defect densities were calculated for the different samples based on the damage probability curves measured in air and in vacuum.

Introduction

Improvements in the laser damage performance of thin film materials used to engineer anti-reflective and high reflective coatings at wavelengths ranging from visible to near infrared has been and continues to be of great importance in the laser community at large. The study of laser damage initiation in coating materials has been ongoing for over forty years yielding significant improvements in our understanding of material properties, including mechanical and optical performance. Areas that have not been studied in depth and consequently limited information is available are: the influence of first surface interfaces and that of vacuum on the laser induced damage threshold (LIDT) performance of Ion Beam Sputtered (IBS) metal oxide

films. The work discussed in this paper studies the difference in the LIDT performance of ion beam sputtered high index materials, Sc_2O_3, HfO_2 and Ta_2O_5 when measured in air and in vacuum. These materials, along with SiO_2, form the backbone of optical interference film technology. We report on LIDT measurement results of high index thin film oxides tested in controlled air and ultra-high vacuum environments. To investigate the effect of interfaces on the LIDT, samples incorporating a capping layer were tested. The LIDT data were analyzed to extract defect densities in air and vacuum. We also present a strategy for increasing the LIDT performance of these same materials when used in vacuum. The importance of this work becomes evident in the quest for ever higher peak power laser systems as well as the proliferation of terawatt and petawatt class systems at public and private laboratories. Pulse compressor optics, space based optics, Free Electron Laser (FEL) mirrors, cryogenic active mirrors and others have all demonstrated a significant decrease in the LIDT performance of metal oxide films when used in low pressure environments. This decrease in the LIDT performance has been known for some time but the reasons for this decrease remain uncertain. Water impregnation in the film, carbon contamination, decreased thermal conductance and oxygen dissociation have all been proposed as possible explanations for this behavior. However, limited evidence has been presented to substantiate these arguments [34, 36, 58-60, 64, 68, 83, 86, 136].

Experimental details

Single layers, 100 nm thick, of amorphous Ta_2O_5, Sc_2O_3 and HfO_2 were grown by ion beam sputtering onto superpolished fused silica substrates. A beam voltage of 1250 V and beam current of 600 mA were used. The oxygen flow was selected to realize the lowest absorption in the films [6]. A second set of single layer samples with a 10 nm thick capping layer were grown.

The 10 nm thick layer does not significantly affect the optical properties of the samples. The transmittance spectrum is shifted towards longer wavelengths as a result of the increase in thickness. The standing wave electric field is insignificantly modified as shown in figure 61 below where three plots, 100 nm HfO_2 single layer and the same single layer capped with 10 nm of SiO_2 and 10 nm of Ta_2O_5, appear nearly identical to one another.

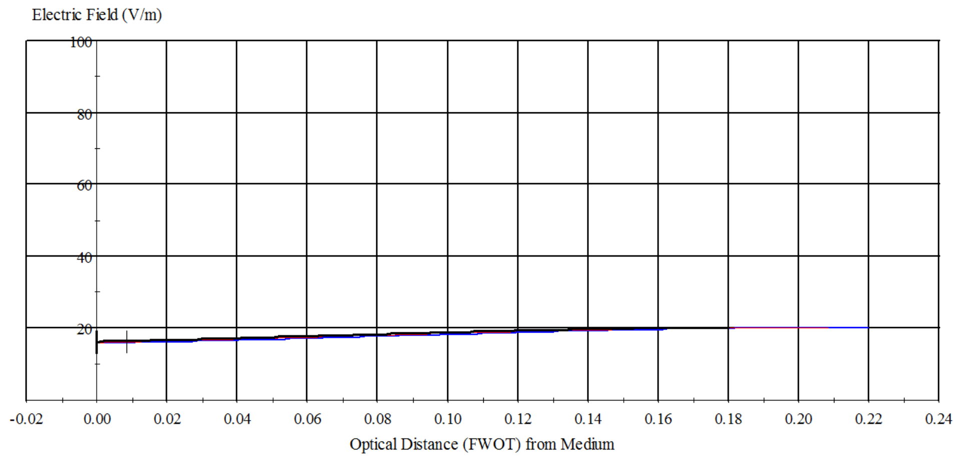

Figure 61: Standing wave electric field for capped and uncapped HfO_2

These samples were grown using optimal deposition conditions for realizing lowest absorption at 1 μm. These conditions for Sc_2O_3 were presented and discussed in an earlier paper our group published [6]. Similar development work was done for our HfO_2, Ta_2O_5 and SiO_2 films. As with the work we presented for Sc_2O_3 all films were grown using conditions that resulted in fully stoichiometric, amorphous, low stress and minimum EPR defect signature and absorption loss at 1 micron. The absorption losses for the set of single layer and capped samples used in this work is summarized in table 2 below.

Table 2: Absorption at 1 μm

Sc_2O_3	Sc_2O_3/ SiO_2	Sc_2O_3/ HfO_2	Sc_2O_3/ Ta_2O_5	HfO_2	HfO_2/ SiO_2	HfO_2/ Sc_2O_3	HfO_2/ Ta_2O_5	Ta_2O_5
7.3± 0.6ppm	6.3± 0.2ppm	7.0± 0.4ppm	9.4± 0.2ppm	11.9± 0.4ppm	11.0± 0.3ppm	11.8± 0.4ppm	10.6± 0.3ppm	5.7± 0.3ppm

LIDT testing was carried out using a new ultra-high vacuum (UHV) chamber capable of reaching 10^{-9} torr built for this purpose. This system is equipped with a load lock where a clean test optic is introduced prior to placing it inside the UHV chamber. In the load lock chamber the sample is cleaned for ten minutes on each side using an oxygen plasma cleaner from XEI to remove hydrocarbon contamination [123]. Confirmation of the carbon removal is made by means of a Brooks Automation ion trap monitor recording partial pressures of elements and molecules in the main chamber with mass ranging from 0.5 to 300 amu [137]. The only carbon compound seen in the chamber prior to testing was CO_2 with a partial pressure of $< 4*10^{-11}$ torr, as shown in figure 62. All vacuum testing was done with a base pressure of $< 5*10^{-9}$ torr. This process, from sample introduction into the load lock chamber to beginning the LIDT test, typically took eight hours. Using the same procedure, LIDT measurements were carried out in the UHV chamber at room temperature filled with ultra pure air to allow for direct comparisons between data sets taken in air and in vacuum.

In this ion trap scan, figure 62, made on a representative sample with a base pressure of $4.11*10^{-9}$ torr the peaks at 16, 17 and 18 amu are associated with water in the system. The peak at 28 is a nitrogen peak and the peak at 44 is CO_2. The low partial pressure ($7.2*10^{-11}$ torr) of the only carbon compound, CO_2, in the vacuum chamber, determined prior to damage testing, eliminates all possibilities that deposition of carbon on the surface of the optics play any role in

the vacuum damage testing. It was previously shown that removal of hydrocarbons is crucial in reliable LIDT measurements [138].

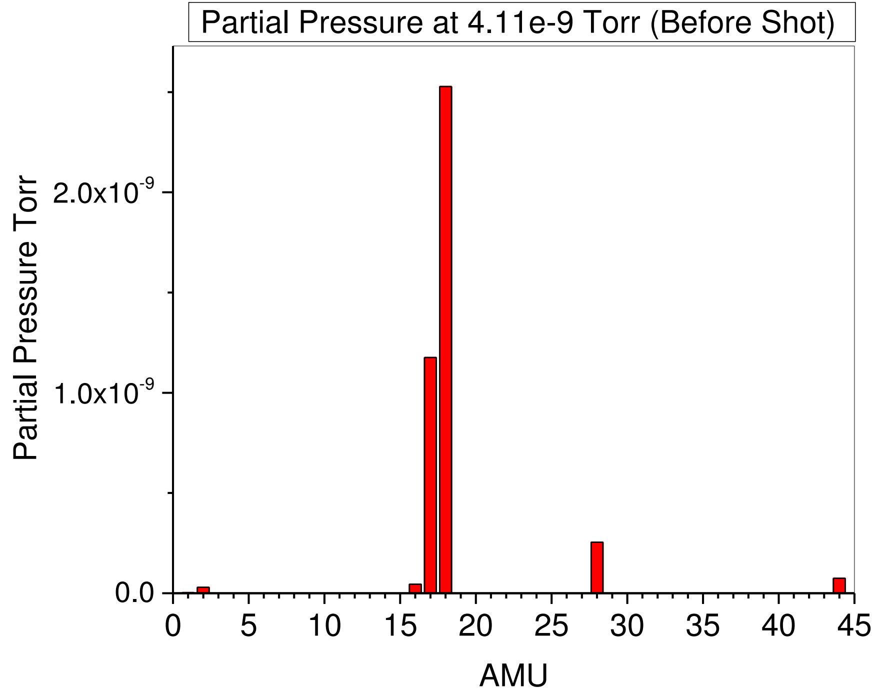

Figure 62: Partial pressure measurement of UHV chamber with sample installed.

The LIDT of these films were assessed using a 100-on-1 protocol. An all-diode-pumped, mode-locked chirped pulse amplified Yb:YAG system was used for this test. This system consisted of a Yb:KYW oscillator pumped by 30 watts of fiber coupled 980 nm light. The oscillator produces ~20 nJ pulses of 300 fs duration with a repetition rate of 57 MHz. A subset of these pulses are stretched then amplified in a cryo-cooled Yb:YAG amplifier pumped with a 90W fiber-coupled laser diode operating at 940 nm. The system is capable of 100 Hz operation at λ=1030 nm, producing pulses of 5 ps duration and 100 mJ of energy. For these experiments only a single one second exposure to uncompressed pulse of 375 ps $\pm$ 20 ps were required at

each test site [139, 140]. The laser was focused onto the test optics to a spot size ~ 100 µm FWHM using a ~275 mm focal length lens with a confocal length of about 16 mm.

Given the low pressures we intended to operate at, as well as the types of monitoring equipment we needed to employ, it was determined early on that the optical system would need a beam director to move the focused laser across the test optic's surface. This was accomplished by means of two computer controlled mirror mounts acting in concert with a motorized two axis lens stage. The lateral position of the laser focused spot was controlled to better than one hundred microns across a half inch scan on the test optic surface with this variation being primarily due to beam jitter in other optical elements in the system. The size and shape of the focused spot appeared identical at all test sites. A schematic description of the damage testing apparatus and pictures are shown in figures 63 – 64.

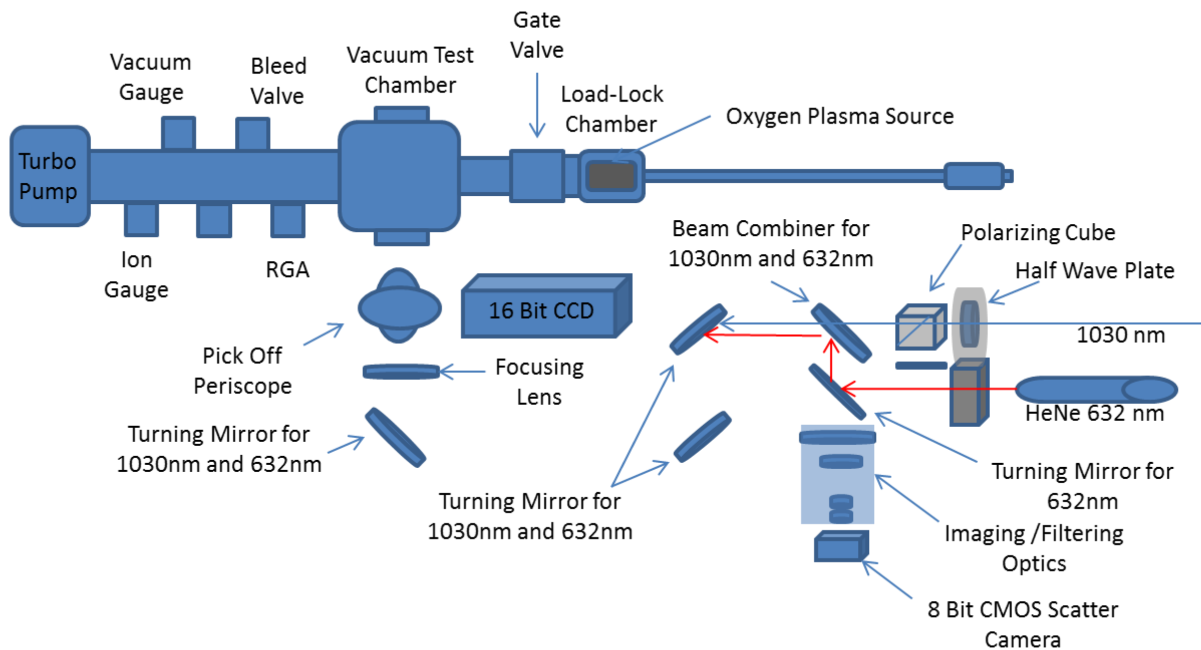

Figure 63: Diagram of UHV damage test apparatus

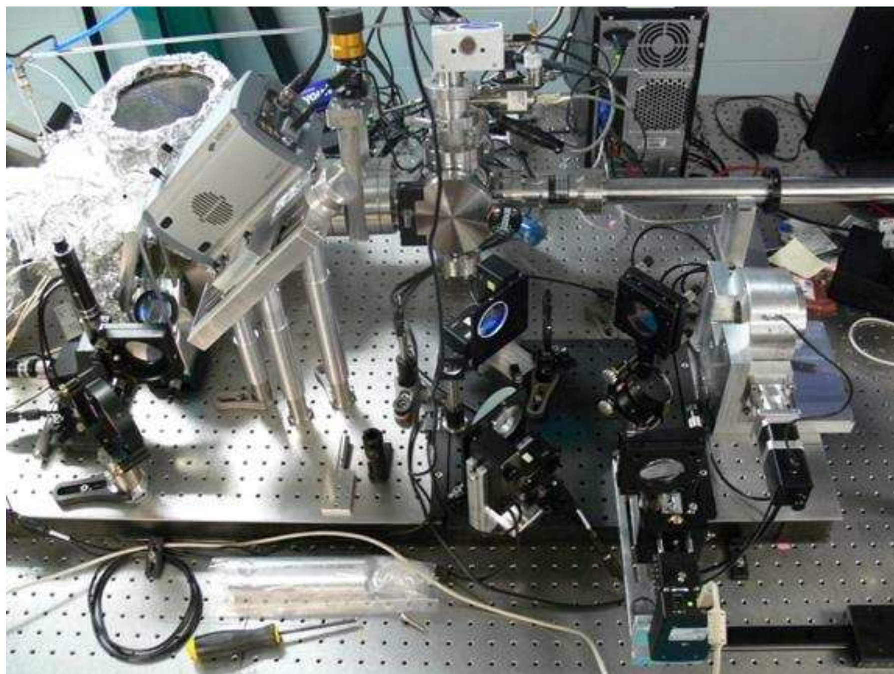

Figure 64: Picture of UHV beam director

Results and discussion

Single layers of Ta_2O_5, HfO_2 and Sc_2O_3, all 100 nm thick, were damage tested in the UHV chamber filled with ultra pure air and in vacuum with a base pressure below $5*10^{-9}$ torr. The general trend observed in single layers is that the LIDT increases in the higher band gap materials with the exception of Sc_2O_3 in vacuum. The same is observed when adding a capping layer, again with the exception of the Sc_2O_3 capping layer in vacuum. All samples with a SiO_2 capping layer demonstrated the higher LIDT in pure air and in UHV testing. This section starts by presenting the LIDT data for the two testing conditions. Lastly, I describe an analysis of the damage probability curves that allows one to extract defect densities for the different samples tested.

A. In Pure Air LIDT Testing

Figure 65 shows the LIDT damage fluence for each of the single layers investigated. The trend that is observed is that the LIDT increases as the band gap of the material increases. We choose to scale with bandgap because of its previous use in the scaling of ultrafast laser damage. However, one has to consider that testing with pulse durations of ~375 ps does not fall in the deterministic, ultrafast damage regime [141].

An uncoated fused silica sample tested using the same cleaning methods and identical test conditions damaged at 47 ± 2.4 J/cm^2. Here the uncertainty represents the variation in the pulse to pulse energy. The error in this and all of our damage value measurements nominally is 3%. As our measured error is smaller than the standard deviation, the standard deviation is shown in the data. It should be noted here that the damage threshold tests done on the bulk fused silica samples exceeded the critical power limit, ~ 4.3 MW, for self focusing in silica [142]. While there is no doubt that self focusing occurs in the bulk of fused silica, we were careful to record the fluence associated with surface damage. The other samples tested did not suffer from the effects of self focusing because the beam was focused on the surface where damage was observed at nearly one third the threshold fluence of the bulk material. Again, we were careful to record the fluence associated with surface damage in addition to the fact that no bulk damage was seen in any of the single layers or capped samples tested.

Other work has demonstrated the need to address the influence of stimulated Brillouin scattering (SBS) in the sample resulting in an enhanced front surface intensity and a reduced damage threshold value [143]. Given our relatively short pulse testing and large spot sizes, electrostriction of the sample would occur on a time scale of tens of nanoseconds. We are testing

using pulse widths an order of magnitude reduced from these values meaning SBS does not significantly influence the onset values and therefore was not considered in our analysis.

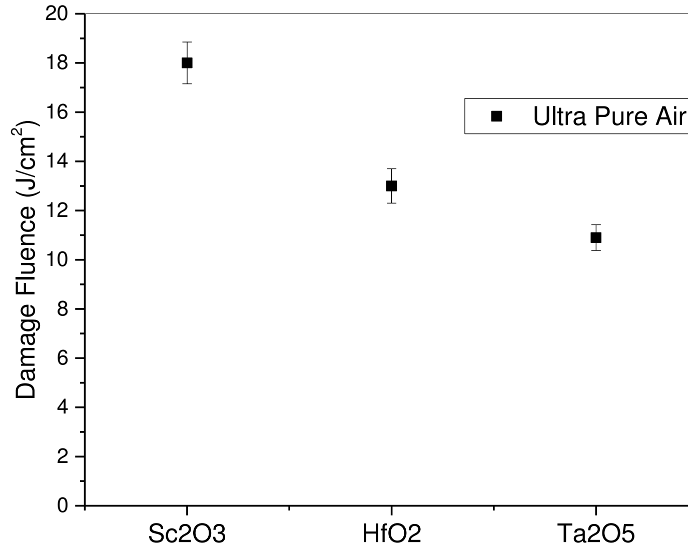

Figure 65: The zero % probability LIDT results of single layers tested in clean air (FS damaged at 47 ± 2.35 J/cm^2)

Figure 66 shows the results of LIDT tests on the Sc_2O_3 samples grown with a 10 nm overcoat of different metal oxides. The results show the addition of an SiO_2 capping layer improves the LIDT. Instead the LIDT reduces when adding capping layers of HfO_2 and Ta_2O_5. The relative magnitude of the decrease in the LIDT value for the HfO_2 capped sample seems anomalous. An explanation for this behavior is found in a comparison of the actual damage onset curves, shown in figures 68 and 69.

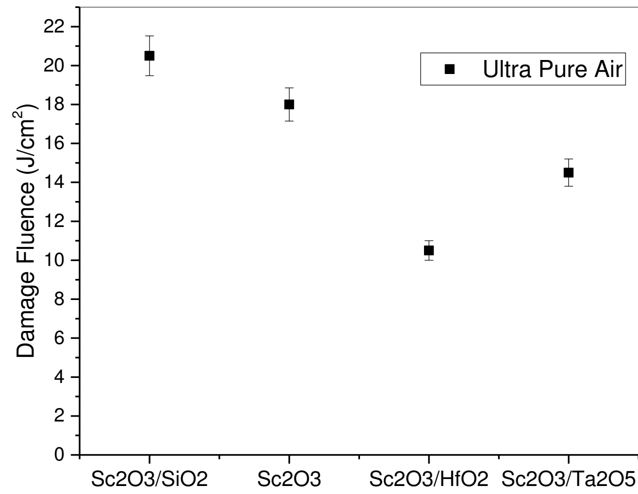

Figure 66: The zero % probability LIDT results of Sc_2O_3 basecoat series tested in clean air (FS damaged at 47 ± 2.35 J/cm^2)

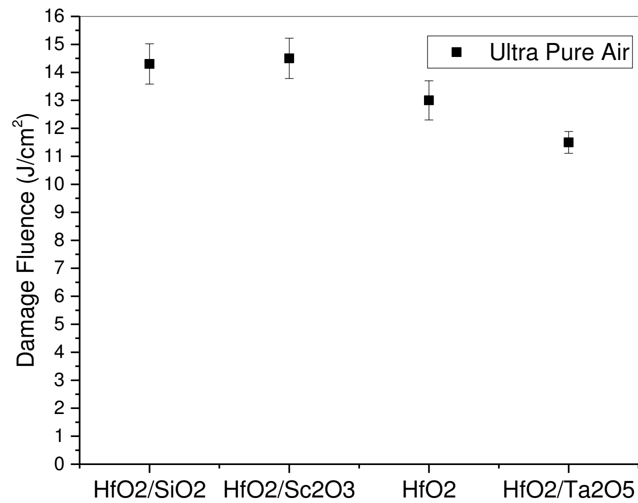

Figure 67: The zero % probability LIDT results of HfO_2 basecoat series tested in clean air (FS damaged at 47 ± 2.35 J/cm^2)

Figure 67 shows the results of LIDT tests on the HfO_2 samples grown with a 10 nm overcoat of different metal oxides. The trend in the LIDT values for these samples shows a ~10% increase in LIDT when using a material with a larger bandgap and a ~10% decrease when using a lower bandgap material. The variations in LIDT are lower than observed in the capped Sc_2O_3 basecoat samples.

Figure 68 shows damage onset curves for Sc_2O_3 basecoat samples. Analysis of the traces shows that there are no damage events between zero and 30% except when HfO_2 is used as a capping layer. This boundary is shown in figure 68 by the blue line.

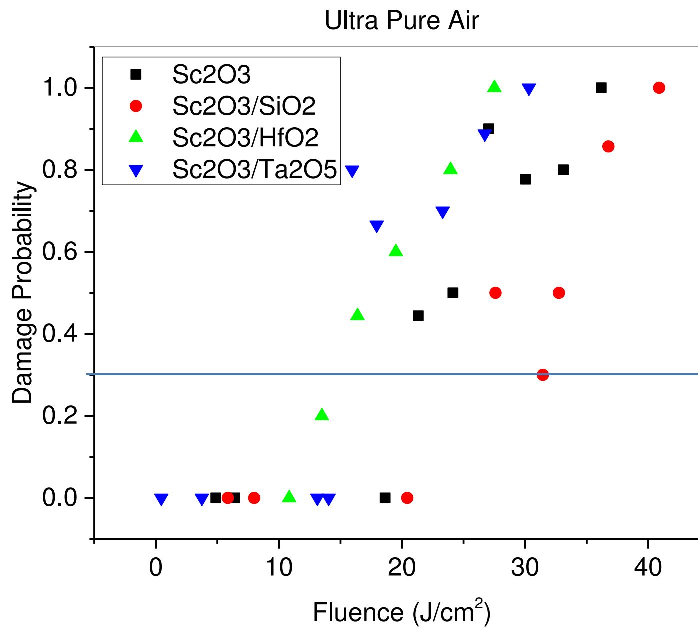

Figure 68: The zero % probability damage onset curves for Sc_2O_3 basecoat series tested in clean air

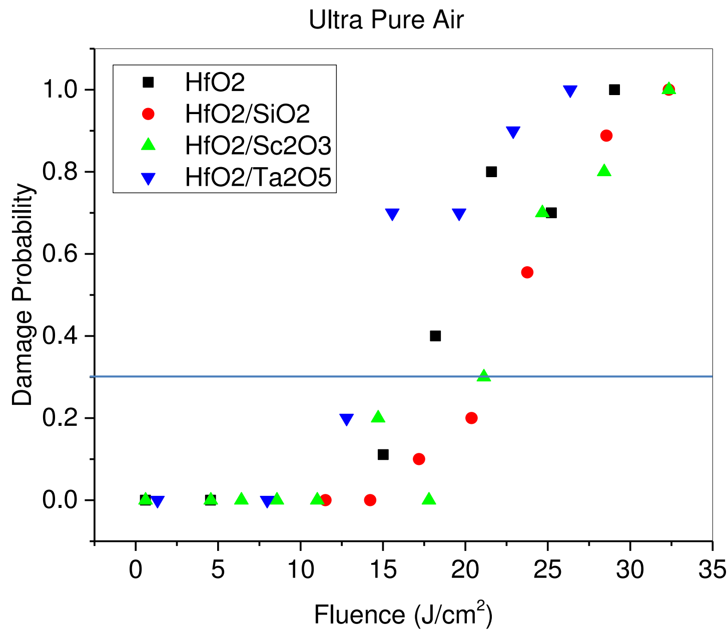

Figure 69: The zero % probability damage onset curves for HfO_2 basecoat series tested in clean air

In contrast all the HfO_2 basecoats capped with different oxides show damage within the zero to 30% probability range (Fig. 69). These results suggest a different type of defect is 'turned on' at lower fluences compared to the results obtained in the Sc_2O_3 series.

One family of defects that may match this defect description is nanoscale absorbing clusters [144]. When looking at the damage results of these capping layer tests the most glaring observation is the profound impact of adding only ten nanometers of material to these basecoats. If the major contributor to the damage process is bulk absorption in the basecoat one could expect to see a very minimal modification to the single layer damage performance with the addition of a 10 nm capping layer. Instead we have observed a greater than 2x variation in the onset thresholds for the Sc_2O_3 basecoat series when considering all four samples in the series and nearly a 20% variation in the HfO_2 basecoat series. These results strongly suggest interface

defects are the dominant contributor to laser damage in the majority of our films which is consistent with generally accepted and observed damage behavior [22].

B. In Ultra-High Vacuum Testing

Next the results of damage testing at ultra-high vacuum are discussed. In other work using femtosecond pulses the single shot damage threshold on metal oxide films was found to not be influenced by the presence of vacuum as there is no opportunity for sub-damage threshold surface modification [34, 145]. For this reason all our tests were performed with 100 shots at a constant fluence per test site or 100-on-1.

Figure 70 compares the 0% probability damage fluence for the single layers of Sc_2O_3, HfO_2 and Ta_2O_5 in ultra pure air and UHV. For all samples the LIDT of the samples in UHV is lower than in ultra pure air. However, the relative change is most significant for Sc_2O_3.

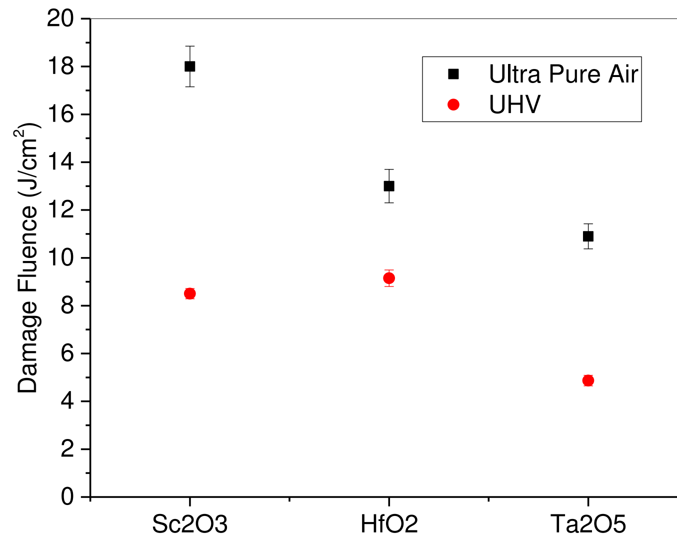

Figure 70: The zero % probability LIDT results of single layers tesed in air and vacuum (FS damaged at 47±2.35 J/cm^2 in air and at 52.6±2.6 J/cm^2 in vacuum)

Previous work has shown a major decrease in the LIDT performance of interference films when tested in vacuum [33, 34, 146-148]. A similarly dramatic decrease is not seen in metal optics and in fact there are instances of improved LIDT performance of metals in vacuum [86]. The LIDT decrease in interference films has been discussed in several papers. It is attributed to: substrate influences [86], vacuum dehydration causing increased tensile stress [60], rapid expansion of super heated surface H_2O, increased thermal conductivity of surface H_2O [36], hydrocarbon contamination [33, 58, 63, 147] and/or surface defect creation [34, 59, 68, 83, 145].

In our tests, we can rule out hydrocarbon contamination. Additionally, earlier work [148] was able to discount the influence of water impregnation in IBS deposited materials.

Our data show Sc_2O_3 appears to be the most susceptible to vacuum mediated defects while HfO_2 appears to be least influenced by a vacuum environment. Additionally, when the Sc_2O_3 and HfO_2 basecoats are capped with 10 nm of SiO_2 we did not see a decrease in the LIDT performance for either basecoat series, seen in figures 71 and 72. The LIDT values for these two films, SiO_2/Sc_2O_3 and SiO_2/HfO_2, were almost identical to their in air values. While this test was only a 100-on-1 damage onset there certainly was the opportunity for laser induced surface modifications during this exposure. Furthermore, these results would seem to discount the possibility of the absence of surface water influencing the LIDT performance of our films in vacuum. The electric field distribution found using Macleod design software for these films is almost indistinguishable from the distribution seen in the basecoat alone given the very thin capping layers used. The explanation for the lack of a decrease in the onset value for these films is likely the superior optical and mechanical qualities of SiO_2 coupled with the fact that in a low pressure environment any plasma formation near the surface would be allowed to expand away from the surface more quickly than at atmosphere conditions. The IBS SiO_2, was deposited from

an oxide target, which ensures consistency in the quality of the films. Moreover, IBS SiO_2 is characterized with the lowest linear absorption of all the materials tested.

Surface chemistry modification is the most likely explanation for multi-pulse LIDT behavior of IBS metal oxide thin films. SiO_2 in the form of bulk fused silica has a markedly higher LIDT performance compared with all the thin films tested. Moreover, the in-vacuum LIDT value for uncoated fused silica was 52.6 ± 2.6 J/cm^2, equal to or slightly larger than the in air LIDT value. IBS SiO_2 appears to possess some of the laser damage resistance characteristics seen in the bulk material when tested in vacuum. Laser induced surface modifications are not observed, at least for these low pulse counts.

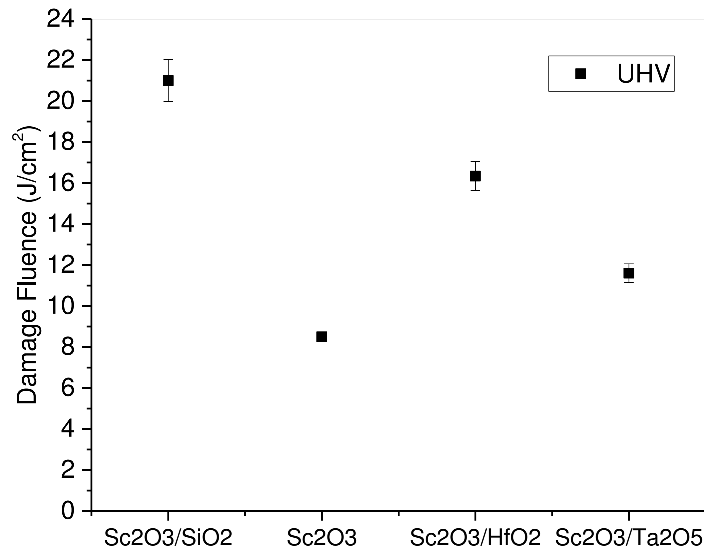

Figure 71: The zero % probability LIDT results for Sc_2O_3 basecoat series tested in UHV (FS damaged at 52.6 ± 2.6 J/cm^2)

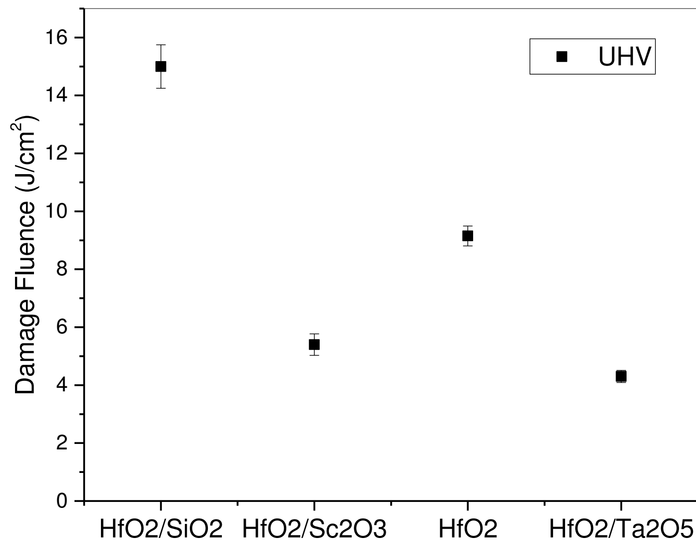

Figure 72: The zero % probability LIDT results for HfO_2 basecoat series tested in UHV (FS damaged at 52.6±2.6 J/cm^2)

Referencing the Sc_2O_3 basecoat series, the uncoated Sc_2O_3 film performed remarkably poorly in relation to the other samples in the test series. Figure 71 shows the LIDT fluence for Sc_2O_3 without and with different capping layers. The behavior of the samples with capping layers is totally unpredicted in that in all cases, the LIDT fluence increased.

In contrast, HfO_2 behaves more or less as expected based solely on the band gap of the capping layer, except for the Sc_2O_3 capping layer which has nearly the lowest LIDT as shown in figure 72. As was discussed already, the SiO_2 capped HfO_2 film performs well in vacuum with potentially no degradation in performance from the in air LIDT value. The HfO_2 single layer also performs relatively well when compared with the other two single layers tested, a 100 nm Sc_2O_3 and Ta_2O_5. The decrease in the LIDT performance of the HfO_2 single layer measured in vacuum relative to its value in air shows the least variation of the three high index materials. The Sc_2O_3

capped HfO_2 sample displayed a major departure from its in air LIDT value with the Ta_2O_5 capped HfO_2 showing a similar trend although not quite as large.

In combination, the results of figures 70, 71 and 72 suggest that Sc_2O_3 is more susceptible to laser damage in vacuum than any other metal oxide we tested. On the contrary, Sc_2O_3 is the best performing in terms of LIDT high index material in air. These results suggest laser induced surface defect creation in vacuum, as opposed to either in the bulk film or within the capping layer, is the dominant process leading to damage in these films.

For the sake of completeness we have included the actual damage onset curves for the Sc_2O_3 and HfO_2 samples tested in vacuum, figures 73 and 74. The probability traces are analyzed in section D to extract defect densities and gain more insight into possible damage mechanisms.

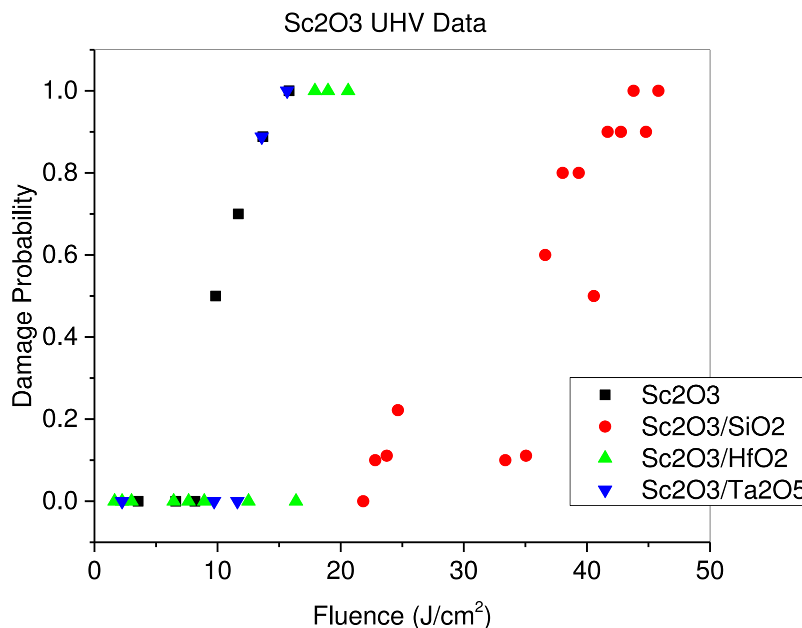

Figure 73: The zero % probability LIDT results for Sc_2O_3 basecoat series tested in UHV

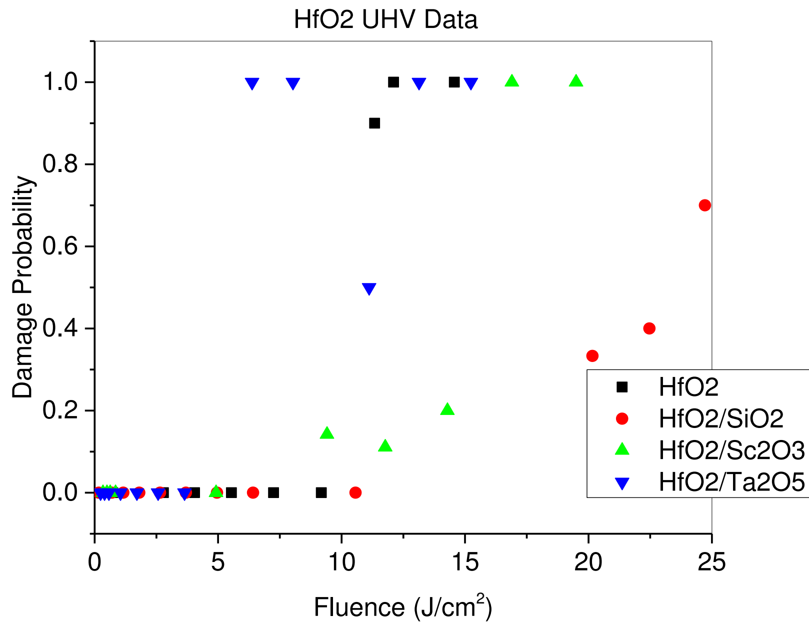

Figure 74: The zero % probability LIDT results for HfO_2 basecoat series tested in UHV

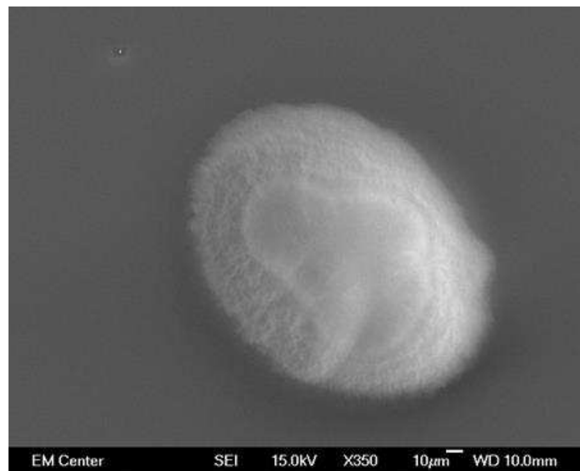

Figure 75: Typical 100 on 1 damage site on 10 nm SiO_2 capped Sc_2O_3

Figure 75 is an SEM image of a representative sample of a typical damage site on a capped single layer from our testing. This damage site shows evidence of melt on the perimeter of the crater with evidence of delamination down to the substrate.

As discussed earlier, the absence of water on the in vacuum surfaces did not significantly alter the performance of the SiO_2 capped samples. This suggests the increased thermal load to the metal oxide tested in vacuum, owing to a reduced water layer, is not significant in any of our materials. It appears that a 10 nm thick SiO_2 layer can passivate surface defects in Sc_2O_3 and HfO_2 making the LIDT of these samples insensitive to atmospheric conditions (figures 76 and 77). The data of figure 76 show that both HfO_2 and Ta_2O_5 capping layers can also passivate defects that lead to laser damage on Sc_2O_3 in vacuum. This situation is reversed in the behavior of the LIDT of HfO_2 in vacuum.

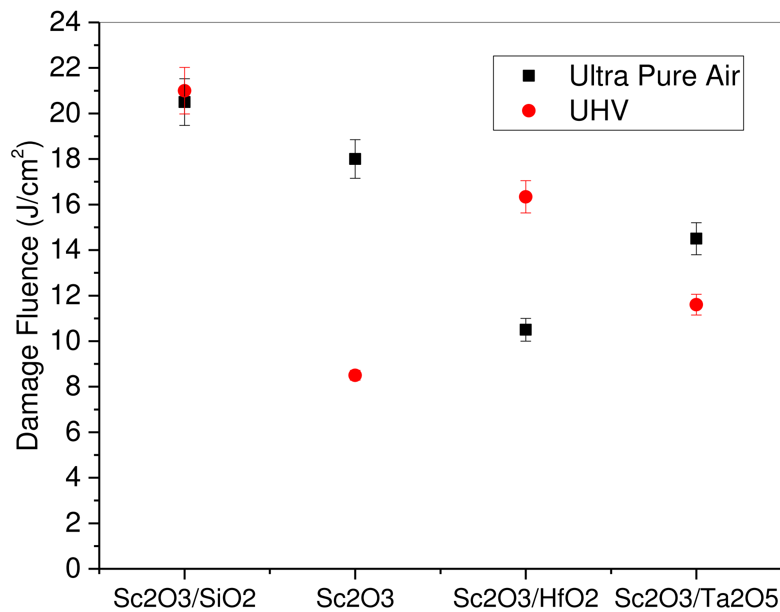

Figure 76: The zero % probability LIDT results for Sc_2O_3 basecoat series tested in air and vacuum (FS damaged at 47 ± 2.35 J/cm^2 in air and at 52.6 ± 2.6 J/cm^2 in vacuum)

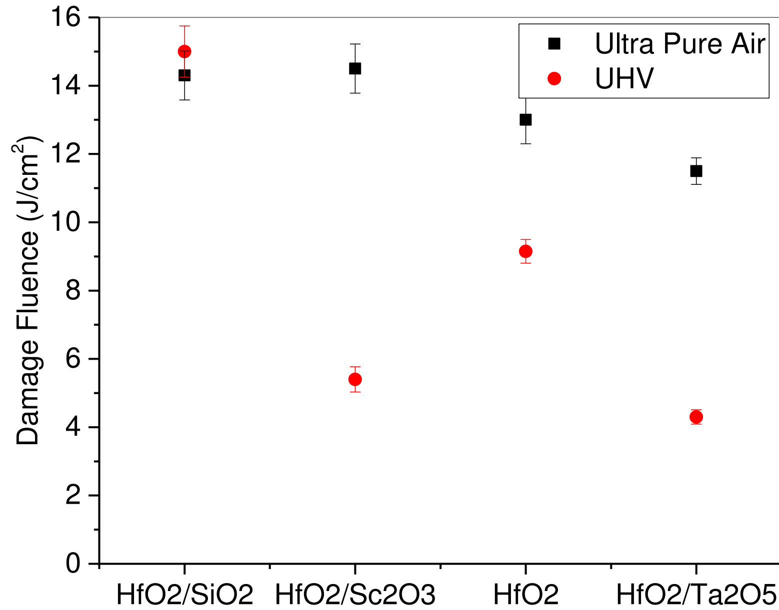

Figure 77: The zero % probability LIDT results for HfO_2 basecoat series tested in air and vacuum (FS damaged at 47$\pm$2.35 J/cm^2 in air and at 52.6$\pm$2.6 J/cm^2 in vacuum)

The fact that laser mediated surface absorption in the SiO_2 capped samples and the HfO_2 capped Sc_2O_3 samples is absent, as explained above, may be due to the high quality of the SiO_2 topcoat. It is likely that since SiO_2 is deposited from an oxide target, the 10 nm thick layer is very uniform and has extremely low absorption loss. The reduced surface absorption of the HfO_2 capped Sc_2O_3 in vacuum may well be a result of surface cleaning, plasma expulsion, and potential laser conditioning. From the data already presented, we have reason to believe the HfO_2 capped Sc_2O_3 likely has higher absorbing defects distributed throughout the volume of the capping layer. These are the type of defects that are traditionally targeted for removal by laser conditioning [149, 150]. Unlike in most published examples of laser conditioning, in our case the HfO_2 is only 10nm thick, so any defects in the film may be thought of as near surface defects capable of being removed without causing catastrophic coating damage. As previously

discussed, the lack of air in the vacuum test on this sample may allow for the rapid expulsion of these defects before collateral damage can form [86] [138]. From the single layer testing that was done, we know the performance of the 100 nm HfO_2 single layers showed the least change when measured in both air and vacuum. This suggests that the HfO_2 surface chemistry may not suffer as much from the reducing environment that exists in vacuum. If these higher absorbing volume defects can be removed from the capping layer without too much collateral damage, this film may be expected to perform very well given the heat conduction capacity of the Sc_2O_3 base coat.

As topcoats, both Sc_2O_3 and Ta_2O_5, which showed the greatest decrease in their LIDT performance as single layers tested in vacuum compared with their in air performance, show the largest susceptibility to laser induced surface defect creation.

C. Analysis of Defect Densities from the Laser Damage Probability Data

On the assumption that no defects exist in our films below the onset threshold, the damage defect density δ(F), as a function of laser fluence, can be described by a power law [16, 151, 152].

$$\delta(F) = \alpha(F - F_{th})^{\beta} \quad (44)$$

The damage probability curves follow a Poisson distribution as a function of both fluence dependent area or volumetric defect density and area or volume element, S, describing where the fluence is above the onset threshold.

$$P(F,S) = 1 - e^{(-\delta(F)*S)} \quad (45)$$

Equation 44 for the defect density has two terms, α and β, that are fitting coefficients to the damage probability curves using a least squares regression. Figure 78 shows an example of a measured probability curve and the least squares fitting to that data for an HfO_2 single layer tested in air. Figure 79 is the calculated defect density associated with this fit assuming the dominant heat loading is in the bulk of the material not at the surface.

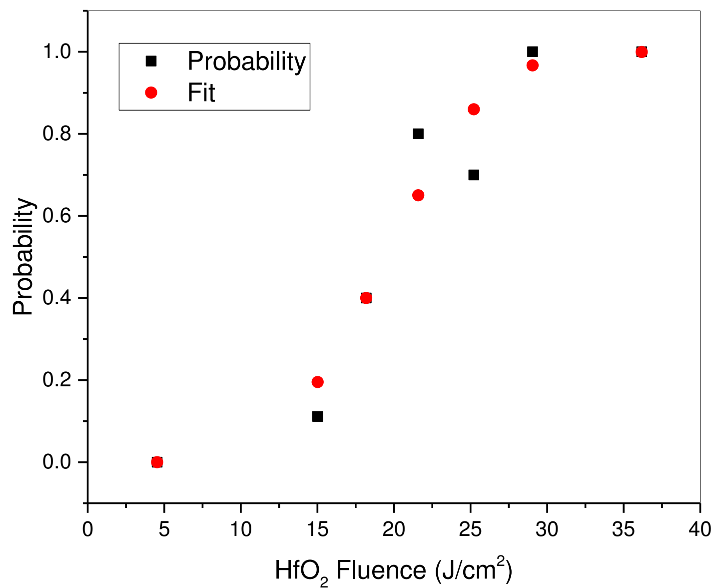

Figure 78: Example of damage probability curve and corresponding least squares fit for HfO_2 single layer.

Figures 80 and 79 are the calculated defect densities for each of the materials based on the most likely type of absorption, surface absorption (Figure 80) or bulk absorption (Figure 79) where HfO_2 is the only material assumed to have significant bulk absorption, determined from the discussions above.

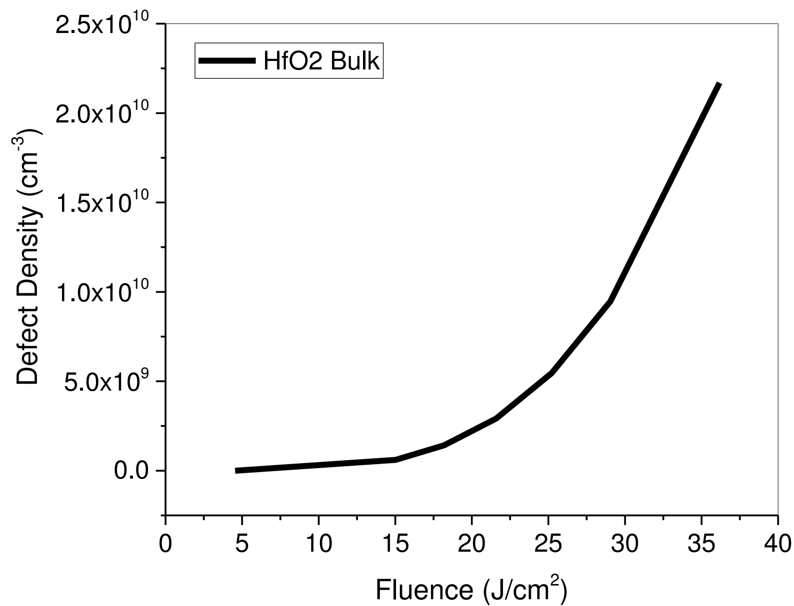

Figure 79: Corresponding defect density found using least squares fit of the damage probability curve for bulk absorption in HfO_2.

For in air testing of the base coat samples only the HfO_2 sample is likely to exhibit significant bulk absorption compared to its surface absorption. For this reason both the surface and bulk defect densities were plotted for this sample and no bulk defect densities were calculated for the other materials tested. Unfortunately, we are not able to conclusively determine which, either surface or bulk absorption, was ultimately responsible for the failure of HfO_2. In reality there were likely contributions from both. At threshold, all the defect densities we extract from the damage probability curves are very near zero by definition, so this number is of little practical use. More importantly to an understanding of these materials' laser damage response is the shape of the defect density curves as the fluence increases. The defect densities increase with fluence essentially turning on new absorbing defects as the fluence increases.

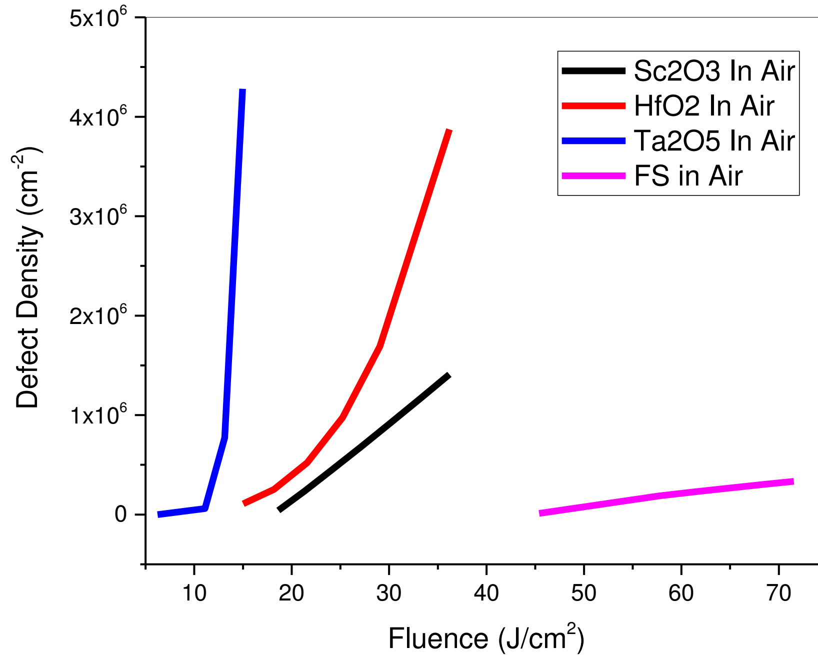

Figure 80: Surface defect densities for single layers tested in clean air.

The shape of this curve speaks to the susceptibility of the material to laser damage as well as the magnitude of the density of defects. As the fluence increases, a larger area is exposed to higher intensities increasing the number of potential defects in the illuminated area. Since the area and the number of defects increases at the same rate there should be no net increase in the defect density with intensity if only one type of defect exists and if their response is not intensity dependent. However, as shown in figures 79 and 80, there is indication that as fluence is increased new types of defects come into play contributing to damage. When making comparisons between different materials or between a material in two different environments, in air and in vacuum, an increasing defect density with fluence indicates an increased sensitivity to higher irradiances either in the form of additional defects in the same irradiated area or to

increased absorption within already absorbing defects. A reducing slope in the defect density indicates a saturating response for a class of defects with fluence.

In the case of bulk fused silica the defect densities are very low in comparison with the other materials tested. Near 47 J/cm^2 the material becomes sensitive to the laser and may be settling into a linearly increasing response with fluence (Figure 80). This defect type might be associated to relatively few, widely spaced relatively high absorbing surface imperfections perhaps left over from polishing efforts. In the case of Ta_2O_5, the nearly asymptotic nature of the defect density curve might suggest an intrinsic bulk defect. The HfO_2 defect densities calculated for both surface and bulk absorption describe a somewhat slowly increasing defect density which builds up from seed electrons originating from intrinsic point defects in the material and increases, likely via avalanche ionization, in a similar way as is typically assumed in free electron models of high band gap materials. The defect density curve for Sc_2O_3 appears to be linearly increasing with fluence and might suggest fewer additional absorption mechanisms come into play with increasing fluence. Once the defects are turned on at their threshold fluence these defect sites may not act to source seed electrons for other high order absorption mechanisms, such as avalanche ionization

The defect density curves for Sc_2O_3 with capping layers are shown in figure 81. The Sc_2O_3 base coat series displayed significantly different onset values that followed fairly well with the band gap of the topcoat material.. The major exception to this trend was in the case of the HfO_2 capped sample. As can be seen in the defect density curves for this series, the defect density remains relatively low compared with the HfO_2 series. For this to be the case the required absorption for this density of defects is much higher than in the other materials. Possible sources

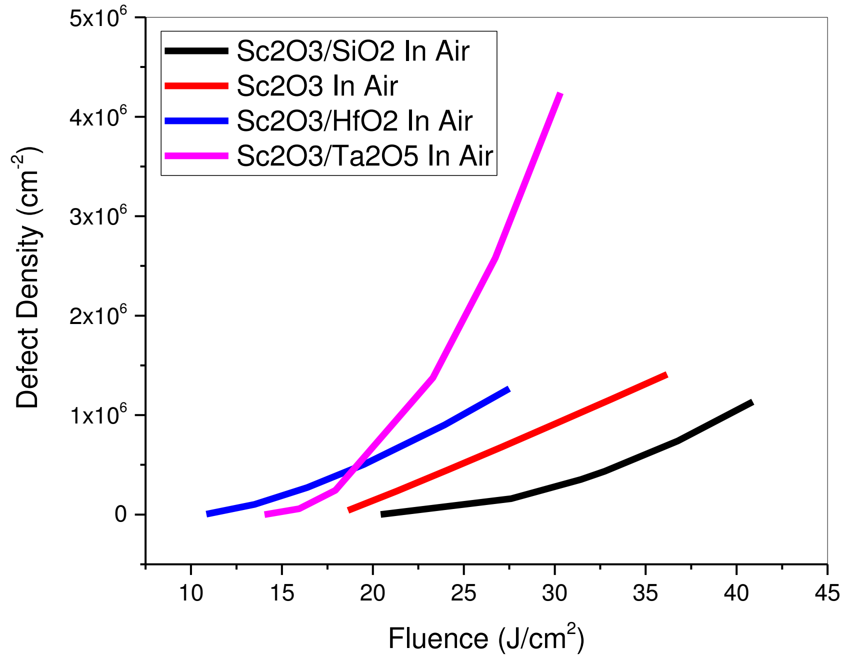

Figure 81: Surface defect densities for Sc_2O_3 basecoat with different capping layers tested in air

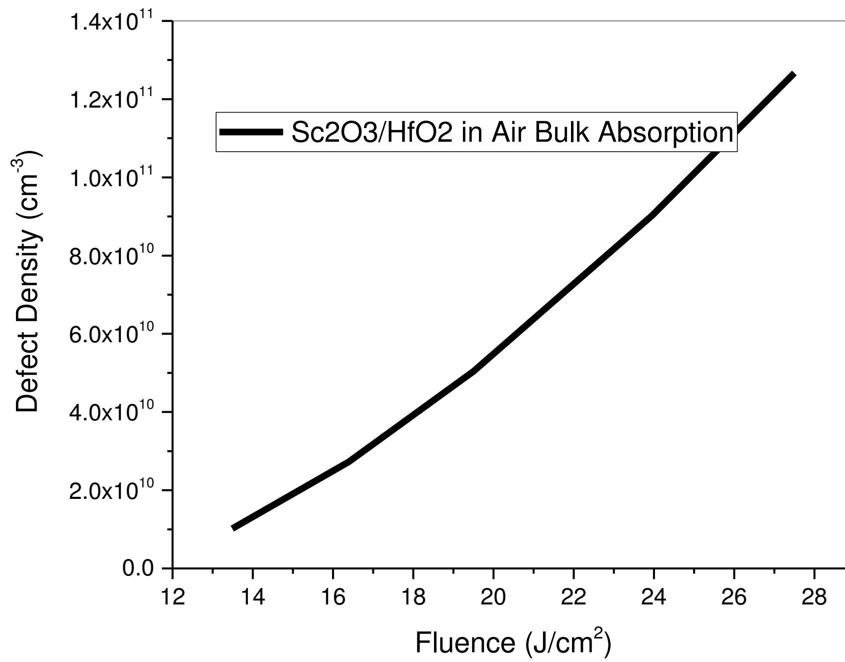

Figure 82: Volume defect densities for HfO_2 capped Sc_2O_3 basecoat series tested in air

of very high absorbing defects might be either physically large defects or metallic inclusions. The behavior of uncapped Sc_2O_3 has previously been discussed but the defect densities for SiO_2 and Ta_2O_5 capping layers are notably distinct from one another. While the silica capped base coat begins with a slowly increasing defect density, this happens at a much higher fluence than the other films tested. This defect density growth continues to increase in a very shallow exponential process. Contrasted against the silica's performance the Ta_2O_5 capping layer begins with a rapidly exponential increase at a relatively low fluence. The defect density calculations for this film appear to start rolling off with higher fluences. This very rapid increase in defect density just after threshold is more likely to be seen in very impure or intrinsically weak material.

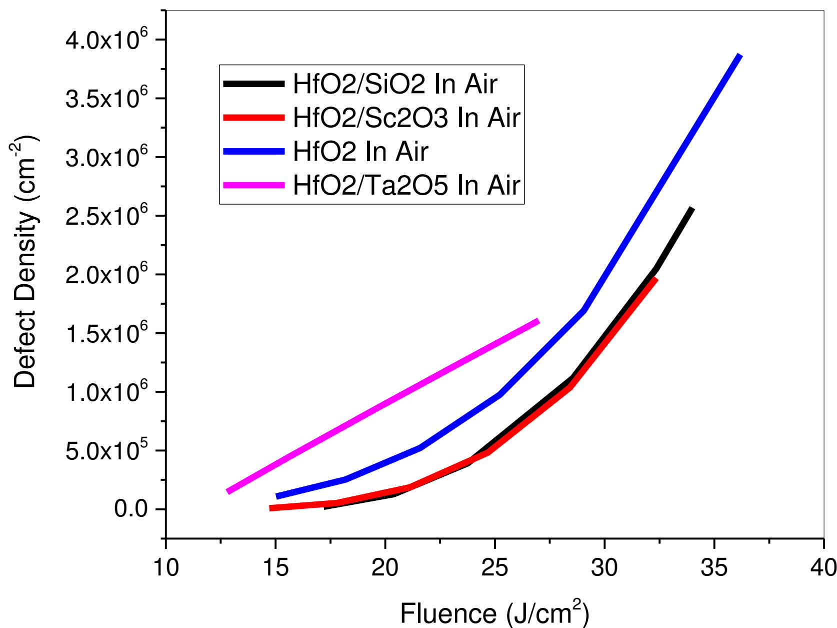

Figure 83: Surface defect densities for HfO_2 basecoat series tested in air

The defect densities for the HfO_2 basecoat series, shown in figure 83, all seem to follow

similar forms beginning with a slowly increasing density and then growing exponentially at higher fluences with the possible exception of the Ta_2O_5 capped sample. In the case of SiO_2 and Sc_2O_3 capped samples their defect density curves are nearly identical suggesting the performance of these two films may be dictated by the common basecoat and not the capping layers. The fact that the HfO_2 single layer has a higher defect density at a given fluence suggests the surface defect contribution of the SiO_2 and Sc_2O_3 capped samples is less than for an HfO_2 surface layer. The Ta_2O_5 capped sample appears to have a higher surface defect contribution which appears to be growing more slowly than the other samples with increasing fluence.

The defect density curves for the majority of our samples tested in vacuum are quite different from their in air values and their functional form. Figure 84 shows the calculated surface defect density of fused silica in air and vacuum. The surface defect density in vacuum starts out lower than in air for equivalent fluences but then grows much more quickly above ~63 J/cm^2. Above this threshold value a new surface defect is turned on and quickly dominates the performance of fused silica in vacuum. At lower fluences there may be some amount of vacuum mediated surface conditioning allowing for a slightly better damage onset performance than the in air values but in this case the effect is small.

The surface defect density of the single layers of Ta_2O_5, HfO_2 and Sc_2O_3 in air and in vacuum is shown in figure 85. The Ta_2O_5 and HfO_2 basecoat samples displayed very rapid increases in the surface defect density above threshold in vacuum. In vacuum the highest defect densities are seen in HfO_2 even though the turn on threshold for this material is higher than in the other two single layers tested. The defect density for Ta_2O_5 ramps up at a much lower threshold than in air and only seems to increase the rate of defect turn on with increasing fluence.

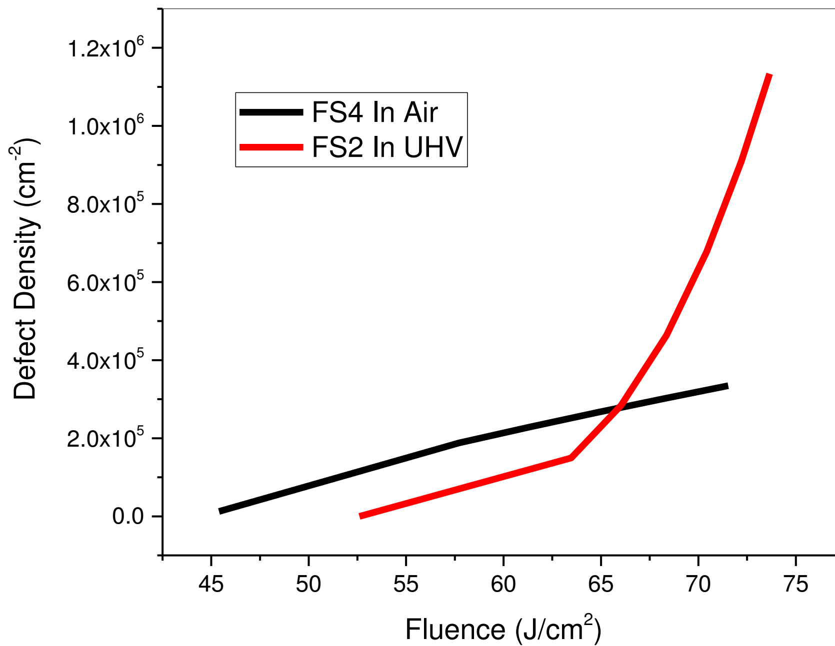

Figure 84: Surface defect densities for fused silica tested in air and vacuum.

Sc_2O_3 displays the largest deviation from its in air-to-vacuum performance in terms of its activation threshold, but the rate of defect creation, identified by the slope of the traces is similar in air and vacuum. We speculate these variations from their in air defect densities are due to vacuum and laser mediated surface defect creation.

Figure 86 shows defect surface densities for the Sc_2O_3 series with capping layers in air and in vacuum. The defect density in SiO_2 capped Sc_2O_3 is very similar both in air and in vacuum. HfO_2 capped Sc_2O_3 in vacuum demonstrated a very large increase in the onset LIDT fluence over its in air value. Once this fluence value was reached, however, the defect density climbed to a much higher value than was seen in air for similar fluences. This performance might suggest HfO_2 is still very sensitive to laser mediated surface defect creation in vacuum but the

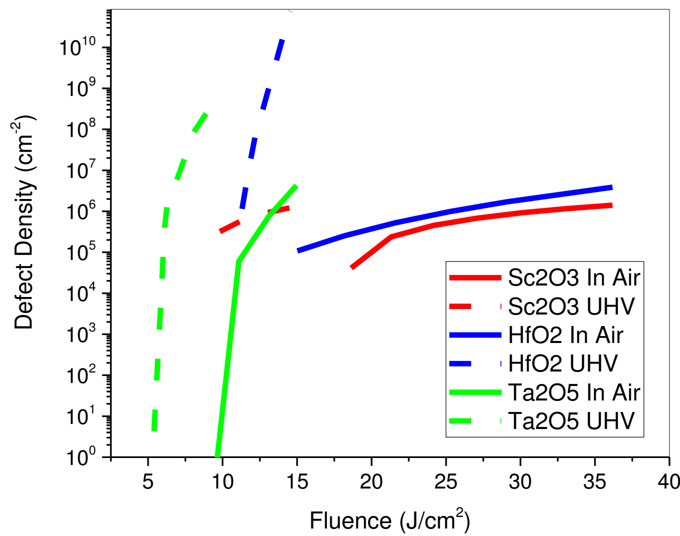

Figure 85: Surface defect densities for single layers tested in air and vacuum.

intrinsic material performance is complicated by a different defect type which can be at least partially passivated in vacuum, potentially through laser conditioning. The Ta_2O_5 capped sample tested in vacuum shows a decrease in the LIDT threshold but the rate of increase of defects with fluence is similar until ~$6*10^4$ defects/cm^2 where the in air sample displayed a saturation or depletion type effect that is not seen in vacuum until much later on.

Figure 87 shows the surface defect density for the HfO_2 samples. The number of data points in the case of the UHV SiO_2 capped HfO_2 were apparently not sufficient to show how similar the defect densities were for both in air and in UHV at lower fluences. However, the similarity is quite clear at all fluences where data is available for both samples. The defect density in the Ta_2O_5 capped sample is remarkable for how early those defects are turned on in vacuum and how high they climb. Even though the Sc_2O_3 capped sample showed similar damage performance in vacuum to the Ta_2O_5 sample the required absorption per defect site would necessarily be much larger in Sc_2O_3 than in Ta_2O_5.

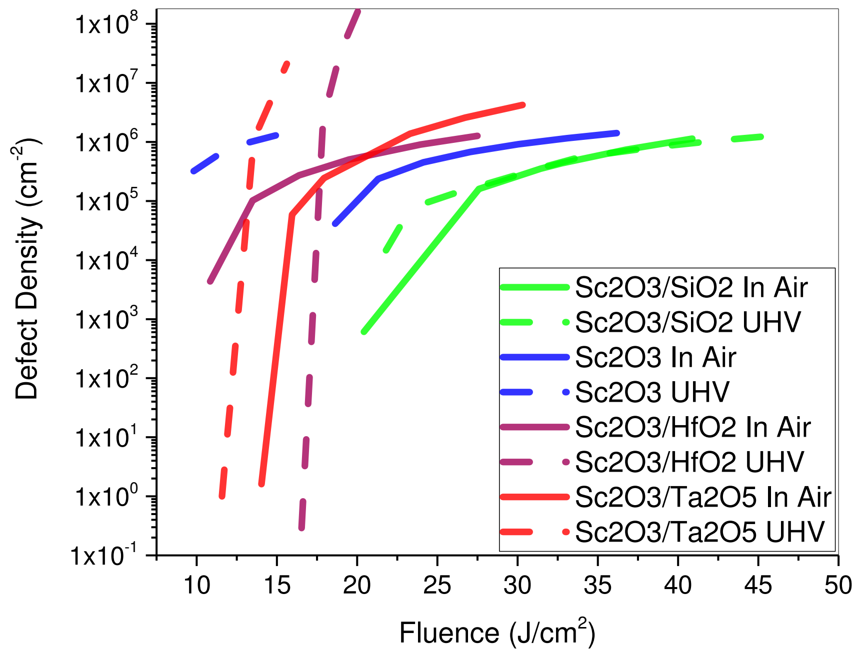

Figure 86: Surface defect densities for Sc_2O_3 basecoat series tested in air and vacuum

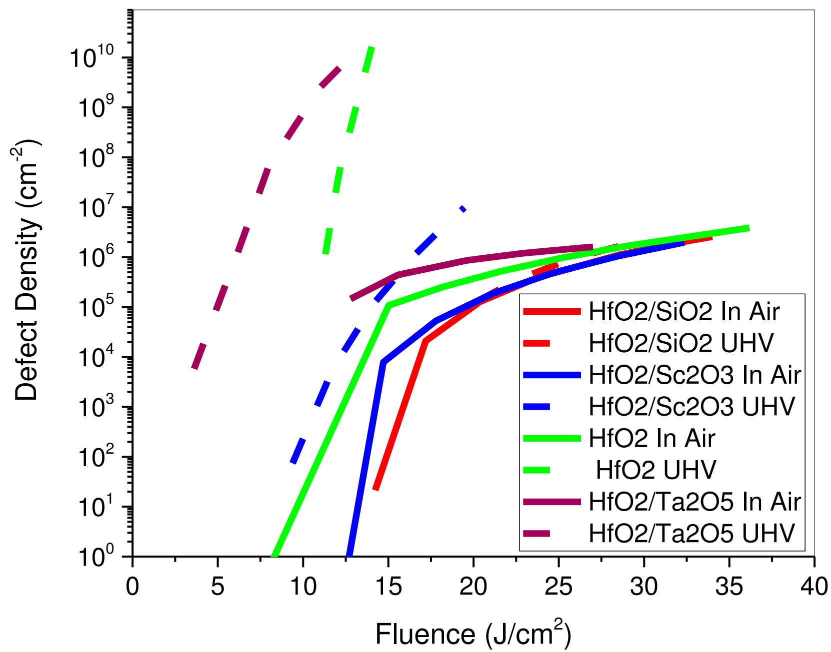

Figure 87: Surface defect densities for HfO_2 basecoat series tested in air and vacuum.

Conclusions

We carried out a detailed study of the laser damage behavior of HfO_2 and Sc_2O_3 thin films with and without capping layers at ambient and ultra-high vacuum conditions. We developed a controlled atmosphere test chamber capable of testing an optic's surface free from hydrocarbon contamination. The test apparatus is capable of scanning a laser beam across the test optic's surface for the purpose of probing the laser damage threshold both in a controlled atmosphere or in UHV. The level of vacuum can be monitored as well as the partial pressures of any gaseous species in the chamber from 0.5 – 300 amu.

The results of our single layer damage testing at 1030 nm and ~375 ps pulse duration showed the expected ranking for our three high index materials tested in air. The higher band gap Sc_2O_3 had the highest zero % probability LIDT value of 18 J/cm^2 followed by HfO_2 at 13 J/cm^2 with Ta_2O_5 having the lowest band gap as well as the lowest LIDT value of 10.9 J/cm^2. When these basecoat materials were capped with 10 nm thick capping layers composed of different metal oxides the observed LIDT ranking was significantly altered. In the case of the Sc_2O_3 basecoat series adding a thin layer of a higher band gap material improved the LIDT value by ~14% while adding a lower band gap capping layer reduced the LIDT value by ~42% for HfO_2 and ~20% for Ta_2O_5. The large decrease in the LIDT value for the HfO_2 capped Sc_2O_3 sample is explain by the likely presence of a high absorbing near surface defect in the HfO_2 capping layer which is primarily seen in our HfO_2 but may also exist to a lesser extent in the Ta_2O_5. This defect type could likely be a nanoscale absorbing defect having a physical extent of less than 10 nm.

In the case of the HfO_2 basecoat series tested in air the variation in the LIDT values with the addition of the 10 nm capping layers is less pronounced. Again, with the addition of a higher band gap capping layer the LIDT value increased from the uncapped HfO_2 about 10% for the

addition of both SiO_2 and Sc_2O_3. By adding a capping layer of Ta_2O_5 the LIDT performance decreased by about 10%.

When these single layers were tested in vacuum the expected decrease in the LIDT values for metal oxides was observed but the relative LIDT ranking for these films changed from the in air test results. Specifically, the Sc_2O_3 sample showed a decrease from 18 J/cm^2 to 8.5 J/cm^2 the largest decrease of the three materials tested. Ta_2O_5 decreased from 10.9 J/cm^2 in air to 4.9 J/cm^2 in vacuum the second largest change of the three single layers followed by HfO_2 which fell from 13 J/cm^2 in air to 9.2 J/cm^2 in vacuum. Curiously, HfO_2 showed the least susceptibility to laser mediated vacuum induced surface modification.

With the addition of an SiO_2 capping layer on these in vacuum tested Sc_2O_3 and HfO_2 basecoat samples we saw no change in the LIDT from their in air values. A very thin layer of SiO_2 is apparently capable of passivating the laser induced vacuum mediated defects in both basecoat materials. With the addition of an HfO_2 capping layer on Sc_2O_3 we see a major increase in the LIDT performance of this film pair from 10.5 J/cm^2 in air to over 16 J/cm^2 in vacuum. We have attributed this increase in the LIDT performance in vacuum to laser conditioning of the near surface defects previously seen in the in air testing of this film pair. We believe the reason these high absorbing defects do not negatively impact the in vacuum performance of this film pair while degrading the in air LIDT values is the lack of a barrier to surface expulsion of these defects when tested in vacuum. The atmosphere above the test optic's surface will impede any plasma ejected from the surface from moving away from the surface while this barrier is not present in the in vacuum tests. Near surface defects are capable of being driven off the surface without causing catastrophic damage to the film.

The Ta_2O_5 capped Sc_2O_3 sample tested in vacuum saw a moderate reduction in its LIDT value from the uncapped value from 14.5 J/cm^2 to 11.6 J/cm^2 in vacuum, a ~20% reduction. The Ta_2O_5 capped HfO_2 film pair showed a reduction greater than 50% from its in air value from 11.5 J/cm^2 to 4.3 J/cm^2 in vacuum. Finally, the Sc_2O_3 capped HfO_2 sample showed the largest decrease from its in air value of 14.5 J/cm^2 to 5.4 J/cm^2 in vacuum. This behavior is consistent with the in vacuum single layer testing we performed showing Sc_2O_3 is the most susceptible material to laser induced vacuum mediated surface defect creation.

Finally, we analyzed the actual damage probability curves measured in air and in vacuum to extract defect densities for the different materials we tested. The results of this work provide a clear ranking of the better surface metal oxide for use in the different environments we studied, in air and in vacuum. When working in air the higher band gap material, Sc_2O_3, greatly outperformed both HfO_2 and Ta_2O_5 single layers. Capping Sc_2O_3 with SiO_2 produced the highest LIDT material both in air and vacuum. Ta_2O_5 by contrast was the lowest performing material in terms of its LIDT in most of the material combinations used when tested in air. However, when working in vacuum the situation is somewhat different. In any case where Sc_2O_3 was exposed to vacuum the LIDT performance was severely compromised. Further, in contrast to its in air performance a HfO_2 capping layer grown on a high conductivity basecoat like Sc_2O_3 performed better than any other material combination except the SiO_2 capped samples. As already stated we believe this is the result of a laser conditioning process assisted by the high mean free paths available in vacuum. While Ta_2O_5 never performed particularly well as a single layer or as a capping layer in air its reduced performance in vacuum suggests this material should not be used as the first surface material in vacuum. Overall, we have demonstrated the ability of an

extremely thin surface layer, 10 nm, to significantly influence the behavior of a material in terms of its LIDT performance in vacuum.

CHAPTER VII. CONCLUSIONS AND FUTURE WORK

Our work at Colorado State University has given us a foundational understanding of how and what process parameters are most influential in producing low loss, high stability, high damage threshold metal oxide ion beam sputtered films. Ion beam sputtering is an ideal deposition method for films that will be used in harsh environments while having a high fluence requirement. This work has established the influence of oxygen incorporation in a multitude of metal oxides from both a mechanical, optical and laser damage perspective. This work led to the understanding that slightly too high of an oxygen partial pressure during deposition leads to excess oxygen incorporation in these materials leading to increased stress, increased absorption at one micron and 515nm, as well as to a reduced laser damage performance in both HfO_2 and Sc_2O_3.

Changes in the deposition energy were studied to inform us on the influence that small variation in the accelerating voltage in the main ion beam has on the development of optically sensitive defects in these films. The results of this work showed an increase from ~6 ppm to ~14 ppm in the optical absorption in Sc_2O_3 at 1064 nm with only a slight change in the LIDT performance of these films from ~18 J/cm^2 to ~15 J/cm^2 for a change of ~ 450 eV in the sputtering ion energy. These results suggest that either these defects are not strongly sensitive to the deposition energy, or at least to the ~400eV change in the deposition energy we studied, or that these defects are self-healing and not in fact a big problem for our specific deposition method. In the course of the beam voltage work, however, we noticed a strong correlation between the 532 nm absorption and the one micron LIDT performance of these same samples.

This may point to a more influential two photon absorption coefficient than was expected and this relationship should be studied further.

The cumulative work done at Colorado State University on the damage performance of HfO_2 and Sc_2O_3 ion beam sputtered thin films has advanced our understanding of the process conditions needed to grow lower loss, high damage threshold materials. We have improved the mechanical and optical properties of our high index materials such that we can grow single layers of HfO_2 and Sc_2O_3 at near theoretical densities and still be capable of operating in very high laser intensities without damaging.

We have also carried out studies of the LIDT performance of thin films of HfO_2 and Sc_2O_3 in air and in vacuum and investigated the impact of modifications to the interface on the LIDT performance of these films that occurred when adding capping layers. When investigating the influence of extremely thin topcoats on the LIDT performance of single layers we saw a remarkable influence on the performance of these films given the very little material that was used in the cap even when tested in air. While the materials followed a more or less expected band gap relationship when tested without capping layers the addition of just 10nm of capping material alters this natural ranking indicating other phenomena dominate the interaction.

Once the testing of these materials moved to a vacuum environment the situation became even more interesting. High conductivity metal oxides such as Sc_2O_3 that would be expected, and have been demonstrated, to outperform HfO_2 showed a remarkable reduction in its LIDT performance in vacuum. Given the direct comparisons that these data sets allowed us to make we were able to attribute much of the differences in the performance between in vacuum and in air testing to surface defect creation.

Our experimental results show that extremely thin layers of capping materials can radically alter the in vacuum damage performance of a given basecoat. SiO_2 capping layers markedly outperformed the other materials tested in our study. While it has been well known that SiO_2 is a good choice for capping films used in air it is noteworthy that just a few hundred atoms may be capable of altering a surface as well as much thicker layers. The SiO_2 capped samples, when tested in vacuum, did not show degradation in their LIDT for the number of pulses tested. Future testing should include higher pulse accumulation on these same film pairs. Somewhat surprising was the reduced vacuum performance of the higher band gap higher thermal conductivity Sc_2O_3 capping layers. The results of this work clearly demonstrate that just because a thin film performs well in one testing environment it may not do well in another.

Future Work

Further studies are needed to gain insight on the structural/morphological changes that occur at the interface of metal oxides and their impact on laser damage performance. Among these potentially informative experiments that could be carried out are two photon absorption measurements. We know from the linear absorption measurements made at 532nm that there exist in our films defects significantly more sensitive to this wavelength than to 1064nm. A good estimate of the two photon absorption cross section for these defects may significantly alter fitting parameters in the rate equation models that are used to predict damage[105].

As was mentioned early in the thesis, we have an interest in understanding the influence of UV assisted one micron absorption. The hardware necessary to perform LIDT experiments with the test optic having simultaneous exposure to 1030nm, 515nm and 257nm has been constructed. The doubling crystals were modeled in SNLO as well as by in house developed Matlab simulations to help optimize conversion from 1030nm to 515nm in KD*P and from

515nm to 257nm in KDP. Given the hydroscopic nature of these materials and the need to drop the temperature of the KDP crystal below freezing to phase match it was decided each crystal would be enclosed in a temperature stabilized controlled atmosphere environment. Custom heat sinks and kinematic mounts to facilitate temperature and angular tuning of these crystals were designed and manufactured. Simple tests on the conversion efficiency of the KD*P crystal were done without reaching the peak intensities required for optimal conversion and with no fine temperature tuning done. These results showed nearly 40% conversion to 515nm giving us high confidence that our simulations were correct. At the time of this writing, no LIDT tests with the presence of harmonics have been done yet. These series of tests are an obvious next step in giving us a more complete understanding of the optical performance of our thin films.

Another, longer term, set of experiments that would be invaluable would be to co-align a PCI measurement tool with a damaging laser in a vacuum environment that included either a high sensitivity RGA, ion trap or even a time of flight mass spectrometer. This tool might enable direct measurements of the damage initiating defects in our films.

The results of our work on thin capping layers were very interesting in both atmospheric testing as well as in vacuum. Significant material performance changes were seen with the inclusion of just 10nm of additional material grown on top of the basecoats. Referencing other overcoat work done using HfO_2 capping layers [44] there may be a size threshold below which a group of optically sensitive defects no longer exists. This size threshold, for HfO_2, may be in the range of 2–10 nm. While other deleterious factors may begin to dominate thin film structures of this size, namely mechanical integrity, it may be worth investigating even thinner capping layers of HfO_2 and Sc_2O_3 to see if further improvement in the in air and in vacuum LIDT performance can be realized.

BIBLIOGRAPHY

1. Mero, M., et al., *On the damage behavior of dielectric films when illuminated with multiple femtosecond laser pulses.* Optical Engineering, 2005. **44**(5): p. 051107.
2. Mero, M., et al., *Scaling laws of femtosecond laser pulse induced breakdown in oxide films.* Physical Review B, 2005. **71**(11): p. 115109.
3. Grosso, D. and P.A. Sermon, *Scandia optical coatings for application at 351 nm.* Thin Solid Films, 2000. **368**(1): p. 116-124.
4. Herrero, A.M., et al., *Epitaxial growth of Sc_2O_3 films on GaN.* Applied Physics Letters, 2006. **89**(9): p. 092117-092117-3.
5. *SPIE Laser Damage* 1968 - Present; Available from: http://spie.org/laser-damage.xml.
6. Langston, P.F., et al., *Point defects in Sc2O3 thin films by ion beam sputtering.* Applied Optics, 2014. **53**(4): p. A276-A280.
7. Menoni, C.S., *Advances in ion beam sputtered Sc2O3 for optical interference coatings.* SPIE Proceedings, 2010. **7842**.
8. *Veeco Ion Beam Sputtering*. Available from: http://www.veeco.com/products/ion-beam/deposition/spector.aspx.
9. *Veeco Planetary System*. Available from: http://www.veeco.com/products/ion-beam/deposition/spector-planetary.aspx.
10. Carr, C.W., H.B. Radousky, and S.G. Demos, *Wavelength Dependence of Laser-Induced Damage: Determining the Damage Initiation Mechanisms.* Physical Review Letters, 2003. **91**(12): p. 127402.
11. Jupé, M., et al., *Calculations and experimental demonstration of multi-photon absorption governing fs laser-induced damage in titania.* Opt. Express, 2009. **17**(15): p. 12269-12278.
12. Stuart, B.C., et al., *Optical ablation by high-power short-pulse lasers.* J. Opt. Soc. Am. B, 1996. **13**(2): p. 459-468.
13. Gattass, R.R. and E. Mazur, *Femtosecond laser micromachining in transparent materials.* Nat Photon, 2008. **2**(4): p. 219-225.
14. Chichkov, B.N., et al., *Femtosecond, picosecond and nanosecond laser ablation of solids.* Applied Physics A, 1996. **63**(2): p. 109-115.
15. Stuart, B.C., et al., *Nanosecond-to-femtosecond laser-induced breakdown in dielectrics.* Physical Review B, 1996. **53**(4): p. 1749.
16. Fu, X., et al., *Laser-induced damage in composites of scandium, hafnium, aluminum oxides with silicon oxide in the infrared.* Applied Optics, 2014. **53**(4): p. A392-A398.
17. Natoli, J.-Y., et al., *Laser-induced Damage of Materials in Bulk, Thin-film, and Liquid forms.* Applied Optics, 2002. **41**(16): p. 3156-3166.
18. Jensen, L., et al. *Damage threshold investigations of high-power laser optics under atmospheric and vacuum conditions*. 2006. SPIE.
19. Guenther, A.H. and J.K. McIver. *The Role Of Thermal Conductivity In The Pulsed Laser Damage Sensitivity Of Optical Thin Films+*. 1988.
20. Génin, F.Y., et al., *Role of light intensification by cracks in optical breakdown on surfaces.* Journal of the Optical Society of America A, 2001. **18**(10): p. 2607-2616.

21. Stenzel, E., et al., *Laser damage of alkaline-earth fluorides at 248 nm and the influence of polishing grades.* Applied Surface Science, 1997. **109–110**(0): p. 162-167.
22. Bloembergen, N., *Role of Cracks, Pores, and Absorbing Inclusions on Laser Induced Damage Threshold at Surfaces of Transparent Dielectrics.* Applied Optics, 1973. **12**(4): p. 661-664.
23. Hollands, E. and D.S. Campbell, *The mechanism of reactive sputtering.* Journal of Materials Science, 1968. **3**(5): p. 544-552.
24. Berg, S., et al., *Predicting thin-film stoichiometry in reactive sputtering.* Journal of Applied Physics, 1988. **63**(3): p. 887-891.
25. Pétigny, S., et al., *Superficial defects induced by argon and oxygen bombardments on (110) TiO2 surfaces.* Surface Science, 1998. **410**(2–3): p. 250-257.
26. Albers, T., et al., *Combined depth profile analysis with SNMS, SIMS and XPS: Preferential sputtering and oxygen transport in binary metal oxide multilayer systems.* Surface and Interface Analysis, 1994. **22**(1-12): p. 9-13.
27. Martin, P.J., *Ion-based methods for optical thin film deposition.* Journal of Materials Science, 1986. **21**(1): p. 1-25.
28. Thielsch, R., et al., *A comparative study of the UV optical and structural properties of SiO2, Al2O3, and HfO2 single layers deposited by reactive evaporation, ion-assisted deposition and plasma ion-assisted deposition.* Thin Solid Films, 2002. **410**(1-2): p. 86-93.
29. Wang, J., R.L. Maier, and H. Schreiber, *Crystal phase transition of HfO2 films evaporated by plasma-ion-assisted deposition.* Appl. Opt., 2008. **47**(13): p. C189-C192.
30. Papandrew, A.B., et al. *Laser conditioning characterization and damage threshold prediction of hafnia/silica multilayer mirrors by photothermal microscopy*. 2001.
31. Chen, G., *Size and Interface Effects on Thermal Conductivity of Superlattices and Periodic Thin-Film Structures.* Journal of Heat Transfer, 1997. **119**(2): p. 220-229.
32. Asheghi, M., et al., *Temperature-Dependent Thermal Conductivity of Single-Crystal Silicon Layers in SOI Substrates.* Journal of Heat Transfer, 1998. **120**(1): p. 30-36.
33. Becker, S., et al. *Laser-induced contamination of silica coatings in vacuum*. 2006.
34. Nguyen, D.N., et al., *Femtosecond pulse damage thresholds of dielectric coatings in vacuum.* Opt. Express, 2011. **19**(6): p. 5690-5697.
35. Harry, G.M., et al., *Titania-doped tantala/silica coatings for gravitational-wave detection.* Classical and Quantum Gravity, 2007. **24**(2): p. 405.
36. Pu, Y., et al., *Mechanism for atmosphere dependence of laser damage morphology in HfO2/SiO2 high reflective films.* Journal of Applied Physics, 2012. **112**(2): p. -.
37. Rainer, F., et al., *Materials for optical coatings in the ultraviolet.* Appl. Opt., 1985. **24**(4): p. 496-500.
38. Alvisi, M., et al., *Laser damage dependence on structural and optical properties of ion-assisted HfO2 thin films.* Thin Solid Films, 2001. **396**(1-2): p. 44-52.
39. Toldedano-Luque, M., et al., *Hafnium oxide thin films deposited by high pressure reactive sputtering in atmosphere formed with different Ar/O2 ratios.* Materials Science in Semiconductor Processing, 2006. **9**.
40. Prashant Raghua, et al., *Adsorption of Moisture and Organic Contaminants on Hafnium Oxide, Zirconium Oxide, and Silicon Oxide Gate Dielectrics.* 2003.
41. Robertson, J.X., Ka. *Defect energy levels in HfO2*. 2006.

42. Gavartin, J.L., et al., *Negative oxygen vacancies in HfO2 as charge traps in high-k stacks.* Applied Physics Letters, 2006. **89**.
43. Papernov, S., et al., *Near-ultraviolet absorption and nanosecond-pulse-laser damage in HfO2 monolayers studied by submicrometer-resolution photothermal heterodyne imaging and atomic force microscopy.* Journal of Applied Physics, 2011. **109**(11): p. -.
44. Strzhemechny, Y.M., et al., *Low energy electron-excited nanoscale luminescence spectroscopy studies of intrinsic defects in HfO2 and SiO2-HfO2-SiO2-Si stacks.* Journal of Vacuum Science Technology B, 2008. **26**(1).
45. Reichling, M., A. Bodemann, and N. Kaiser, *Defect induced laser damage in oxide multilayer coatings for 248 nm.* Thin Solid Films, 1998. **320**(2): p. 264-279.
46. Foster, A.S., et al., *Vacancy and interstitial defects in hafnia.* Physical Review B, 2002. **65**(17): p. 174117.
47. Heitmann, W., *Reactively Evaporated Films of Scandia and Yttria.* Applied Optics, 1973. **12**(2): p. 394-397.
48. Xu, Z., A. Daga, and H. Chen, *Microstructure and optical properties of scandium oxide thin films prepared by metalorganic chemical-vapor deposition.* Applied Physics Letters, 2001. **79**(23): p. 3782-3784.
49. Liu, G., et al., *Effect of substrate temperatures on the optical properties of evaporated Sc2O3 thin films.* Thin Solid Films, 2010. **518**(10): p. 2920-2923.
50. Al-Kuhaili, M.F., *Optical properties of scandium oxide films prepared by electron beam evaporation.* Thin Solid Films, 2003. **426**(1–2): p. 178-185.
51. Liu, C., et al., *Epitaxial growth of* Sc_2O_3 *films on GaN (0001) by pulsed laser deposition.* Journal of Vacuum Science & Technology B: Microelectronics and Nanometer Structures, 2007. **25**(3): p. 754-759.
52. de Rouffignac, P., et al., *ALD of Scandium Oxide from Scandium Tris(N,N[sup Ê*^{1}*]-diisopropylacetamidinate) and Water.* Electrochemical and solid-state letters, 2006. **9**(6): p. F45.
53. Vink, T.J., et al., *Physically trapped oxygen in sputter-deposited MoO[sub 3] films.* Journal of Applied Physics, 2000. **87**(10): p. 7252-7254.
54. Pérez-Pacheco, A., et al., *Influence of the growth conditions on the stoichiometry and on the optical properties of titanium oxide thin films prepared by reactive sputtering.* Thin Solid Films, 2009. **517**(18): p. 5415-5418.
55. Mende, M., et al., *Laser damage resistance of ion-beam sputtered Sc2O3/SiO2 mixture optical coatings.* Applied Optics, 2013. **52**(7): p. 1368-1376.
56. Gallais, L., et al. *An exhaustive study of laser damage in ion beam sputtered pure and mixture oxide thin films at 1030 nm with 500 fs pulse durations*. 2012.
57. C. R. Wolfe, M.R.K., J. H. Campbell, F. Rainer, A. J. Morgan, and R. P Gonzales, *Laser Conditioning of Optical Thin Films.* 1990.
58. Ling, X., et al., *Annealing effect on the laser-induced damage resistance of ZrO2 films in vacuum.* Applied Optics, 2009. **48**(29): p. 5459-5463.
59. Hosono, H., et al., *Physical Disorder and Optical Properties in the Vacuum Ultraviolet Region of Amorphous* SiO_2*.* Physical Review Letters, 2001. **87**(17): p. 175501.
60. Riede, W., et al. *Analysis of the air-vacuum effect in dielectric coatings*. 2008.
61. A. M. Muller, C.J.G.J.U., B. Witzel, J. Wanner, K. L. Kompa, *Photoionization and photofragmentation of gaseous toluene using 80-fs, 800-nm laser pulses.* Journal of Chemical Physics, 2000. **112**.

62. Riede, W., et al. *Laser-induced hydrocarbon contamination in vacuum*. 2005.
63. Cui, Y., et al., *Impact of organic contamination on laser-induced damage threshold of high reflectance coatings in vacuum.* Applied Surface Science, 2008. **254**(18): p. 5990-5993.
64. R. R. Kunz, V.L.a.D.K.D., *Experimentation and modeling of organic photocontamination on lithographic optics.* 2000.
65. *Silicon-oxygen bond arrangement*. Available from: http://www.chem.ox.ac.uk/vrchemistry/chapter6/Page21.htm.
66. *Quartz Crystal Structure*. Available from: httpsimages.search.yahoo.comimagesview;_ylt=AwrTcYR_qVpVXaAA7S0unIlQ;_ylu=X3oDMTIycXZkbm1tBHNlYwNzcgRzbGsDaW1nBG9pZAM2ZTUzMjRjMTk0NmNiZjM3YmEzZjIzZmYwYzBmYTQyMgRncG9zAzgEaXQDYmluZw--.origin=&back=https%3A.
67. *Amorphous SiO2 on Si*. Available from: httpsimages.search.yahoo.comimagesview;_ylt=AwrB8pr7XVlVXS8AL6sunIlQ;_ylu=X3oDMTI0aGIwOHVrBHNlYwNzcgRzbGsDaW1nBG9pZANlZTY1NGU3YjdhOGIzNjZiZGNiODYwZDlhMTdhN2NmZQRncG9zAzE2MgRpdANia.
68. George, S.R., et al., *Interaction of vacuum ultraviolet excimer laser radiation with fused silica. I. Positive ion emission.* Journal of Applied Physics, 2010. **107**(3): p. 033107.
69. Chow, R., et al. *Reversible laser damage of dichroic coatings in a high-average-power laser vacuum resonator*. 2000.
70. Bei, C., et al., *Influence of oxygen diffusion through capping layers of low work function metal gate electrodes.* Electron Device Letters, IEEE, 2006. **27**(4): p. 228-230.
71. Chatham, H., *Oxygen diffusion barrier properties of transparent oxide coatings on polymeric substrates.* Surface and Coatings Technology, 1996. **78**(1–3): p. 1-9.
72. He, J.Q., et al., *Microstructure and interfaces of HfO2 thin films grown on silicon substrates.* Journal of Crystal Growth, 2004. **262**.
73. Yang, Y., H. Liu, and P. Zhang, *Structural and electronic properties of Sc n O m (n= 1− 3, m= 1− 2 n) clusters: Theoretical study using screened hybrid density functional theory.* Physical Review B, 2011. **84**(20): p. 205430.
74. Schaub, R., et al., *Oxygen-Mediated Diffusion of Oxygen Vacancies on the TiO2(110) Surface.* Science Magazine, 2003. **299**.
75. Arun Kumar, D.R., and D. L.Douglass, *Effect of oxide defect structure on the electrical properties of ZrO2.* Journal of the American Ceramic Society, 1972.
76. W.W.Smeltzer, D.J.P.a., *Oxygen Diffusion in Monoclinic Zirconia.* Journal Electrochemical Society: Solid State Science, 1970. **117**(3).
77. Yu, H.Y., et al., *Thermal stability of (HfO2)x(Al2O3)1-x on Si.* Applied Physics Letters, 2002. **81**(19).
78. Guo, W., et al., *Epitaxial ZnO films on (111) Si substrates with Sc2O3 buffer layers.* Applied Physics Letters, 2009. **94**(12): p. 122107-122107-3.
79. Mitchell, D.F., G.I. Sproule, and M.J. Graham, *Sputter reduction of oxides by ion bombardment during Auger depth profile analysis.* Surface and Interface Analysis, 1990. **15**(8): p. 487-497.
80. Oliver, J.B., *Evaporated HfO2/SiO2 Optical Coatings and Modifications for High-Power Laser Applications*, 2012.

81. John A. Kardach, A.F.S., Arthur H Guenther and John K. McIver, *Photo Induced Desorption and Emission from Thin Film Dielectric Sufaces.* 1987.
82. Lange, M.R., J. McIver, and A.H. Guenther. *Laser damage threshold predictions based on the effects of thermal and optical properties employing a spherical impurity model*. in *Proc. SPIE*. 1985.
83. Ling, X., et al., *Damage investigations of AR coating under atmospheric and vacuum conditions.* Optics & Laser Technology, 2009. **41**(7): p. 857-861.
84. Tamura, S., et al., *Measurement of Laser Damage Threshold of 355-nm Antireflection Coating.* Japanese Journal of Applied Physics, 1989. **28**(6R): p. 1141.
85. Tamura, S., et al., *Influence of Deposition Parameters on Laser Damage Threshold of 355-nm Scandium Oxide-Magnesium Fluoride High-Reflector Coatings.* Japanese Journal of Applied Physics, 1990. **29**(10R): p. 1960.
86. Strupp, P.G., P.C. Stair, and E. Weitz, *Pulsed laser‐induced electron and positive‐ion emission from Cu(100) under ultrahigh‐vacuum conditions near the threshold for surface damage.* Journal of Applied Physics, 1991. **69**(6): p. 3472-3479.
87. Rainer, F., et al., *Scandium oxide coatings for high-power UV laser applications.* Appl. Opt., 1982. **21**(20): p. 3685-3688.
88. Trudy Tuttle Hart, T.L.L.a.C.K.C., *Effects of Undercoats and Overcoats on Damage Thresholds of 248 nm Coatings.* 1983.
89. Tamura, S., *Laser damage threshold of Sc2O3/SiO2 high reflection coatings for a laser wavelength of 355 nm.*
90. Carniglia, C.K., *Oxide coatings for one micrometer laser fusion systems.* Thin Solid Films, 1981. **77**(1–3): p. 225-238.
91. Stolz, C.J., et al. *Effect of SiO2 overcoat thickness on laser damage morphology of HfO2/SiO2 Brewster's angle polarizers at 1064 nm*. 1997.
92. Zhan, M., et al., *Overcoat dependence of laser-induced damage threshold of 355 nm HR coatings.* Applied Surface Science, 2006. **252**(6): p. 2126-2130.
93. Wu, Z., et al. *Understanding of the abnormal wavelength effect of overcoats*. 1991.
94. Yao, J.F., Zhengxiu; He, Hongbo; Shao, Jianda, *Influence of overcoat on laser-induced damage threshold of 532 and 800nm TiO2/SiO2 high reflectors.* 2007.
95. Schmid, S.P.a.A.W., *Localized absorption effects during 351nm, pulsed laser irradiation of dielectric multilayer thin films.* J. Appl. Phys, 1997.
96. Tollerud, J., *SCATTER LOSS AND SURFACE ROUGHNESS OF HAFNIUM OXIDE THIN FILMS.* 2011.
97. Milam, D., et al., *Influence of deposition parameters on laser-damage threshold of silica?tantala AR coatings.* Applied Optics, 1982. **21**(20): p. 3689-3694.
98. *Network Covalent Materials*. Available from: http//www.meta-synthesis.comwebbook38_laingtetrahedra.
99. G. D. Wilk, R.M.W., and J. M. Anthony, *High-κ gate dielectrics: Current status and materials properties considerations.* Journal of Applied Physics, 2001.
100. *Light at an interface*. Available from: http://hyperphysics.phy-astr.gsu.edu/hbase/phyopt/reflin.html.
101. *Phase shift at an interface*. Available from: http://physics.ucsd.edu/students/courses/spring2009/physics2c/documents/6.1ThinFilmInterference..pdf.

102. Macleod, H.A., *Thin Film Optical Filters*. Fourth ed2010, Boca Raton, London, New York: CRC Press.
103. *Specular vs diffuse reflections*. Available from: http://www.azom.com/article.aspx?ArticleID=4781.
104. *Idealized vs practical band gap*. Available from: http://commons.wikimedia.org/wiki/File:Band_gap.gif.
105. Emmert, L.A., M. Mero, and W. Rudolph, *Modeling the effect of native and laser-induced states on the dielectric breakdown of wide band gap optical materials by multiple subpicosecond laser pulses.* Journal of Applied Physics, 2010. **108**(4): p. 043523-7.
106. Emmert, L.A., et al. *Femtosecond pulse S on 1 LIDT in dielectric materials: comparison of experiment and theory*. 2010. Boulder, Colorado, USA: SPIE.
107. Wolfe, C., et al., *Laser conditioning of optical thin films.* Laser induced damage in optical materials, 1989. **1**: p. 989.
108. Krous, E., *CHARACTERIZATION OF SCANDIUM OXIDE THIN FILMS FOR USE IN INTERFERENCE COATINGS FOR HIGH-POWER LASERS OPERATING IN THE NEAR-INFRARED.* 2010.
109. Alexey Kondyurin, M.M., *Ion Beam Treatment of Polymers Applicaion Aspects from Medicine to Space*2007.
110. Nyberg, S.B.a.T., *Fundamental understanding and modeling of reactive sputtering processes.* Thin Solid Films, 2005.
111. *Diagram of Woollam ellipsometer operation*. Available from: http://www.jawoollam.com/tutorial_4.html.
112. *Tutorial of JA Woollam ellipsometer operation*. Available from: http://www.jawoollam.com/tutorial_1.html.
113. Chang, R., et al., *Residual stresses of sputtering titanium thin films at various substrate temperatures.* Journal of nanoscience and nanotechnology, 2010. **10**(7): p. 4562-4567.
114. Route, A.A.M.F.A.M.R., *Photothermal common-path interferometry (PCI): new developments.* SPIE Proceedings, 2009. **7193**.
115. Tollerud, J., *Scatter Loss and Surface Roughness of Hafnium Oxide Thin Films*, 2011, Colorado State University.
116. Tullin*, L.-E.Å.a.C.J., *The Theory Behind FTIR analysis Application Examples From Measurement at the 12 MW Circulating Fluidized Bed Boiler at Chalmers.*
117. *AFM explanatory diagram*. Available from: http://www.keysight.com/main/editorial.jspx?ckey=1774141&id=1774141&nid=-33986.0&lc=spa&cc=VE.
118. *XRD Bragg diffraction*. Available from: http://en.wikipedia.org/wiki/File:Bragg_diffraction_2.svg.
119. *Mechanisms to strain broaden an XRD peak*. Available from: http://pd.chem.ucl.ac.uk/pdnn/peaks/size.htm.
120. Barklie, R. and S. Wright, *Electron paramagnetic resonance characterization of defects in HfO2 and ZrO2 powders and films.* Journal of Vacuum Science & Technology B, 2009. **27**(1): p. 317-320.
121. *Zeeman split of one energy level*. Available from: http://en.wikipedia.org/wiki/Electron_paramagnetic_resonance.

122. *Diagram of an EPR cavity, magnet and support equipment*. Available from: https://www.auburn.edu/~duinedu/epr/1_theory.pdf.
123. *Evactron Plasma Cleaning by XEI Scientific*. Available from: http://www.evactron.com/.
124. X. Wang, O.I.S., B.Xi, X. Lou, R.J.Molnar, T. Palacios, and R.G. Gordon, *Atomic Layer Deposition Sc203 for Passivating AlGaN/GaN High Electron Mobility Transistor Devices.* Applied Physics Letters, 2012.
125. Yakovkina, L.V., et al., *Synthesis and properties of dielectric (HfO2)1 − x (Sc2O3) x films.* Inorganic Materials, 2013. **49**(2): p. 172-178.
126. Menoni, C.S., et al. *What role do defects play in the laser damage behavior of metal oxides?* 2012.
127. Flinn, P.A., D.S. Gardner, and W.D. Nix, *Measurement and Interpretation of stress in aluminum-based metallization as a function of thermal history.* IEEE Transactions on Electron Devices, 1987. **34**(3): p. 689-699.
128. Stoll, S. and A. Schweiger, *EasySpin, a comprehensive software package for spectral simulation and analysis in EPR.* Journal of Magnetic Resonance, 2006. **178**(1): p. 42-55.
129. Wright, S. and R.C. Barklie, *Electron paramagnetic resonance characterization of defects in monoclinic HfO[sub 2] and ZrO[sub 2] powders.* Journal of Applied Physics, 2009. **106**(10): p. 103917.
130. Markosyan, A.S., et al., *Study of spontaneous and induced absorption in amorphous Ta2O5 and SiO2 dielectric thin films.* Journal of Applied Physics, 2013. **113**(13): p. 133104.
131. Kay, E., F. Parmigiani, and W. Parrish, *Effect of energetic neutralized noble gas ions on the structure of ion beam sputtered thin metal films.* Journal of Vacuum Science & Technology A, 1987. **5**(1): p. 44-51.
132. Barybin, A.A. and V.I. Shapovalov, *Nonisothermal chemical model of reactive sputtering.* Journal of Applied Physics, 2007. **101**(5): p. 054905.
133. Berg, S. and T. Nyberg, *Fundamental understanding and modeling of reactive sputtering processes.* Thin Solid Films, 2005. **476**(2): p. 215-230.
134. Langdon, B., et al. *Influence of process conditions on the optical properties HfO2/SiO2 thin films for high power laser coatings*. 2007.
135. Markosyan, A., *Thin Film Absorption Under Two Color Illumination.* TBD, 2012.
136. Becker, S., et al. *Laser-induced contamination of silica coatings in vacuum*. in *Boulder Damage Symposium XXXVIII: Annual Symposium on Optical Materials for High Power Lasers*. 2006. International Society for Optics and Photonics.
137. Trap, B.A.I.; Available from: http://www.vacuumone.com/pdf/VacuumOne_835VQM.pdf.
138. Alessi, D.A., et al., *Picosecond laser damage performance assessment of multilayer dielectric gratings in vacuum.* Optics Express, 2015. **23**(12): p. 15532-15544.
139. Furch, F.J., et al., *Demonstration of an all-diode-pumped soft x-ray laser.* Opt. Lett., 2009. **34**(21): p. 3352-3354.
140. Curtis, A.H., et al. *Demonstration of soft X-ray laser driven by an all diode pumped CPA laser system*. in *IEEE Photonics Society, 2010 23rd Annual Meeting of the*. 2010.
141. Stuart, B.C., et al., *Laser-Induced Damage in Dielectrics with Nanosecond to Subpicosecond Pulses.* Physical Review Letters, 1995. **74**(12): p. 2248-2251.
142. Marburger, J.H., *Self-focusing: Theory.* Progress in Quantum Electronics, 1975. **4**: p. 35-110.

143. Smith, A.V. and B.T. Do, *Bulk and surface laser damage of silica by picosecond and nanosecond pulses at 1064 nm.* Applied Optics, 2008. **47**(26): p. 4812-4832.
144. Papernov, S. and A. Schmid, *Localized absorption effects during 351 nm, pulsed laser irradiation of dielectric multilayer thin films.* Journal of Applied Physics, 1997. **82**(11): p. 5422-5432.
145. Emmert, L.A., et al. *The Role of Native and Transient Laser-Induced Defects in the Femtosecond Breakdown of Dielectric Films*. in *Conference on Lasers and Electro-Optics/International Quantum Electronics Conference*. 2009. Baltimore, Maryland: Optical Society of America.
146. Yamada, K., et al., *Degradation and restoration of dielectric-coated cavity mirrors in the NIJI-IV FEL.* Nuclear Instruments and Methods in Physics Research Section A: Accelerators, Spectrometers, Detectors and Associated Equipment, 1995. **358**(1): p. 392-395.
147. Kunz, R.R., V. Liberman, and D.K. Downs, *Experimentation and modeling of organic photocontamination on lithographic optics.* Journal of Vacuum Science & Technology B, 2000. **18**(3): p. 1306-1313.
148. Jensen, L., et al. *Damage threshold investigations of high-power laser optics under atmospheric and vacuum conditions*. in *Boulder Damage Symposium XXXVIII: Annual Symposium on Optical Materials for High Power Lasers*. 2006. International Society for Optics and Photonics.
149. Stolz, C.J., et al. *Laser conditioning methods of hafnia-silica multilayer mirrors*. in *Laser-Induced Damage in Optical Materials: 1998*. 1999. International Society for Optics and Photonics.
150. A. B. Papandrew, C.J.S., Z. L. Wu, G. E. Loomis, and S. Falabella, *Laser conditioning characterization and damage threshold prediction of hafnia/silica multilayer mirrors by photothermal microscopy.* Proceedings of SPIE - The International Society For Opitcal Engineering, 2000.
151. Fu, X., et al., *Investigation of the distribution of laser damage precursors at 1064 nm, 12 ns on Niobia-Silica and Zirconia-Silica mixtures.* Optics Express, 2012. **20**(23): p. 26089-26098.
152. Gallais, L., et al., *Investigation of nanodefect properties in optical coatings by coupling measured and simulated laser damage statistics.* Journal of Applied Physics, 2008. **104**(5): p. 053120.

APPENDIX

Damage performance of ion beam sputtered Sc_2O_3 and HfO_2 single layers tested in air and ultra-high vacuum

Author List

P. F. Langston, D. Patel, B. Reagan, J.J. Rocca, and C.S. Menoni

Abstract

Results of a study of laser induced damage of ion beam sputtered single layers and capped single layers of Sc_2O_3, HfO_2 and Ta_2O_5 in a controlled atmosphere and in an ultra-high vacuum (UHV) environment are presented. All damage testing was done using a 100-on-1 test at a wavelength of 1.030 μm using a ~375 ps pulse duration and a ~100 μm FWHM spot size. The zero percent probability laser induced damage threshold (LIDT) of Ta_2O_5, HfO_2 and Sc_2O_5 were determined to be 10.9, 13 and 18 J/cm^2 respectively when tested in a controlled air atmosphere. The threshold values measured in UHV were 8.5 J/cm^2 for Sc_2O_3, 9.2 J/cm^2 for HfO_2 and 4.9 J/cm^2 for Ta_2O_5. Addition of a 10 nm ultra-thin capping layer of SiO_2, Sc_2O_3, HfO_2 and Ta_2O_5 to the basecoat films of Sc_2O_3 and HfO_2 significantly changes the LIDT, suggesting that the surface states play a dominant role in the laser damage behavior of the structures. The trend in LIDT observed in the single and capped Sc_2O_3 and HfO_2 layers suggests that when designing interference coatings for $\lambda \sim 1$ μm operation Sc_2O_3 is a better choice for high index material when the coatings are used at atmospheric conditions. HfO_2 performs better at ultra-high vacuum conditions.

References and links

1. S. Becker, A. Pereira, P. Bouchut, F. Geffraye, and C. Anglade, "Laser-induced contamination of silica coatings in vacuum," in *Boulder Damage Symposium XXXVIII:*

Annual Symposium on Optical Materials for High Power Lasers (International Society for Optics and Photonics (2006), pp. 64030J-64030J-64012.

2. D. N. Nguyen, L. A. Emmert, P. Schwoebel, D. Patel, C. S. Menoni, M. Shinn, and W. Rudolph, "Femtosecond pulse damage thresholds of dielectric coatings in vacuum," Opt. Express **19**, 5690-5697 (2011).
3. Y. Pu, P. Ma, S. Chen, J. Zhu, G. Wang, F. Pan, P. Sun, X. Zhu, J. Zhu, and D. Xiao, "Mechanism for atmosphere dependence of laser damage morphology in HfO2/SiO2 high reflective films," Journal of Applied Physics **112**, - (2012).
4. X. Ling, S. Li, M. Zhou, X. Liu, Y. Zhao, J. Shao, and Z. Fan, "Annealing effect on the laser-induced damage resistance of ZrO2 films in vacuum," Applied Optics **48**, 5459-5463 (2009).
5. H. Hosono, Y. Ikuta, T. Kinoshita, K. Kajihara, and M. Hirano, "Physical Disorder and Optical Properties in the Vacuum Ultraviolet Region of Amorphous SiO_2," Physical Review Letters **87**, 175501 (2001).
6. W. Riede, P. Allenspacher, L. Jensen, and M. Jupé, "Analysis of the air-vacuum effect in dielectric coatings," (2008), pp. 71320F-71320F-71310.
7. V. L. a. D. K. D. R. R. Kunz, "Experimentation and modeling of organic photocontamination on lithographic optics," (2000).
8. S. R. George, J. A. Leraas, S. C. Langford, and J. T. Dickinson, "Interaction of vacuum ultraviolet excimer laser radiation with fused silica. I. Positive ion emission," Journal of Applied Physics **107**, 033107 (2010).
9. X. Ling, Y. Zhao, D. Li, J. Shao, and Z. Fan, "Damage investigations of AR coating under atmospheric and vacuum conditions," Optics & Laser Technology **41**, 857-861 (2009).
10. P. G. Strupp, P. C. Stair, and E. Weitz, "Pulsed laser-induced electron and positive-ion emission from Cu(100) under ultrahigh-vacuum conditions near the threshold for surface damage," Journal of Applied Physics **69**, 3472-3479 (1991).
11. P. F. Langston, E. Krous, D. Schiltz, D. Patel, L. Emmert, A. Markosyan, B. Reagan, K. Wernsing, Y. Xu, Z. Sun, R. Route, M. M. Fejer, J. J. Rocca, W. Rudolph, and C. S. Menoni, "Point defects in Sc2O3 thin films by ion beam sputtering," Applied Optics **53**, A276-A280 (2014).
12. A. A. M. F. A. M. R. Route, "Photothermal common-path interferometry (PCI): new developments," SPIE Proceedings **7193** (2009).
13. "Evactron Plasma Cleaning by XEI Scientific," http://www.evactron.com/.
14. B. A. I. Trap, http://www.vacuumone.com/pdf/VacuumOne_835VQM.pdf.
15. D. A. Alessi, C. W. Carr, R. P. Hackel, R. A. Negres, K. Stanion, J. E. Fair, D. A. Cross, J. Nissen, R. Luthi, G. Guss, J. A. Britten, W. H. Gourdin, and C. Haefner, "Picosecond laser damage performance assessment of multilayer dielectric gratings in vacuum," Optics Express **23**, 15532-15544 (2015).
16. A. H. Curtis, B. A. Reagan, K. A. Wernsing, F. J. Furch, B. M. Luther, and J. J. Rocca, "Demonstration of a compact 100 Hz, 0.1 J, diode-pumped picosecond laser," Opt. Lett. **36**, 2164-2166 (2011).
17. B. A. Reagan, C. Baumgarten, K. Wernsing, H. Bravo, M. Woolston, A. Curtis, F. J. Furch, B. Luther, D. Patel, C. Menoni, and J. J. Rocca, "1 Joule, 100 Hz Repetition Rate, Picosecond CPA Laser for Driving High Average Power Soft X-Ray Lasers," in *CLEO: 2014*(Optical Society of America, San Jose, California, 2014), p. SM1F.4.

18. B. A. Reagan, A. H. Curtis, K. A. Wernsing, F. J. Furch, B. M. Luther, and J. J. Rocca,"Development of High Energy Diode-Pumped Thick-Disk Yb:YAG Chirped-Pulse- Amplification Lasers," IEEE Journal of Quantum Electronics **48**, 827-835 (2012).
19. B. A. Reagan, K. A. Wernsing, A. H. Curtis, F. J. Furch, B. M. Luther, D. Patel, C. S. Menoni, and J. J. Rocca, "Demonstration of a 100 Hz repetition rate gain-saturated diode-pumped table-top soft x-ray laser," Optics Letters **37**, 3624-3626 (2012).
20. F. J. Furch, B. A. Reagan, B. M. Luther, A. H. Curtis, S. P. Meehan, and J. J. Rocca, "Demonstration of an all-diode-pumped soft x-ray laser," Opt. Lett. **34**, 3352-3354 (2009).
21. A. H. Curtis, B. A. Reagan, F. J. Furch, B. M. Luther, K. A. Wernsing, S. P. Meehan, and J. J. Rocca, "Demonstration of soft X-ray laser driven by an all diode pumped CPA laser system," in *IEEE Photonics Society, 2010 23rd Annual Meeting of the* (2010), pp. 276-277.
22. J. H. Marburger, "Self-focusing: Theory," Progress in Quantum Electronics **4**, 35-110 (1975).
23. A. V. Smith, and B. T. Do, "Bulk and surface laser damage of silica by picosecond and nanosecond pulses at 1064 nm," Applied Optics **47**, 4812-4832 (2008).
24. N. Bloembergen, "Role of Cracks, Pores, and Absorbing Inclusions on Laser Induced Damage Threshold at Surfaces of Transparent Dielectrics," Applied Optics **12**, 661-664 (1973).
25. X. Fu, M. Commandré, L. Gallais, M. Mende, H. Ehlers, and D. Ristau, "Laser-induced damage in composites of scandium, hafnium, aluminum oxides with silicon oxide in the infrared," Applied Optics **53**, A392-A398 (2014).
26. X. Fu, A. Melnikaitis, L. Gallais, S. Kiá?as, R. Drazdys, V. Sirutkaitis, and M. Commandré, "Investigation of the distribution of laser damage precursors at 1064 nm, 12 ns on Niobia-Silica and Zirconia-Silica mixtures," Optics Express **20**, 26089-26098 (2012).
27. L. Gallais, J. Capoulade, J.-Y. Natoli, and M. Commandré, "Investigation of nanodefect properties in optical coatings by coupling measured and simulated laser damage statistics," Journal of Applied Physics **104**, 053120 (2008).
28. Y. Xu, L. A. Emmert, M. Alhamadani, D. Patel, C. S. Menoni, and W. Rudolph, "Comparison of defects responsible for nanosecond laser-induced damage and ablation in common high index optical coatings," Optical Engineering (**to be published).** (2016).

Introduction

Improvements in the laser damage performance of thin film materials used to engineer anti-reflective and high reflective coatings for high energy and high average power lasers operating at wavelengths ranging from visible to near infrared has been and continues to be of great importance. In particular, understanding of the damage mechanisms at sub-nanosecond pulse duration is important for increasing power extraction in near infrared terawatt and petawatt

solid state laser systems. Pulse compressor optics, space based optics, Free Electron Laser (FEL) mirrors, cryogenic active mirrors and others have all demonstrated a significant decrease in the laser induced damage threshold (LIDT) performance of metal oxide coatings when used in a vacuum environment. This decrease in the LIDT performance has been known for some time but the reasons for this decrease remain uncertain. Water impregnation in the film, carbon contamination, decreased thermal conductance and oxygen dissociation have all been proposed as possible explanations for this behavior. However, limited or inconclusive evidence has been presented to substantiate these arguments [1-10].

This paper describes results of the study of the laser damage performance of Sc_2O_3, HfO_2 and Ta_2O_5 in controlled air and UHV environments. These materials, along with SiO_2, form the backbone of optical interference film technology and are usually the most susceptible components to laser damage. Our results show a decrease in LIDT in UHV compared to in-air testing with the most significant reduction seen in Sc_2O_3. The addition of a 10 nm cap layer of a different oxide material that is optically invisible changes the laser damage behavior both in ultra-pure air and in UHV. These results highlight the importance of surface states in affecting the LIDT of the high index Sc_2O_3 and HfO_2 films. The LIDT fluence is obtained from 100-on-1 tests conducted using λ = 1030 nm pulses of 375 ps pulse duration.

Experimental details

Single, 100 nm thick layers, of amorphous Ta_2O_5, Sc_2O_3 and HfO_2 were grown by reactive ion beam sputtering onto superpolished fused silica substrates. A beam voltage of 1250 V and beam current of 600 mA were used. The oxygen flow was selected to realize the lowest absorption at λ=1030 nm [11]. A second set of identical single layer samples was capped with a 10 nm thick layer of different oxides. In this way a set of samples of Sc_2O_3 capped with HfO_2

and Ta_2O_5 and another set of HfO_2 capped with Sc_2O_3 and Ta_2O_5 were grown. SiO_2 deposited from a ceramic target was also used as capping layer in the Sc_2O_3 and HfO_2 single layers. Addition of the 10 nm thick layer does not significantly alter the optical properties of the basecoat films. The transmittance spectrum is shifted towards longer wavelengths as a result of the thickness increase. The standing wave electric field is insignificantly modified.

The absorption loss for the Sc_2O_3, HfO_2 and Ta_2O_5 single layers and of the Sc_2O_3 and HfO_2 capped samples measured using a Photothermal Common Path Interferometer [12] are summarized in table 3. In all films the absorption loss at λ=1.064 μm is at most 12 ppm. No significant changes in the absorption loss incurred with the addition of a capping layer.

Table 3: Absorption loss at 1.064 μm for the basecoats and capped samples. The absorption loss of a 100 nm thick SiO2, 1-2 ppm, is barely distinguished from that of the substrate.

Sc_2O_3 7.3± 0.6ppm	HfO_2 11.9± 0.4ppm	Ta_2O_5 5.7± 0.3ppm
Sc_2O_3/SiO_2 6.3± 0.2ppm	Sc_2O_3/HfO_2 7.0± 0.4ppm	Sc_2O_3/Ta_2O_5 9.4± 0.2ppm
HfO_2/SiO_2 11.0± 0.3ppm	HfO_2/Sc_2O_3 11.8± 0.4ppm	HfO_2/Ta_2O_5 10.6± 0.3ppm

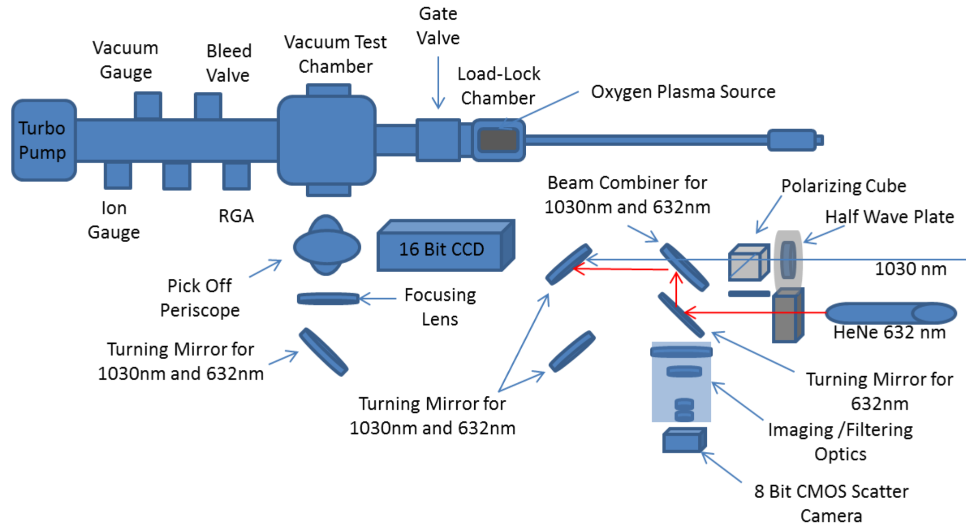

Figure 88: Diagram of UHV damage test apparatus.

LIDT testing was carried out in an ultra-high vacuum (UHV) chamber. This system, schematically shown in Fig. 88, is equipped with a load lock chamber where a clean test optic is introduced prior to placing it inside the UHV chamber. In the load lock chamber the sample is cleaned for ten minutes on each side using an oxygen plasma cleaner from XEI to remove hydrocarbon contamination. Confirmation of carbon removal is made by means of a Brooks Automation ion trap monitor recording partial pressures of elements and molecules in the main chamber with mass ranging from 0.5 to 300 amu [14]. The only carbon compound seen in the chamber prior to testing is CO_2 with a partial pressure of $\sim 7.2\times10^{-11}$ Torr. All vacuum testing was done with a base pressure of $< 5\times10^{-9}$ Torr. At this pressure, the ion trap spectrum contained small peaks at 16, 17 and 18 amu which are associated with water in the system. A peak at 28 is assigned to nitrogen and a peak at 44 is CO_2. The low partial pressure (7.2×10^{-11} Torr) of the only carbon compound, CO_2, in the vacuum chamber determined prior to damage testing, eliminates all possibilities that deposition of carbon on the surface of the optics play an appreciable role in the vacuum damage testing. It was previously shown that removal of

hydrocarbons is crucial in reliable LIDT measurements [15]. The process from sample introduction into the load lock chamber to beginning of the LIDT test, typically took eight hours. Using the same procedure, LIDT measurements were carried out in the UHV chamber at room temperature filled with ultra pure air to allow for direct comparisons between data sets taken in air and in UHV.

Single layers of Ta_2O_5, HfO_2 and Sc_2O_3, all 100 nm thick, were damage-tested in the UHV chamber filled with ultra pure air at atmospheric pressure and at UHV with a base pressure below 5×10^{-9} Torr. The LIDT zero percent probability of these films was assessed using a 100-on-1 protocol. An all-diode-pumped, chirped pulse amplified Yb:YAG system was used for this test. This system consisted of a Yb:KYW produceing ~20 nJ pulses of 300 fs duration with a repetition rate of 57 MHz. A subset of these pulses are stretched then amplified by a room temperature Yb:YAG regenerative amplifier and a cryo-cooled Yb:YAG multi-pass amplifier. The system can produce pulses of 5 ps duration and 100 mJ of energy [16-19]. For these experiments only a single one second exposure to uncompressed pulses of 375 ps was required at each test site [20, 21]. The laser was focused onto the test optics to a spot size of ~ 100 μm FWHM using a ~275 mm focal length lens with a confocal length of about 16 mm. The laser spot was moved across the sample using an external beam director controlled with mirror mounts acting in concert with a motorized two axis lens stage. The lateral position of the laser focused spot was controlled to better than one hundred microns across a half inch scan on the test optic surface with this variation being primarily due to beam jitter in other optical elements in the system. The size and shape of the focused spot was identical at all test sites. Consecutive damage sites were separated by 0.5 mm. The fluence on each spot was calculated from the measured laser pulse energy which was selected using a computer controlled rotating half wave plate

positioned just in front of a polarizer, and the beam profile taken from a representative pulse from the damaging pulse train using a cooled 16 bit Andor iKon camera. In situ damage identification was accomplished using both a front surface scatter probe imaging the damage site, illuminated with a 5mW HeNe, and also viewing the beam profile of the transmissive HeNe and one micron beam deformation after passing through the test optic. Taken together, there was perfect correlation between these two in situ damage ID methods and post damage Nomarski microscopy.

Results and discussion: Laser damage probability analyses

The zero percent probability LIDT fluence for the basecoat layers in-air and in UHV are shown in Fig. 89. In air, Sc_2O_3 has the highest LIDT followed by HfO_2 and Ta_2O_5. The UHV LIDT is reduced for all three samples, showing the smallest change in HfO_2 (-30%) and the highest (-66%) for Sc_2O_3. The uncoated fused silica substrate tested using the same cleaning methods and identical test conditions damaged at 47 ± 2 J/cm^2 in air and 52 ± 3 J/cm^2 in UHV. Here the uncertainty represents the variation in the shot to shot pulse energy, which dominates over all other errors. As it will be shown below, the insensitivity of SiO_2 to atmospheric conditions is also observed in the SiO_2 capped Sc_2O_3 and HfO_2 samples.

It should be noted that the damage threshold tests done on the bulk fused silica substrates exceeded the critical power limit, ~ 4.3 MW, for self-focusing [22]. While there is no doubt that self-focusing occurs in the bulk of fused silica, we were careful to record the fluence associated with surface damage. The other samples tested did not suffer from self focusing effects because the beam was focused onto the surface where damage was observed at nearly one third the threshold fluence of the bulk substrate material. Other work has demonstrated the need to address the influence of stimulated Brillouin scattering (SBS) in SiO_2 resulting in an enhanced

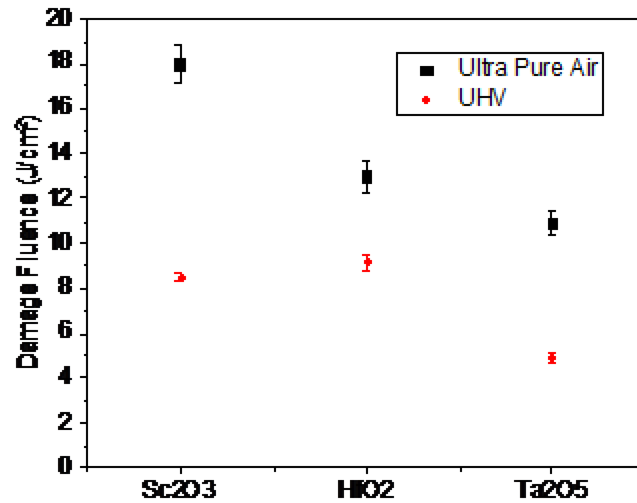

Figure 89: Zero percent probability LIDT of single layers tested in-air and at UHV. For reference the fused silica substrate damaged at (47±2) J/cm2 in-air and at 53±3 J/cm2 at UHV. The error bars are associated mainly with the uncertainty in pulse duration, ±4%.

front surface intensity and a reduced damage threshold value [23]. Given our relatively short pulse duration testing and large spot sizes, electrostriction of the sample would occur on a time scale of tens of nanoseconds. At the pulse duration of these tests, 375 ps, SBS does not significantly influence the onset values and therefore was not considered in our analysis.

Figure 90 shows the results of LIDT tests of a set of Sc_2O_3 samples grown with a 10 nm overcoat of SiO_2, HfO_2 and Ta_2O_5 tested in air and in UHV. The addition of a SiO_2 capping layer improves the LIDT in air and in UHV. Instead, in the in-air tests the LIDT reduces when adding capping layers of HfO_2 and Ta_2O_5. The decrease however, does not follow the trend shown in Fig. 89, as the LIDT of the Sc_2O_3 capped with HfO_2 is anomalously large. The UHV behavior of the LIDT of capped Sc_2O_3 also deviates from the behavior of the basecoats of Fig. 89, in that the addition of a capping layer of HfO_2 improves the LIDT of Sc_2O_3 by 2x with respect to the LIDT fluence of the uncapped basecoat. We believe the reason for the poor LIDT

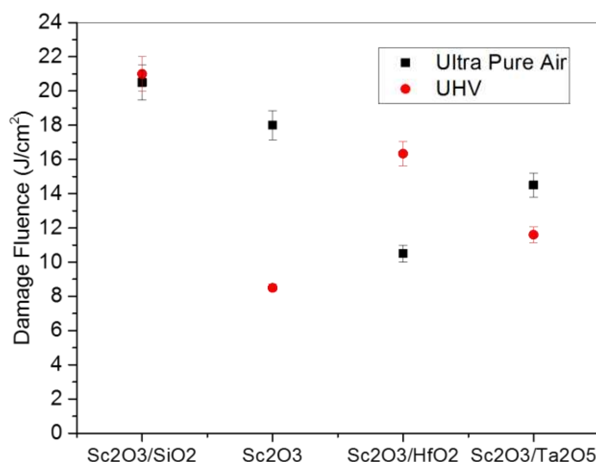

Figure 90: Zero percent probability LIDT of Sc_2O_3 capped with SiO_2, HfO_2 and Ta_2O_5 tested in-air and at UHV.

values seen in the HfO_2 capped Sc_2O_3 tested in air is due to relatively high absorbing defects within the thin HfO_2 cap. These same defects exist in the HfO_2 capped Sc_2O_3 tested in UHV but in vacuum these near surface, <10 nm from the surface, high absorbing defects are exactly the type of defect typically targeted by laser conditioning efforts. When these defects are heated in air the air acts to hold these defects and any plasma generated during their heating near the surface allowing for catastrophic damage to the surface. When these same defects are heated in vacuum there is no buffering layer to impede the rapid expulsion of these near surface defects from the surface without transferring too much energy to the thin film. This type of vacuum mediated surface conditioning has been reported by Alessi et al.[15].

The behavior of HfO_2 capped with SiO_2, Sc_2O_3 and Ta_2O_5 is shown in Figure 91. The SiO_2 capped HfO_2 film performs well in UHV with potentially no degradation in performance from the in-air LIDT value. The addition of Sc_2O_3 capping layer shows a 10% improvement in the in-air LIDT while a similar decrease is observed when adding the Ta_2O_5 capping layer.

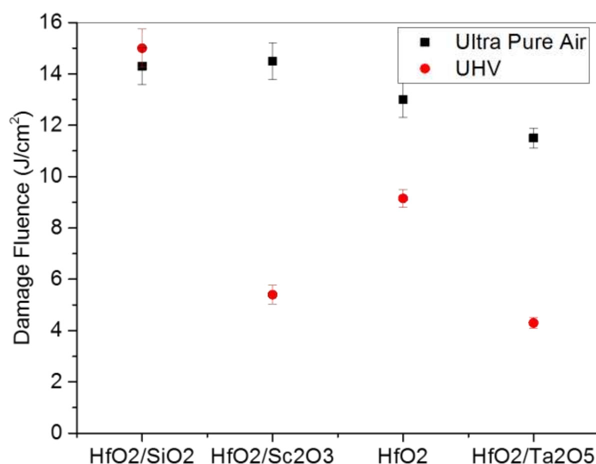

Figure 91: The 0 % probability LIDT for HfO_2 basecoat series tested in air and in UHV.

Under UHV conditions, the addition of the Sc_2O_3 cap reduces the LIDT fluence by 64%. A similar behavior is observed when adding the Ta_2O_5 cap, where the LIDT reduces to nearly the same value measured on the single Ta_2O_5 layer at UHV.

When comparing the LIDT fluence results of the Sc_2O_3 and HfO_2 capped layers of Fig. 90 and 91, the most glaring observation is the significant impact of adding only a ten nanometer cap layer to these basecoats. If the major contributor to the damage process were absorption from bulk defects in the basecoat one could expect to see a minimal modification to the single layer damage performance with the addition of a 10 nm capping layer. Instead, the variation in the damage onset thresholds for the Sc_2O_3 and HfO_2 basecoat series in air and in UHV are significant and strongly dependent on the material used as capping layer. These results suggest surface defects, whether native surface defects or laser-induced, are the dominant contributors to laser damage, in agreement with previous work [24]. The distinct behavior observed in the LIDT of the basecoat Sc_2O_3 and HfO_2 samples capped with SiO_2 which in air and in UHV shows improvements may be the result of the superior optical and mechanical qualities of SiO_2. The

IBS SiO_2 was deposited from an oxide target, which provides a better surface coverage and may more efficiently passivate surface defects. In combination, the results shown in figures 89, 90 and 91 suggest that a better choice for high index layer in interference coatings for $\lambda \sim 1\mu m$ lasers is Sc_2O_3 if the coatings are to be used at atmospheric conditions and HfO_2 if the coatings are to be used in a reducing environment.

Results and discussion: Analysis of defect densities from the laser damage probability data

The damage probability data from which the onset LIDT is obtained can be analyzed to estimate the density of defects that contribute to damage and qualitatively assess whether one or several type of defects affect damage. Fig. 92 shows the probability curves for the basecoats Sc_2O_3 and HfO_2 and capped layers of Sc_2O_3 capped with HfO_2 and HfO_2 capped with Sc_2O_3 obtained in the in-air tests.

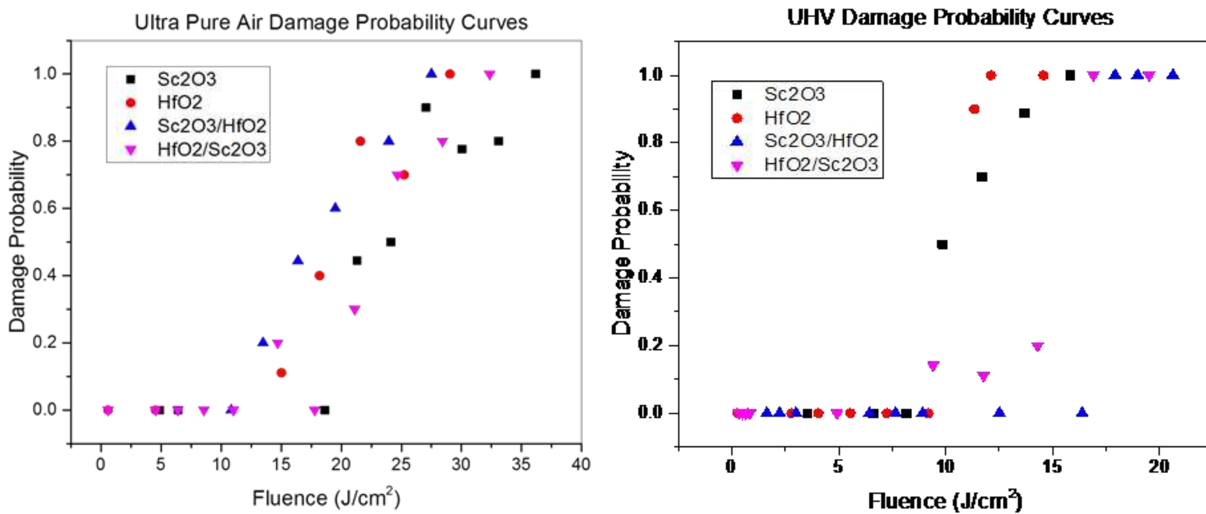

Figure 92: Damage probability versus fluence for Sc_20_3, HfO_2 and capped layers Sc_2O_3 capped with HfO_2 and HfO_2 capped with Sc_2O_3 for tests carried out in-air (left) and in UHV (right). Both of these traces show scattered data points or shoulder at low (<30%) damage probability.

In HfO_2/Sc_2O_3 the damage probability shows significantly more variance in the values up to about ~ 30% damage probability, indicating the onset of damage may be dominated by a set of

defects different than the ones controlling damage at higher probabilities. This type of behavior is evident from the analysis of the probability curves that follows.

Based on the assumption that no area defects exist below the onset threshold, the fluence dependent damage defect density, $\delta(F)$, can be described by a power law [25-27].

$$\delta(F) = \alpha(F - F_{th})^{\beta} \tag{1}$$

The damage probability curves follow a Poisson distribution as a function of both defect density $\delta(F)$ and fluence dependent area S(F), describing which part of the illuminated area is above the onset threshold.

$$P(F,S) = 1 - e^{(-\delta(F)*S(F))} \tag{2}$$

In Eq. (1), α and β are fitting coefficients extracted from the fit of the damage probability curves using a least squares regression.

We fitted the probability curves for the Sc_2O_3 and HfO_2 basecoat series obtained in the in-air and UHV tests using Eqs. (1) and (2) assuming the damage is dominated by surface states in the single layers or capping layers. At threshold the area element S(F) was chosen to be equal to the area of the nine hottest pixels in the image of the focal spot on the test optic. The average fluence value of these nine pixels at threshold is a fixed value that was used to scale the increasing area of the test site as the fluence was increased. Assuming a Gaussian spatial profile the area is scaled with the fluence which would result in a constant defect density value with increasing fluence if the defects are not fluence dependent. Any increase or decrease in the

calculated defect density with fluence is signifying an increased or decreased sensitivity to the laser field.

Figures 93 (a) and (b) show the calculated surface defect densities for the basecoat of Sc_2O_3 and HfO_2 in-air and in UHV respectively.

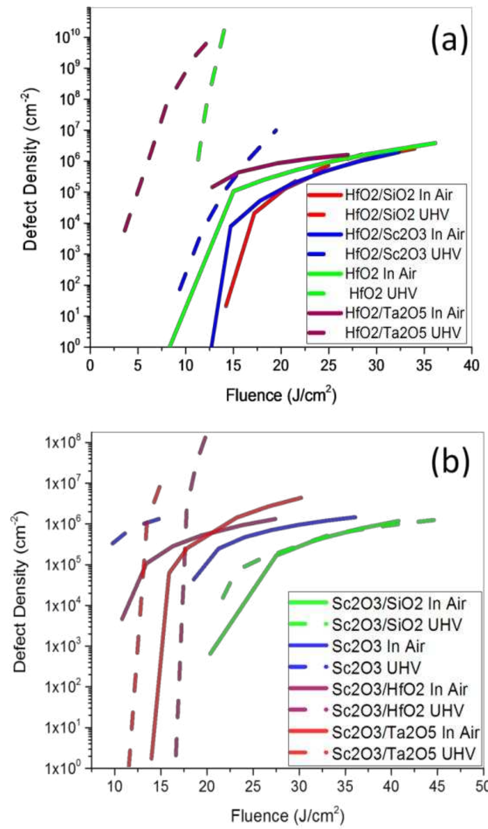

Figure 93: Figure 93 (b) Defect densities of the Sc_2O_3 basecoat series extracted from the damage probability curves in air and in UHV from the fit with Eqs. (1) and (2). (a) Defect density in the HfO_2 basecoat series.

The results of the analysis show the defect density increases with fluence, a scaling that is the contribution of the increase in the illuminated area and the fluence dependent defect density $\delta(F)$. Kinks in the traces indicate that a new type of defect with a higher laser damage threshold is turned on. The presence of defects with different turn-on thresholds in HfO_2 thin films

grown using IBS has been independently identified using a STERO-LID (Spatio-TEmporally REsolved Optical Laser Induced Damage) [28].

Analysis of the Sc_2O_3 basecoat series of Fig. 93 (b) shows that for the uncapped Sc_2O_3 sample the surface defect density increases by an order of magnitude in UHV. The similarity of the slope of the two traces suggests the same type of surface defect controls the damage behavior. A similar conclusion can be obtained from the results of the Sc_2O_3/SiO_2 samples.

The damage density behavior versus fluence of the Sc_2O_3 capped with HfO_2 is significantly different in air than in UHV. The traces show that addition of the 10 nm cap layer is effective in passivating defects that affect the UHV laser damage performance and furthermore, in eliminating a family of defects that damages at lower fluence in-air. A similar behavior is observed when adding a Ta_2O_5 cap, although in this case the set of defects contributing to damage have a lower onset, consistent with the behavior of the Ta_2O_5 basecoat. Analysis of the defect density versus fluence on the HfO_2 basecoat series shows: i) in the uncapped HfO_2 the defect density is orders of magnitude higher in UHV than at atmospheric conditions; ii) capping with SiO_2 passivates defects effectively; iii) the Sc_2O_3 cap layer effectively reduces defect density to values similar to the uncapped HfO_2 when tested in air.

Conclusions

We carried out a detailed study of the laser damage behavior of HfO_2 and Sc_2O_3 thin films with and without capping layers at ambient and UHV conditions. Detailed handling of the sample before the tests rules out hydrocarbon contamination as a possible mechanism for laser damage. The results of laser damage testing of single layers at λ=1.030 μm and ~375 ps pulse duration showed Sc_2O_3 had the highest zero % probability LIDT, 18 J/cm^2, followed by HfO_2 at 13 J/cm^2 and Ta_2O_5 with the lowest LIDT value of 10.9 J/cm^2 when tested in a controlled air

atmosphere. The LIDT of the single layers tested in UHV decreased although the relative change in LIDT did not follow the same behavior as the in-air tests. Specifically, the Sc_2O_3 sample showed a decrease in LIDT of 53%, 55% and 28% for Sc_2O_3, Ta_2O_5 and HfO_2 respectively.

When these basecoats of Sc_2O_3 and HfO_2 were capped with 10 nm thick layers composed of a different metal oxide the LIDT was significantly altered. In the case of the Sc_2O_3 basecoat series adding a 10 nm thick layer of SiO_2 improved the in-air LIDT value by ~14% while the LIDT value reduced by ~42% and ~20% when HfO_2 and Ta_2O_5 capped layers were added respectively. In the HfO_2 basecoat series tested in air the variation in the LIDT values with the addition of the 10 nm capping layers is less pronounced and the trend in LIDT follows the behavior of the single layers. Instead the addition of a 10 nm SiO_2 capping layer improved the LIDT of the Sc_2O_3 and HfO_2 basecoat samples.

The addition of a 10 nm SiO_2 capping layer to the Sc_2O_3 and HfO_2 basecoat samples improves the UHV LIDT to values similar to those measured in the in-air tests. A very thin layer of SiO_2 seems effective in passivating intrinsic defects and reducing the probability of generating laser induced vacuum-mediated defects in both basecoat materials. The UHV results also showed the susceptibility to damage of Sc2O3 in UHV, observed in the basecoat and in the reduction of the LIDT in the HfO_2 basecoat capped with Sc_2O_3. Instead, when capping Sc_2O_3 with 10 nm of HfO_2, a 53% increase in the LIDT is measured.

Analysis of the damage probability versus fluence results in-air and UHV predict different types of defects which scale with fluence at different rates. Furthermore, the analysis shows the addition of a capping layer effectively passivates a family of defects. This is more clearly evident in the comparison of the in-air and UHV tests of Sc_2O_3 capped with HfO_2 and

when the role of the capping is reversed in the HfO_2 capped with Sc_2O_3. The results of the analysis provides a clear ranking in the high index material tested depending on the environment to which interference coatings will be exposed to. When working in air, Sc_2O_3 greatly outperformed both HfO_2 and Ta_2O_5 single layers. However, at UHV the LIDT performance of Sc_2O_3 is severely compromised. Overall, the results of this study demonstrate the significant influence an extremely thin surface layer, 10 nm, has on mitigating surface states in single layers of Sc_2O_3 and HfO_2.